## NASA TECHNICAL MEMORANDUM



UB Nasa TM X-1424

A TM X-142

(NASA-TM-X-1424) FEASIBILITY STUDY OF A TUNGSTEN WATER-MODERATED NUCLEAR ROCKET.

5: ENGINE SYSTEM M.H. Krasner (NASA)

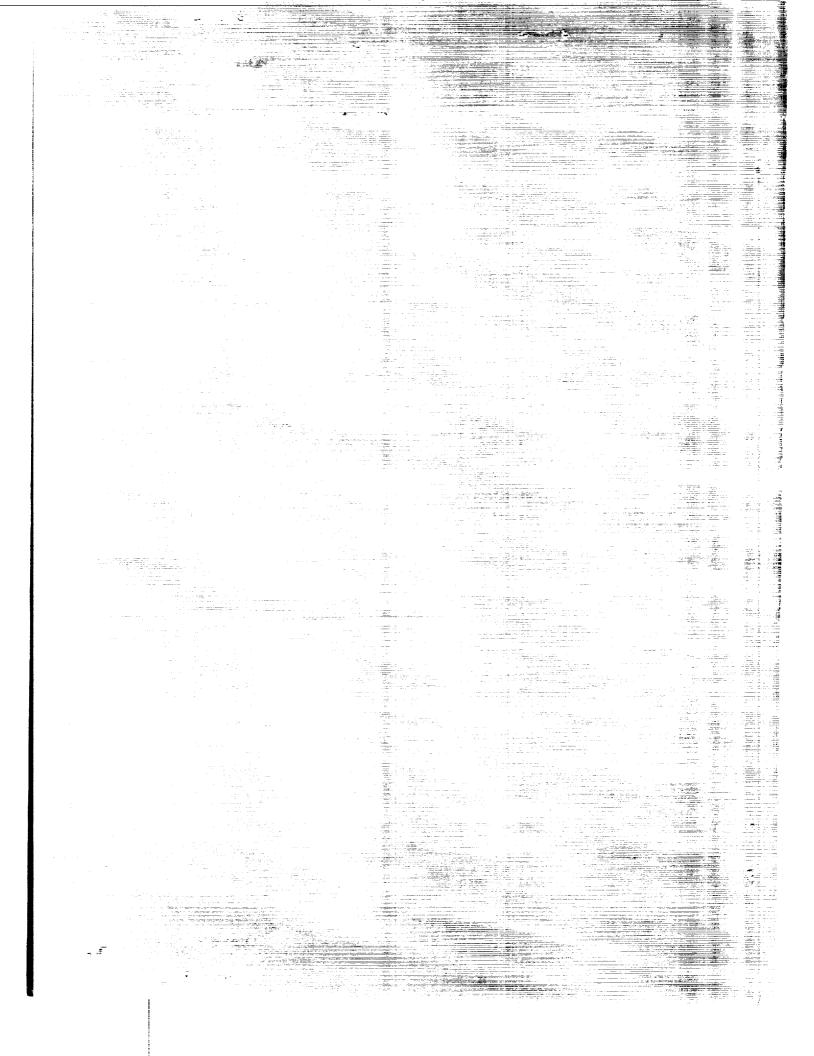
Mar. 1968 213 p

N72-74704

Unclas 00/99 40303

(ACCESSION NUMBER)
(ACCESSION NUMBER)
(PAGES)
(PAGES)
(CODE)
(CODE)
(CODE)
(CATEGORY)
(CATEGORY)
(CATEGORY)
(CATEGORY)
AVAILABLE TO U.S. GOVERNMENT AGENCIES
AND CONTRACTORS ONLY

**68** 

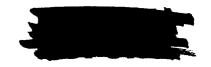


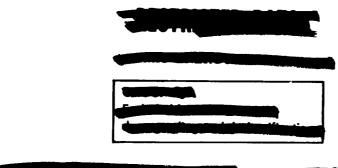
# FEASIBILITY STUDY OF A TUNGSTEN WATER-MODERATED NUCLEAR ROCKET

V. ENGINE SYSTEM

By Morton H. Krasner

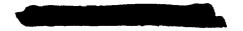
Lewis Research Center Cleveland, Ohio





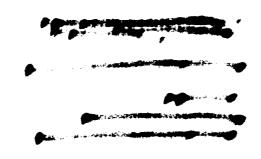


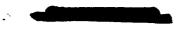
NATIONAL AERONAUTICS AND SPACE ADMINISTRATION





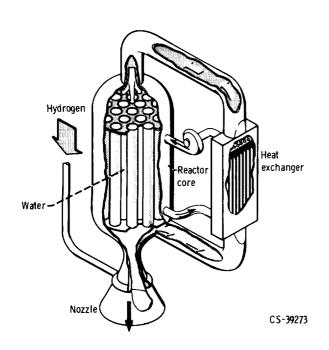






#### **PREFACE**

The concept of a nuclear rocket system based on the use of a tungsten water-moderated reactor (TWMR) was originated at the Lewis Research Center. The TWMR is a thermal reactor that uses water as the moderator, uranium dioxide as the fuel, and tungsten enriched in tungsten 184 as the



fuel element structural material. As is common to all nuclear rocket systems, hydrogen is used as the propellant to maximize specific impulse. The reactor (see illustration) consists of a tank containing a number of pressure tubes that are attached to tube sheets at the inlet and outlet ends of the reactor. The pressure tubes contain the fuel elements. The space inside the tank between the tubes is filled with water, which serves both as the neutron moderator and as a coolant for the structure. Heat is generated in the water by neutrons and gamma rays and is also transferred to the water by heat leakage from the hot fuel elements, each of which is located in a pressure tube. The removal of heat is provided by pumping the water through the core and a heat exchanger in a closed loop. The water is regeneratively cooled in the heat exchanger by the hydrogen propellant, which flows from a

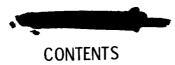
supply tank through the nozzle and heat exchanger into the core. As the hydrogen flows through the core pressure tubes and through the fuel elements, it is heated to a high temperature and is expanded out the nozzle to produce thrust.

The potential advantages of the concept lie in the following areas: The use of tungsten provides a high-temperature material with good thermal shock resistance, tensile and compressive strength, thermal conductivity, and resistance to corrosion by the hydrogen propellant. The properties of tungsten also permit the fabrication of fuel elements with very thin cross sections for good heat transfer. The use of water as the moderator provides a good coolant for the pressure vessel and structural members and reduces core size and weight over that obtained for most moderator materials. In this concept, the fuel element assemblies are structurally independent of each other and thus permit individual development of these assemblies.

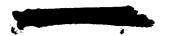
A program was undertaken at Lewis to investigate the engineering feasibility and performance of the TWMR nuclear rocket system. The results of these investigations, which are summarized in part I (NASA Technical Memorandum X-1420) of this series of reports, are presented in detail in the other six parts of the series as follows: II. Fueled Materials (NASA Technical Memorandum X-1421); III. Fuel Elements (NASA Technical Memorandum X-1422); IV. Neutronics (NASA Technical Memorandum X-1423); V. Engine System (NASA Technical Memorandum X-1424); VI. Feed System and Rotating Machinery (NASA Technical Memorandum X-1425); VII. System Dynamics (NASA Technical Memorandum X-1426).

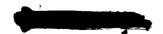






PRECEDING PAGE BLANK NOT FILMED.	Page
SUMMARY	
INTRODUCTION	. 1
I. TUNGSTEN WATER-MODERATED NUCLEAR ROCKET	. 2
CONCEPT REFERENCE DESIGN	. 2
DESCRIPTION	. 2
FUEL ASSEMBLIES	. 5
HYDROGEN FLOW SYSTEM	. 7
WATER SYSTEM	. 7
REACTOR CONTROL SYSTEM	. 9
ARRANGEMENT OF COMPONENTS	. 10
MATERIALS	. 10
ENGINE CONTROL	. 11
Startup	11
Afterheat Removal	12
ENGINE WEIGHTS	13
II. REACTOR STRUCTURE	16
PRESSURE VESSEL MATERIALS AND STRESSES	16
BERYLLIUM REFLECTOR AND SUPPORT PLATE	21
FABRICATION OF HEAT EXCHANGER	22
SYMBOLS	25
III. FUEL-ELEMENT ASSEMBLY DESIGN	26
STRUCTURAL CONSIDERATIONS	26





FUEL-ELEMENT SUPPORT TUBE VIBRATION TEST PROGRAM	28
Description of Test Specimen	29
Test Setup and Procedure	30
Test Results and Analysis	31
Spring Constants and System Damping	32
Vibration Tests of Operating Temperature Fuel-Assembly Mockup	33
INSULATION BETWEEN FUEL ASSEMBLY AND PRESSURE VESSEL	34
Heat Loss to Pressure Tube	34
Outlet Tube Sheet Insulation	36
Heat Transfer Through Lateral Support Devices	38
HEAT TRANSFER TO PROPELLANT	41
Reference Design Using Concentric Fuel Cylinders	42
Hot Channel Analysis	-
Performance of Honeycomb Fuel Assembly	44
	51
COMPATIBILITY OF TUNGSTEN AND ZIRCONIA	55
SYMBOLS	56
IV. REACTOR CONTROL	58
REFERENCE SYSTEM	58
Selection of Poison Salt Candidates	58
Selection of Materials of Construction	59
Gas Generation	59
Thermal and Radiolytic Stability of Poison Salt	62
GAS CONTROL SYSTEM - METHOD OF FABRICATING	
CONTROL ELEMENT	64
STUDIES OF OTHER CONTROL SYSTEMS	66
Thermal Analyses of Reactors with Push-Pull Control Rods	66
Thermal Analysis of Reactors with Combination Drum and Rod Control	70
V. WATER FLOW SYSTEM	71
HEAT SOURCES IN WATER SYSTEM	72
COOLING REQUIREMENTS OF CORE	73
Necessity of Flow Divider	
Trada mil mil	74 <sub>.</sub>
TI WYYNG A GYTT A CHICLE F F F F F F F F F F F F F F F F F F F	1.1



Use of Roughened Surfaces to Improve Heat Transfer	3 <b>0</b>
SIZING OF HEAT EXCHANGER	8 <b>2</b> 83
HEAT-EXCHANGER EXPERIMENTS	86 87
Transient Tests	88
Effect of Corrosion on Structural Integrity	90 90
Extent of Gas Generation	91 92
	94
VI. THRUST NOZZLE	96
HEAT TRANSFER AND PRESSURE DROP IN NOZZEE 10DES	96 99
Inlet Coolant Pressure (Case 19)	99
Power Level and Flow Rate (Cases 101 and 302)	99
Power Level (Cases 200, 201, and 202)	
Other Calculations	00
NOZZLE TUBE STRESS ANALYSIS	.00
HEAT TRANSFER AND STRESS IN FLANGE AND BACKUP SHELL	.03
SUMMARY OF NOZZLE STUDY RESULTS	.10
SYMBOLS	10
REFERENCES	113



### Printing Committee



#### FEASIBILITY STUDY OF A TUNGSTEN WATER-MODERATED NUCLEAR ROCKET

V. ENGINE SYSTEM (U) by Morton H. Krasner Lewis Research Center

#### **SUMMARY**

An overall description of the reference system used in a feasibility program is presented. Those portions of the study concerned with reactor structure and the heat transfer and structural design of fuel assemblies are discussed. Also included are results of investigations of various reactor control systems which might be used. Problems associated with the water moderator system including heat-exchanger performance, flow distribution, and water chemistry are also covered. The final section of this report deals with the heat-transfer performance and structural problems of the propulsion nozzle.

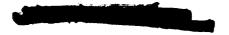
#### INTRODUCTION

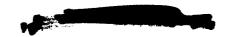
The tungsten water-moderated nuclear rocket (TWMR) engine is a system that involves several components and subsystems. The components include the reactor, turbo-pumps, heat exchangers, and nozzle. The subsystems include the water-moderator flow loop, the reactor control system, and the propellant flow system. This report deals primarily with the incorporation of these items into a complete system.

The system reference design used as a focal point in the feasibility studies of the concept is described in this report. System weight breakdowns and weight projections for other power levels are also presented.

Results of investigations on several aspects of the reactor design are presented that include selection of pressure vessel material, structural design of the fuel assemblies to withstand booster as well as nuclear stage operating loads. An analysis of heat transfer from fuel elements to the propellant is presented including a ''hot-spot' evaluation. Several techniques for reactor control are discussed with regard to their effects on system operation, size, and complexity.

Results of the water-moderator-system study include heat-exchanger design and per-





formance with emphasis on the icing problem at off-design conditions. Water flow distribution in the core region was investigated experimentally, and a summary of results is included. Results of experiments on water chemistry and their effects on system design and operation are discussed. The final section of this report deals with heat transfer, fluid flow, and structural considerations in the thrust nozzle.

Much of the work, summarized and interrelated in this volume, is reported in greater detail in referenced topical reports. The following members of the Lewis Research Center Staff contributed substantially to the material presented in this volume: Donald W. Adams, Hubert W. Allen, Harry W. Davison, Ivan B. Fiero, Colin A. Heath, John V. Miller, Walter A. Paulson, Richard L. Puthoff, and Walter F. Weiland.

# I. TUNGSTEN WATER-MODERATED NUCLEAR ROCKET CONCEPT REFERENCE DESIGN

The feasibility study of the tungsten water-moderated nuclear rocket (TWMR) concept included the evolution of a reference design. This design served as a focal point for the study and served several functions:

- (1) Pointed out problem areas that required investigation
- (2) Enabled limits to be set on the range of parameters to be explored in experimental and analytical programs
- (3) Enabled weight estimates to be made for the system
- (4) Helped clarify the interrelation of system components

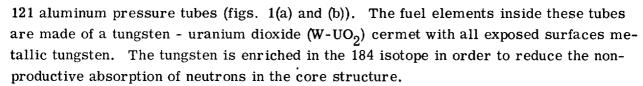
Certain features of the reference design were chosen primarily to fulfill its exploratory function, for example, the split-feed hydrogen flow system. Therefore, a final version of the concept designed to fulfill a specific mission might look quite different from this one.

#### DESCRIPTION

The reference design is composed of (1) a water-moderated, beryllium-reflected reactor, (2) a circulating water system, (3) a heat exchanger to cool the moderator regeneratively, (4) a pressure shell to house the reactor, (5) a nozzle, (6) a hydrogen feed system, and (7) a reactor control system. An assembly drawing of the reactor portion of of the powerplant is shown in figure 1. Figure 2 contains the reactor component nomenclature.

The reactor is essentially a cylindrical aluminum can 51.5 inches (131 cm) in diameter and approximately 55 inches (140 cm) long filled with water and pierced axially with





The paths of the hydrogen propellant and water moderator flow are indicated in figure 1. High-pressure hydrogen from the liquid-propellant system is supplied to the nozzle for regenerative cooling. The heated high-pressure hydrogen enters the reactor pressure vessel and passes through the tubes of a shell-and-tube heat exchanger located in an annular space outside the core and circumferentially divided into six sections. When the hydrogen leaves the heat exchanger, it is discharged into an annular manifold for collection at one circumferential location. From this point, the hydrogen is piped to a topping turbine in which approximately 70 percent of the power required in the hydrogen feed system is extracted. After a drop in pressure is experienced in the topping turbine, the propellant is readmitted to the reactor pressure shell at the center of the elliptical pressure head into the inlet plenum. Located in the plenum is a stainless-steel radiation shield and a manifold for a poison solution reactor control system. The incoming hydrogen cools these items and then enters the fuel elements. Approximately 96 percent of the gas is heated to 4460° R (2475° K) in through-flow elements and is discharged through the nozzle to produce thrust. The remainder of the gas is heated in four special reentry type fuel assemblies in the central region of the core. The temperature of this gas as it leaves these bleed fuel assemblies at the inlet end of the reactor core is  $1867^{O}$  R (1037° K). The gas is used to supply the remaining 30 percent of the hydrogen feed system power and the water moderator pump power by driving a high-temperature turbine. Figure 3 is a schematic diagram of both the hydrogen and water flow through the system. Included is a bleed-flow-driven turbine for driving the circulating pump in the chemical poison loop system and a bypass in the hydrogen feed line around the heat exchanger.

Water from the bleed-turbine-driven-moderator circulating pump enters an annular manifold in the reactor pressure vessel, as shown in figures 1(a) and (c). Six radial ducts transfer the water through the hydrogen manifold region into a plenum at the inlet end of the core. Water flows through the core region and serves both as a moderator and as a structure coolant for the aluminum pressure vessel components and the beryllium reflectors.

A second plenum at the outlet end of the core leads the water into the parallel-flow heat-exchanger sections. After giving up its heat to the hydrogen, the water passes into an approximately annular space between the core and the pressure shell flowing toward the hydrogen outlet end of the vessel before being piped back to the circulating pump. The water system is pressurized to match the reactor discharge pressure thus minimizing the loads on the outlet tube sheet.

The outlet tube sheet is cooled by water flow on one side and is insulated from the

hot exhaust gases by a series of tungsten radiation shields and stagnant hydrogen gas regions. A stagnant hydrogen gas space and radiation shield also reduces the heat flow from the hot fuel elements to the aluminum pressure tubes.

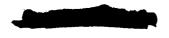
The reference reactor design includes a control system in which a poison (neutron absorbing) solution of variable concentration is continually circulated through tubes in a triangular array placed in the water moderator region. Each of these 198 tubes contains an entrance flow inner tube. Outlet flow is in the annular space between the inner and outer tubes. In addition to a circulating pump and the core tubes, the control system includes an ion exchanger used to reduce poison concentration, a supply of poison concentrate to decrease core reactivity, an accumulator-pressurizer, a solution-to-hydrogen heat exchanger, and control and isolation valving. A schematic diagram of the reference poison control loop system is shown in figure 4.

The following limitations and nominal conditions have been adopted in the reference design:

Maximum fuel plate temperature, <sup>O</sup> R; <sup>O</sup> K
Average outlet gas temperature, <sup>O</sup> R; <sup>O</sup> K
Nozzle chamber pressure, psi; N/cm <sup>2</sup>
Maximum aluminum temperature, <sup>o</sup> R; <sup>o</sup> K
Minimum wall temperature in heat exchanger, <sup>O</sup> R; <sup>O</sup> K
Poison control system pressure, psi; N/cm <sup>2</sup>
Maximum fuel loading in tungsten, vol. % UO <sub>2</sub>
Enrichment of uranium, percent U <sup>235</sup> 93
Maximum enrichment of tungsten, percent W <sup>184</sup>
Reactor power, MW
Operating life, hr

#### The following parameters characterize the reference design:

Number of fuel assemblies (including bleed)
Number of bleed assemblies
Hydrogen mass flow, lb/sec; kg/sec
Water flow rate, lb/sec; kg/sec
Specific impulse, sec
Core power density, MW/liter
Hydrogen flow in maximum power fuel element, lb/sec; kg/sec 0.957; 0.424
Core exit Mach number
Flow area in core, $\operatorname{ft}^2$ ; $\operatorname{m}^2$
Total void area in core (including aluminum), percent
Moderator area in core (including poison), percent
Tungsten plus fuel area in core, percent
Peak heat flux, Btu/(sec)(in. $^2$ ); J/(sec)(cm $^2$ )
Average dynamic head at exit of maximum power fuel assembly, psi; N/cm <sup>2</sup> 12.5; 8.62



#### FUEL ASSEMBLIES

The fuel-element configuration and support system are the heart of any reactor design. The fuel assembly must

- (1) Hold fuel in a stable configuration
- (2) Provide adequate heat-transfer surface area
- (3) Resist aerodynamic loads
- (4) Provide adequate resistance to thermal stresses
- (5) Resist loads imposed when the reactor is not in operation
- (6) Be capable of fabrication and assembly
- (7) Be amenable to inspection

A cross section through one of the propulsion fuel assemblies is shown in figure 5. The fueled tungsten is divided into axial sections or stages with a gap between them. This technique eases the fabrication problem and allows for mixing among the many parallel coolant flow passages. For the reference design, twenty-six 1.5-inch-long (3.8 cm) stages are used and a 0.125-inch (3.175 mm) gap between stages is allowed.

Alternate designs of the basic fuel-element stage are included in the reference design. They result from giving primary consideration to the ability to resist aerodynamic loads or to reduction of thermal stresses. Figure 6(a) is a view in the direction of flow of the fine geometry design resulting from the first approach. This honeycomb configuration has no large unsupported area of fueled tungsten. The great stiffness of this design affords very high power density capability resulting from high velocity flow, but this same rigidity makes it susceptible to large thermal stresses.

Figure 6(b) is a similar view of the concentric cylinder configuration designed for reduction of thermal stress. This nest of cylinders is held concentric by combs at the leading edge region. These combs also stiffen the leading edges of the larger cylinders to increase their ability to withstand aerodynamic loads. They are joined to the cylinders by brazing or are made integral with the cylinders. Since these combs are very short axially, relative expansion of the cylinders is unencumbered over most of the stage length. At the leading edge, this freedom is reduced because of the combs. If the number of combs required to prevent buckling under the aerodynamic load becomes large, this design loses its apparent advantage with regard to thermal stress.

Another version of the fine geometry design in addition to the honeycomb is shown in figure 6(c). This configuration may be worthy of consideration because it does allow for independent variation of hydraulic diameters of the flow passages and variations of the fueled material thickness with radius.

Both the honeycomb and concentric ring stages can be supported in essentially the same manner. Figures 7(a) and (b) show the details of this arrangement. The support tube is the structural element to which the stages are attached by unfueled tungsten pins





inserted from outside the support tube. These pins are prevented from falling out by a tungsten locking band. In the honeycomb design, the material which engages the pins is in six unfueled tungsten tabs produced integrally with the fuel stages. In the concentric cylinder design, the combs engage the pins to provide lateral and radial support. The pins are retained either by brazing to the support tube, as shown in figure 7(b) or by banding in a manner similar to that shown in figure 7(a).

A tungsten support tube has been successfully fabricated by vapor deposition and it may be possible to join already fabricated stages to such a support tube in the deposition process. Samples of such an assembly in which unfueled tabs on honeycomb stages received the vapor deposited support tube material to provide the joint have been produced and tested (ref. 1).

The axially continuous support tube (see fig. 5) in which the pins from each stage engage is constructed mainly of unfueled tungsten. The colder regions are made of molybdenum and stainless steel. The support tube serves both as an axial and laterial support member for the stages in each assembly and as a radiation shield to shield the aluminum pressure tube from the hot fuel stages. The support tube is held at the inlet end and supported laterally at the outlet end by the pressure tube. Several tungsten corrugated springs located in a 0.120-inch (3.05 mm) annular space between the support tube and the pressure tube provide additional lateral support. These springs are positioned at several axial locations between the midcore and the outlet end of the reactor. The annular space is filled with stagnant hydrogen to reduce the pressure stresses in the support tube. The annulus is sealed at the cold end and is open to exhaust gas pressure at the hot end. This arrangement maintains an internal pressure on the thin support tube to minimize any buckling tendency. Axial loads on the support tube are least at the hot end and increase toward the cold end.

Four of the 121 fuel assemblies are of special design. Their purpose is to provide  $2000^{\circ}$  R ( $1120^{\circ}$  K) maximum outlet gas to be used to drive high-temperature turbines in the hydrogen feed, water circulating, and poison solution circulating systems. These bleed fuel assemblies are the reentry type. The hydrogen flows from inlet end to outlet end of the core in an annular space between a normal sized pressure tube and a reduced sized support tube (fig. 8). The gas is turned to make a second pass from outlet to inlet end. In this latter pass it cools fuel stages of smaller diameter but similar in arrangement to the normal fuel assemblies. Ducts carry the hot gas through the inlet plenum and out of the pressure shell for further passage to the turbomachinery. The four bleed assemblies are located in the central region of the core. Since the maximum temperatures in these assemblies is lower than that in the others, a wider choice of materials for their construction is possible.

Both types of fuel assemblies can be inserted into the core from the outlet end. The preassembled units would comprise 26 fuel stages, support pins, cold end seal, support





tube, and reflector insert. These units are fastened into the pressure tube with spring type holding devices at the inlet end.

#### HYDROGEN FLOW SYSTEM

The hydrogen propellant is forced through the components by a feed system powered by both a topping turbine and a high-temperature bleed turbine. Schematic diagrams of the feed system are shown in figures 3 and 9. Figure 9 specifies pressures and temperatures as well as flow paths. By extracting as much of the required pumping power as possible in the topping turbine, a minimum specific impulse penalty is suffered. The first-stage hydrogen pump is driven by a bleed turbine that uses high-temperature gas from the previously described bleed fuel assemblies. A schematic diagram of the bleed flow with pressures and temperatures is shown in figure 10. In addition to driving the first-stage hydrogen pump, the bleed flow also drives the poison-control-solution pump and the water-moderator pump.

Such a split-feed system has more components than either an all-topping or all-bleed arrangement. However, it does avoid operational limits imposed by power available in the topping turbine and has a higher specific impulse than an all-bleed system.

The final selection of a feed system and/or the division of bleed and topping turbine power in a split system depends to some extent on chamber pressure in the nozzle. Only a mission analysis based on adequate performance and weight data for engine components can optimize this selection. The reference system has a nozzle chamber pressure of  $600 \text{ psi} (414 \text{ N/cm}^2)$ . Although an all-topping system can provide all the required pumping power for this chamber pressure, it is in keeping with the purpose of the reference design that the split-feed system be incorporated. By taking account of the problems involved in such a system, for example, regions of high pressure in the reactor container and specialized fuel assemblies in the core, an increased degree of applicability can be achieved.

#### WATER SYSTEM

The circulating water-moderator system is unique to this type of reactor. There are several areas of concern in the water system. The first of these areas is the water to low temperature hydrogen heat exchanger and the problem of icing. Calculations have indicated that ice-free operation is not difficult to achieve at design flow conditions. The results of these calculations were verified experimentally (see the section on HEAT-EXCHANGER EXPERIMENTS, p. 86). In the same experiments, transient operation in





a mockup heat exchanger has been explored, and the results indicate that a series of steady-state calculations can adequately predict transient behavior with regard to icing. Provision has been made for the controlled bypassing of hydrogen around the heat exchanger should that become necessary during off-design operation.

The flowing-water moderator is used to remove heat from reactor structural components. In normal operation, the water temperature in the loop varies over a narrow range of temperature (650° to 700° R (361° to 389° K)). This relatively constant temperature heat sink should minimize thermal stresses in the reactor pressure vessel and core structural components and make possible the use of low-temperature materials.

There are two critical areas of heat removal by the water from pressure vessel components. In these areas, both heat induced by nuclear radiation and heat transferred from high-temperature regions of the core are involved. Since heat is transferred to the aluminum pressure tubes through the stagnant hydrogen space from the high-temperature fuel assemblies, a high water velocity is required on the lower two-thirds of the pressure tubes to maintain a 760° R (422° K) aluminum wall temperature. To reduce the total water flow required as a result of the high velocities, for divider tubes were installed around the pressure tube, as shown in figure 5. These baffles form two general areas of parallel flow in the core; a high-velocity region between the flow divider and pressure tubes, and a low-velocity region outside the flow dividers. This arrangement requires suitable baffle plates and flow distribution orifices.

The other area of critical heat transfer to the water is the outlet tube sheet. In the reference design, buffer zones of stagnant hydrogen and radiation shields were provided to reduce heat transferred from the hot gas to the tube sheet by flaring the support tube out over the tube sheet, as shown in figure 5. Heat transferred to this flared region from the gas is radiated to the cooler nozzle surface which thereby becomes the sink for the bulk of the heat transferred from the gas and allows a relatively low temperature to exist in the flared region. Heat transfer from the flared tube region to the tube sheet is reduced by a second radiation shield and two stagnant hydrogen insulating spaces. Even with such a configuration, a fairly high water velocity is required over the tube sheet to maintain allowable operating temperatures. Preliminary investigations of the water flow distribution in the plenum at the outlet end of the core indicate a fairly complex flow pattern (ref. 2). It would probably be necessary to explore this situation further to ensure that adequate heat-transfer coefficients exist everywhere across the tube sheet to cool it adequately.

Hydrogen generation in the moderator system due to corrosion and radiolytic decomposition have been investigated, as discussed in the section WATER MODERATOR SYSTEM CHEMISTRY (p. 90). The severity of this problem is dependent on the mode of operation of the system. The operational requirements of a specific mission or ground





test program coupled with the experimental data for such hydrogen generation would indicate whether methods for coping with this problem would be necessary.

#### REACTOR CONTROL SYSTEM

The control system incorporated in the reference design is aimed at achieving the following special results in addition to normal control system requirements:

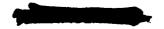
- (1) Constant power distribution pattern in the core for all operating conditions
- (2) Minimum peak to average power generation in the gross radial sense
- (3) Minimum variation in circumferential power distribution in any given fuel assembly

A poison (neutron absorbing) solution, cadmium sulfate in water, is circulated through the core region in two-pass control tubes (see figs. 1(a) and (c)). These tubes surround each pressure tube in a pattern which eliminates the regions of increased moderator thickness which would otherwise exist with a triangular array of round tubes. This arrangement reduces circumferential power scalloping in the fuel assembly. The large number of tubes keeps the distribution of poison fairly even across the core and minimizes gross power distortions due to control devices. Since the poison solution is always located in the same areas of the core with only the concentration changing to vary reactivity, the power distribution should remain uniform over core operating life.

The constantly circulating poison solution is pressurized to match moderator pressure and thus reduce system structure. The circulating pump, ion exchanger, poison supply, and other system components are located outside the core. The system will contain approximately 22.5 gallons  $(8.52\times10^{-2} \text{ m}^3)$  of solution. Cycle time is approximately 2 seconds with flow velocities limited to 40 feet per second (12.2 m/sec).

Figure 4 shows a schematic diagram in which the flow path for the circulating poison has a variable bypass through the ion exchanger for decrease of poison concentration. Increase of poison concentration is accomplished by forcing poison into the system from a pressurized concentrate reservoir through a high or low rate line. The feasibility of a practical system of this type in such an application is closely tied to the inherent negative temperature coefficient of the core at operating temperature. Such a characteristic makes the use of a relatively slow acting control system reasonable.

In addition to this sort of control system, it will be necessary to provide another system for rapid shutdown of the reactor in case of an emergency. It would probably not be necessary to make provision for rapid recovery from such a fast scram. The injection of a poison solution from a pressurized container directly into the moderator system just upstream of the core appears to be one reasonable approach to this requirement.



#### ARRANGEMENT OF COMPONENTS

The components of the engine system including the paths for fluid flow were arranged with two primary considerations in mind: (1) compactness and (2) minimum stresses.

The heat exchanger located in the annular space surrounding the core means that the hydrogen leaving the nozzle can flow directly into the tubes of the heat exchanger without extensive manifolding and piping. The high-pressure gas occupies the tube space in the exchanger rather than the shell space because the tubes are better able to stand the pressure.

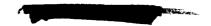
Another component arrangement in the reactor core to be noted is in the region of the inlet end reflector. This beryllium disk serves not only to produce a desirable axial power distribution, but it is also the main support structure for the fuel elements. The loads produced on the fuel stages can be traced through the support pins to the support tube where they are eventually transferred to the pressure tubes. Collars on the aluminum pressure tubes shown in figure 5 bear on the top surface of the inlet reflector to transmit the loads into it. The reflector is a 3-inch-thick (7.62 cm) plate of forged beryllium and is much stiffer than the thin aluminum inlet header, which becomes a redundant structure for this load. The reflector is well cooled so that thermal stresses are small.

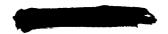
Manifolds for the poison control solution are located in the pressure vessel head so that emergency shutoff of the external control loop can be achieved with only two valves. This can also reduce the weight of the manifolds because the pressure difference between the poison system and the hydrogen is not great. Pressure balancing between the water moderator system and the hydrogen discharge pressure will reduce stresses in the pressure vessel, particularly in the outlet header.

#### **MATERIALS**

The key material in the concept reference design is, of course, tungsten enriched to 87 percent W<sup>184</sup>. The possibility for producing this material by gaseous diffusion in an existing facility has been investigated and appears economically feasible (ref. 3). An extensive metallurgical program has been conducted to determine those properties of fueled natural tungsten important to the nonnuclear aspects of the reactor design.

The use of the forged beryllium inlet reflector as a structural member is considered to be feasible because of the demonstrated ability of beryllium producers and fabricators to forge pieces of this size. Heat shields for the Mercury Project capsules were even larger in diameter. Forged beryllium exhibits reasonable ductility with greater than 10 percent elongation at fracture in tensile tests. This member is subject primarily to





a bending load in which maximum stresses occur at the outer fibers where maximum forging action would occur. Calculated stresses in the perforated reflector are half the values of ultimate strength exhibited by forged beryllium.

The reactor pressure vessel is designed for 6061-T6 aluminum. A 760° R (422° K) temperature limitation was adopted in vessel components. If this temperature limitation should become untenable in areas like the outlet tube sheet, one possible remedy may be to substitute a zirconium alloy and suffer some penalty in weight. It is also possible to use stainless steel and suffer some reactivity penalty.

#### **ENGINE CONTROL**

During full-power operation, the control system will be required to maintain the proper thrust by keeping propellant flow and reactor power at the proper levels. The negative temperature coefficient of the reactor should make the reactor power requirement fairly easy to achieve. Propellant flow must be regulated by controlling the feed-system turbopumps. In addition, the water temperature must be regulated to avoid overheating the fuel-assembly pressure tube or freezing in the heat exchanger. Manipulation of the bypass hydrogen around the heat exchanger can be used for this purpose.

The most severe requirements for the engine control system will occur during system startup and shutdown. Certain features of the TWMR concept tend to alleviate problems which might be encountered in these operations.

#### Startup

The possibility exists for circulating the water moderator and poison control solution at low flow rates by using auxiliary pumps. It will, therefore, be possible to operate the reactor at low power with no hydrogen flow and to warm the circulating water moderator by transferring heat from the hot fuel elements across the insulation gap between the support tube and the pressure tube. During startup, then, a heat source other than sensible heat of the components is readily available to the incoming hydrogen and the bootstrapping operation should become easier.

A likely general sequence for startup is as follows:

- (1) Start circulation of poison control solution and moderator using auxiliary pumps.
- (2) Bring the reactor critical and to some low power by removing poison from control solution.
- (3) Allow the water moderator and fuel to heat. The accompanying reactivity loss is overcome by reducing poison concentration to maintain power at the low level.





- (4) Chill pumps with liquid hydrogen and set turbopump and heat exchanger bypass valve positions for bootstrapping procedure.
- (5) Start hydrogen flow through the system under tank pressure and commence bootstrapping as decreasing fuel element and water temperatures increase reactivity. During this bootstrapping operation, no attempt to regulate hydrogen flow would be made and only reactor power would be ramped at a certain rate by using the poison control system.
- (6) After a significant power level has been reached, activate the complete control system to control hydrogen flow and reactor power to achieve a high specific impulse during the power ramp. This part of the startup sequence is expected to take less than 1 minute, and both the heat-exchanger bypass valve and the poison control system would be used to control reactivity.
- (7) After full power and outlet gas temperature are reached, maintain operating conditions by controlling propellant flow rate and water-moderator temperature.

The feasibility of this type of startup sequence has been studied as discussed in reference 4.

#### Afterheat Removal

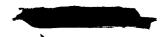
The reduction of power during system shutdown would be controlled by use of the poison system and the heat-exchanger bypass valve. Reference 4 also describes shutdown performance of the system.

The method of removing post-shutdown heat generated by nuclear radiation from decaying fission products is an important consideration in the design of a restartable nuclear rocket engine system. After the reactor has been shut down for a short period of time, the principal source of heat is the beta and gamma radiation from the decaying fission products. These fission products persist for a long period of time, and the heat generated by them must be removed to prevent overheating of core components. Most of the beta particles are absorbed in the fuel elements, whereas the gamma particles are absorbed throughout the core.

Figure 11 shows the calculated total beta and gamma power generated from 1 hour to 1 year after shutdown for several reactor operating times. At some time after shutdown, all the heat generated can be radiated to space with no hydrogen flow required.

The heat loss by radiation to space from the pressure vessel was calculated as a function of source temperature, sink temperature, and emissivity of the radiating surface. The results are shown in figure 12. The source temperature is that of the external aluminum pressure vessel and must be kept at a reasonable level. If a source temperature of 660° R (367° K) is assumed and an emissivity of 0.9, achievable with a suit-





able coating, is used,  $3\times10^{-4}$  percent of full power can be radiated to space. This power level is reached 14 days after shutdown from a 1-hour operation, as indicated in figure 11.

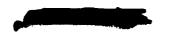
It would, therefore, be necessary to supply some cooling to the reactor for these 14 days. It is also necessary to minimize the amount of cooling required for this task. With the assumption that hydrogen at a core inlet temperature of 322° R (179° K) would be used for cooling the core, calculations of steady-state heat-transfer and pressuredrop performance were made at various power levels and flow rates. The digital computer Multiple Channel Analysis Program (MCAP, ref. 5) was used in these calculations, and the results are shown in figure 13. In the regions of negative slope  $\,d\,\Delta\,P/dW$ , laminar flow cannot be maintained because of instability. To avoid these regions, coolant flows at reduced power will have to be maintained at flows higher than the flows corresponding to these powers. At 1-percent power, for example, more than 4 percent of the full flow is required, which will mean overcooling the core at these low power levels (less than 10 percent of full power). Pulse cooling may be used to avoid the resulting waste of coolant. With this technique, core component temperatures are dropped to well below the normal operating temperatures during cooling pulses. Between pulses, the heat generated in the core raises the component temperatures again until the next pulse is started. Prior to the time pulse cooling is started, coolant flow can be continuously decreased to remove the heat generated as power is reduced.

The use of these three modes, steady hydrogen flow, pulsed coolant flow, and radiation to space, should result in near optimum expenditure of propellant for a mission in which restart is required. The amount of hydrogen required for afterheat removal has been estimated to be of the order of 4 percent of that used in a 30-minute run at full power.

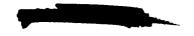
#### **ENGINE WEIGHTS**

Calculations of engine weights resulted in the following breakdown of the overall system:





Reactor assembly		Veight
	lb	kg
Reactor pressure vessel (aluminum)	1325	601
Reactor pressure vessel head (aluminum)	175	79.5
Inlet-end reflector (beryllium)	130	59
Side reflector (beryllium)	1060	481
Heat exchanger tubes, 720 aluminum tubes 3/8-inch (0.952 cm) outside diameter by 0.035-inch (0.089 cm) wall	111	50. 4
Inlet reflector inserts, 117 assemblies:		
Stainless-steel jackets and mountings	213	97
Beryllium inserts	145	66
Total	358	163
Fuel assembly, 117 assemblies:		
Stage support members and stiffeners	416	189
Support tubes	404	183
Tungsten cladding	412	187
Tungsten in fueled material	1710	776
UO <sub>2</sub> fuel	199	90
Stainless-steel mountings	26	12
Total	3167	1437
Heated bleed fuel assembly, 4 assemblies:		
Total tungsten	51	23. 1
UO <sub>2</sub> fuel	3	1. 36
Stainless-steel mountings	7	3. 18
Inconel support tube	18	_8. 17
Total	79	35.81
Poison control components (dry)	208	94.5
Poison control solution	121	54.9
Flow divider tubes (aluminum)	128	58.1
Pressure tubes (aluminum)	310	141
Water inside pressure vessel	1837	834
Total weight of reactor assembly	9009	4088



	<b>.</b>

Nuclear rocket engine system	Weight	
	lb	kg
Reactor assembly	9 009	4088
Nozzle and chamber	1 281	581
Liquid-hydrogen turbopumps:		
First-stage pump and turbine	349	158
Second-stage pump and turbine	349	158
Total	698	316
Water turbopump	201	91
External poison system components	507	230
External moderator piping	747	339
External moderator (water)	924	419
Liquid-hydrogen system piping and fluid	372	169
Total system weight	13 739	6222

The densities used in the calculations are given in the following table:

Material	Density		
	lb/in. 3	g/cm <sup>3</sup>	
Aluminum	0. 098	2.72	
Beryllium	. 067	1.85	
Stainless steel	. 290	8.04	
Tungsten	. 697	19.3	
Uranium dioxide	. 387	10.7	
Inconel	. 307	8, 50	
Liquid hydrogen	. 0026	. 072	
Water	. 036	. 997	

It should be noted that no shield weights are included in the preceding tabulation.

The 830-second specific impulse for the system is based on the performance of nozzle with an area ratio of 40 and an efficiency of 98 percent. The thrust resulting from this specific impulse is 77 000 pounds (3.42×10 $^5$  N) and the thrust to weight ratio of the unshielded nuclear rocket engine is 5.6 pounds thrust per pound weight (54.8 N/kg). Estimates were made for larger reactors of this type and for smaller ones down to the reactivity limits using both uranium 235 and 233. Thrust to weight ratios were calculated and are reported in reference 6. Figure 14 shows the principal results of these performance projections. The dynamic head performance line of 12.5 psi (8.62 N/cm $^2$ ) is based on the use of concentric-ring fuel stages, and the core pressure drop line of 250 psi (172 N/cm $^2$ ) is based on the use of a fine geometry fuel stage with no dynamic head limit.





### II. REACTOR STRUCTURE

#### PRESSURE VESSEL MATERIALS AND STRESSES

The primary structural member of the TWMR is the pressure vessel which serves the multiple functions of

- (1) Containing the reactor core structure and loads
- (2) Containing the heat-exchanger structure and loads
- (3) Providing passages and plenums for both the moderator water and hydrogen propellant
- (4) Transferring thrust produced by the nozzle to the engine structure The vessel is exposed simultaneously to pressurized hot water, cryogenic flowing hydrogen, and stagnant hydrogen at moderately high temperatures. The water pressure level is matched to the 600-psi (414  $\rm N/cm^2$ ) nozzle chamber pressure. The water temperature must be maintained below the saturation temperatures (930° to 945° R (516° to 525° K)) at the various pressures in the circulating systems. The more important criteria for vessel material selection are
  - (1) Compatibility with the total environment
  - (2) Neutronic efficiency of the reactor
  - (3) Weight for a flight engine
  - (4) Fabricability

The materials considered were aluminum alloys, 6061-T6 and 6071-T6; Inconel X-750; titanium alloy Ti-6Al-4V; Zircaloy-2; and 304 stainless steel. They are discussed in the order of the preceding criteria.

The aluminum alloys require a limitation on maximum water temperature which restricts the operational flexibility of the system. If the water purity is maintained, no serious structural corrosion problems will be encountered with aluminum. Preoxidation of the surfaces will minimize corrosion-generated hydrogen, but the resulting hydrogen may require special consideration, as discussed in the section WATER MODERATOR SYSTEM CHEMISTRY (p. 90).

The Zircaloy-2 material does not impose the water temperature limitation associated with aluminum, and water purity is less of a problem. Zirconium is, however, subject to hydriding, and many surfaces of the vessel are exposed to hydrogen. Specially critical are the pressure tubes and the outer tube sheet both of which are exposed to hydrogen at moderately high temperatures and high pressure. Since hydriding results in embrittlement and loss of toughness, protective coatings would have to be applied at least to these components of the vessel.

Inconel, titanium, and stainless steel present no problems as far as the nonnuclear





environment is concerned. They all are compatible with water and hydrogen at the operating conditions encountered.

Three primary criteria were considered in the investigation of nuclear properties of pressure vessel materials: (1) thermal neutron absorption cross section, (2) gamma heat generation, and (3) radiation damage. Absorption cross section should be minimized for neutron economy in the reactor core. The pressure tubes are the primary concern in this respect. Gamma heat generated in the structure must be dissipated to prevent exceeding the temperature capabilities of the materials involved. Radiation damage could lead to degradation of physical and mechanical properties to the point where the useful life of the structure is shortened.

Table 1 lists the macroscopic absorption cross sections  $\Sigma_a$  (cm<sup>-1</sup>) for the materials investigated. Zircaloy-2 and the aluminum alloys have the lowest and best in this respect. Cross sections of the remaining alloys are of a higher magnitude and must be considered as less desirable from a neutron economy basis.

The gamma heat generated in the pressure vessel material presents two problems: (1) maintaining adequate coolant flow on the surfaces to remove the heat and give safe working temperatures for the material, and (2) maintaining temperature gradients and thermal stresses at reasonable levels. No single property of a pressure vessel material can be used as an index of desirability in the presence of gamma heating. Low density will result in a small amount of heat generated per unit volume. High strength will reduce the amount of material required. Low expansivity and modulus, and high conductivity will reduce thermal stresses. High ductility, desirable in any complicated structure to accommodate local stress concentrations, assumes additional importance in the presence of gamma heating. None of the materials considered should suffer any radiation damage for the exposures expected in this application.

The sink for the heat generated in the pressure vessel is either the water moderator or the propellant. The water temperature range  $(650^{\circ}\ \text{to}\ 700^{\circ}\ \text{R}\ (361^{\circ}\ \text{to}\ 389^{\circ}\ \text{K}))$  is for the reference system with an aluminum pressure vessel. This temperature was maintained in order to keep the aluminum below  $760^{\circ}\ \text{R}\ (422^{\circ}\ \text{K})$ . If a material with a higher permissible operating temperature were used, a higher water temperature could be tolerated. This would provide an advantage in heat exchanger size and/or operation flexibility with regard to icing.

Data were compiled for mechanical properties of each of the materials considered for use in the pressure vessel. Representative values of manufacturer's data are presented in figure 15. They were used in calculations presented in this section for determining the suitability of the materials.

Hoop stresses due to both pressure loads and temperature gradients were calculated in the outer cylindrical shell portion of the pressure vessel for three of the materials under consideration, 6061-T6, Zircaloy-2, and Inconel X-750. Operating conditions for





the reference design were used in the aluminum calculations. For the Inconel X-750 and Zr-2 cases, higher water temperatures and a counterflow heat exchanger were assumed. For these two materials, it was also assumed that a higher heat-transfer coefficient could be maintained in the water flow passages. These variations are reflected in the temperatures, pressures, and heat-transfer coefficients used in calculations for each of the three materials. A summary of values used in each case is given in the following table:

Material	Water pressure		Water temperature		Heat-transfer coefficient		Heat- generation rate,	
	psia	N/cm <sup>2</sup> abs	<sup>o</sup> R	°к	$\frac{\text{Btu}}{(\text{hr})(\text{ft}^2)(^{0}\text{R})} \frac{\text{J}}{(\text{hr})(\text{m}^2)(^{0}\text{K})}$		<b>W</b> /g	
Aluminum 6061-T1	a <sub>505</sub>	348	644	358	1845	3.78×10 <sup>7</sup>	2.65 4.00	
Zircaloy-2 Inconel X-750	700 700	483 483	740 740	411 411	2680 2680	5. 48×10 <sup>7</sup> 5. 48×10 <sup>7</sup>	2.65 2.65	

<sup>&</sup>lt;sup>a</sup>Latest reference-design value is 534 psia (368 N/cm<sup>2</sup> abs).

In all cases, it was assumed that all heat generated in the vessel wall flowed inward to the water coolant. Maximum stresses occur at the inner surface of the vessel where both thermal and pressure hoop stresses are tensile. No axial temperature gradients were considered. Modulus, expansivity, and conductivity values were determined at average wall temperatures. In calculating thermal stresses, the curvature of the shell was ignored, and a flat plate was assumed. Since wall thicknesses are small, heat-generation rates were assumed constant through the material.

Temperature levels and gradients in walls of various thicknesses were determined by using the assumed values of water temperature, heat-transfer coefficient, and heat-generation rate as given in the preceding table. The results are shown in figure 16 and indicate the great importance of low density and high thermal conductivity. Aluminum shows little temperature gradient; Zr-2, with the worst combination of density and conductivity, requires the largest gradient among the materials considered to transfer the generated heat.

The maximum thermal stresses resulting from these gradients were calculated for various thicknesses by using the approximate relation

$$\sigma_{\text{max}} = \frac{\mathbf{E}\alpha}{1 - \nu} \frac{2}{3} \Delta \mathbf{T}$$

which results from a combination of (ref. 7)



$$\sigma_{\text{max}} = \frac{E\alpha}{2(1 - \nu)} \left( \frac{\text{qt}^2}{6k} + \Delta T \right)$$

and

$$\Delta T = \frac{qt^2}{2k}$$

for uniform heat generation.

Pressure stresses were also calculated and added to the thermal stresses to give a total tensile stress at the inner surface of the vessel wall. The results of these calculations for each of the three materials are shown in figure 17. Also plotted are the yield strength and 0.8 yield strength values for the material at the average wall temperature for each thickness of material.

Two preliminary criteria were adopted for determining an adequate design:

- (1) The pressure stress must be no higher than the 0.8 yield point value.
- (2) The combined pressure and thermal stress must be no higher than the yield point value.

Application of these criteria indicate that the hot-rolled Zr-2 would not provide a satisfactory design and that cold-worked material would have to be used. The minimum required wall thicknesses for three materials are listed in the following table along with pressure vessel weights relative to aluminum.

Material	İ	ım wall	Weight ratios	
	in.	cm	aluminum	
Aluminum 6061-T6	0.42	1.07	1	
Inconel X-750	. 18	. 46	1.31	
Zircaloy-2 (10 percent cold worked)	. 38	. 96	1. 97	

The thickness estimates were made on the basis of parent material strength for all the materials. Postwelding heat treatment of welds in 6061-T6 does restore parent material properties and will be utilized in longitudinal and other joints wherever possible in the structure. It may well be necessary, however, to employ an as-welded longitudinal joint because of the complicated configuration. Under those circumstances, the common technique of increasing the thickness in the immediate area of the weld must be utilized. Included in figure 17(a) is a plot of as-welded 6061-T6 minimum yield strength. It indicates that the local combined thermal and pressure stresses will exceed the yield stress





in the region of the weld. Such a situation is not considered prohibitive because of the conduction of heat from the local area and because of the ability of small strains to alleviate local thermal stresses. Figure 17(a) also shows thermal stress in aluminum with two different heat-generation rates. As can be seen, errors in estimates of heating rate will have negligible effects on total stress.

An examination of the physical and mechanical properties of 6071-T6, 6Al-4V titanium and 304L stainless steel would indicate that

- (1) 6071-T6 would result in 25 percent lower weight than the 6061-T6.
- (2) 304 Stainless steel does not possess enough strength in the annealed condition to handle the combined pressure and thermal stresses.
- (3) The 6Al-4V titanium alloy in the annealed condition appears to be an adequate material for the stresses occurring in the pressure vessel. Such a vessel would probably weigh less than the 6061-T6 version.

The best pressure vessel material of those structurally suitable for use in a nuclear rocket will depend on the permissible neutron cross section. As reactor power and core size increase, the tolerable cross section becomes greater. The principal gains to be realized from the use of the higher neutron cross section, higher temperature material are higher moderator temperature and greater flexibility of powerplant operation. Until the nuclear requirements allow use of a high-cross-section alloy, such gains cannot be realized. Because fabrication problems that occur from using the cold worked Zr-2 alloy in a complex structure may be quite severe, the only remaining low-cross-section material of those considered is an aluminum alloy. Existing fabrication knowledge would make the 6061-T6 alloy the safer aluminum choice.

The previous discussion assumed that the entire pressure vessel would be made of the same material. A composite vessel in which the outer, more highly stressed members were made of high-cross-section material, and the internal thinner members, such as pressure tubes, were made of low-cross-section material might afford some advantage. One potential advantage is that the reduced surface area of aluminum in the water system will result in less corrosion-produced hydrogen in the moderator. If Zr-2 internal parts were combined with Inconel external pressure vessel components, this advantage plus the higher moderator temperature advantages could be realized. Use of Zr-2 pressure tubes depends on the seriousness of the hydriding problem on the inner surface of the tube and the possibilities of preventing deterioration. Stainless steel can be joined to either zirconium or aluminum in simple tube configurations by using present technology. The use of this type of joint configuration only would make possible a composite vessel design in which internal members could be of low cross section.

Although the possibilities indicated previously do exist, the reference design still utilizes an all-aluminum 6061-T6 pressure vessel. Its advantages are





- (1) Low thermal stresses
- (2) Low weight
- (3) Well-established commercial fabrication techniques

#### BERYLLIUM REFLECTOR AND SUPPORT PLATE

The beryllium reflector at the inlet end of the core is desirable to improve the axial power distribution in the core. The use of this thick member to carry the fuel-element drag and pressure loads across the inlet tube sheet is very desirable but such use depends on the suitability of beryllium as a structural member. The reflector contains holes for both the pressure tubes and the poison control tubes and is loaded primarily normal to its diameter. The maximum stresses in this bending situation occur at the flat surfaces in the ligaments between the holes. Stress concentrations are also present and this situation requires a material with reasonable ductility. As previously pointed out in the section MATERIALS (p. 10), forged beryllium seems to be a satisfactory material. Therefore, the beryllium reflector was used as a structural member in the reference design.

The reflector is approximately 40 inches (1.016 m) in diameter and is bolted to the aluminum pressure vessel. The holes for the pressure tubes are 2.56 inches (6.5 cm) in diameter and are spaced 3.16 inches (8.02 cm) between centers in a triangular array. Six poison tube holes, 0.56 inch (1.42 cm) in diameter, symmetrically surround each pressure tube. A plan view of a portion of the reflector showing the hole arrangement is shown in figure 18.

Calculations of drag, pressure drop, and axial acceleration loads on the maximum performance fuel assembly yielded a value of approximately 330 pounds (1470 N). The pressure of the hydrogen above the inlet tube sheet is approximately 710 psi (490  $\text{N/cm}^2$ ), and the pressure in the water below the reflector plate is about 610 psi (421  $\text{N/cm}^2$ ). In considering the pressure loads, the thin aluminum inlet tube sheet was assumed to transmit its portion of the loads through the pressure tube collars to the reflector. Stresses were calculated in a 3-inch-thick (7.62 cm) inlet end beryllium reflector plate, since this is a reasonable thickness from the standpoint of core neutronics.

These stress calculations were made considering the 100-psi (69.0 N/cm $^2$ )  $\Delta p$  load acting on the solid areas of the plate and a 330-pound (1470 N) load acting conservatively at each of the 121 pressure tube locations. The total force was converted to a uniform equivalent pressure loading on the surface of a simply supported solid plate with equivalent values of modulus of elasticity and Poisson's ratio.

The equivalent properties were determined according to the method of O'Donnel and Langer (ref. 8). For a ligament efficiency (ligament thickness divided by hole spacing) of 0.190, the equivalent Poisson's ratio based on a value of 0.030 for beryllium is 0.097.





The equivalent modulus is 0.13 times the normal beryllium modulus of  $42\times10^6$  psi  $(2.9\times10^7~\text{N/cm}^2)$  or  $5.46\times10^6~\text{psi}$   $(3.76\times10^6~\text{N/cm}^2)$ . For a simply supported plate, the maximum stress occurs at the center, and the radial stress is equal to the tangential stress. The central stress in an equivalent flat plate is 4400 psi  $(3.04\times10^3~\text{N/cm}^2)$ , the average stress in a central ligament of a plate with holes is 23 300 psi  $(1.61\times10^4~\text{N/cm}^2)$ , and the peak stress in the same ligament is 28 800 psi  $(1.99\times10^4~\text{N/cm}^2)$ .

The poison tube holes result in secondary ligaments between these holes and the main holes. An empirical method for determining the stresses for such a situation is given in reference 9. This method consists of multiplying the main ligament stresses by the ratio of the main ligament efficiency to the secondary ligament efficiency. For our case, the latter efficiency is 0.162, and the resulting multiplying ratio is 1.185. These numbers result in an average stress of 27 600 psi  $(1.9 \times 10^4 \text{ N/cm}^2)$  and a peak stress of 34 000 psi  $(2.34 \times 10^4 \text{ N/cm}^2)$  in a centrally located ligament.

Since cooling water is in contact with both flat surfaces of the reflector plate and water flows between the pressure tubes and the pressure tube holes, the temperature gradients in the beryllium will be quite small. An estimate of the radial temperature gradient around a pressure tube hole with 20 watts per gram of heat generation in the beryllium yielded a  $2^{\circ}$  R (1.11° K)  $\Delta$ T. This sort of gradient results in insignificant stresses

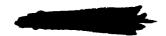
It would, therefore, appear that beryllium forged at 2060° R (1145° K) with the following properties

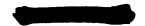
should be adequate for construction of the load carrying reflector plate.

#### FABRICATION OF HEAT EXCHANGER

The reference-design heat exchanger consists of six fine geometry aluminum sections incorporated into the reactor pressure vessel. The tubes are 3/8 inch (0.952 cm) in outside diameter with a 0.035 inch (0.89 mm) wall thickness and are spaced on 0.475-inch (1.21 cm) centers. The tubes are fabricated of 6061-T6 aluminum and are 40 inches (1.016 m) long.

In order to study the feasibility of the reference design from a fabrication standpoint and in order to produce heat exchangers for testing under operating conditions, various methods of producing such devices were investigated. The principal problem in the fabrication was producing the leak-tight joints between the tubes and the tube headers with-





out completely destroying the strength of the heat-treated aluminum.

Calculations made with an assumed tube wall temperature of  $490^{\circ}$  R ( $272^{\circ}$  K) and a shell temperature of  $660^{\circ}$  R ( $367^{\circ}$  K) resulted in a load of 490 pounds (2200 N) and a stress of 12 900 psi ( $8.90\times10^3$  N/cm<sup>2</sup>) in the tubes. It was therefore desirable to maintain the tubes in at least a T4 heat treat condition (21~000 psi ( $1.44\times10^4$  N/cm<sup>2</sup>) yield strength).

Two methods for producing satisfactory joints were developed and both were used to produce 19-tube heat exchangers used in the tests described in section V. WATER FLOW SYSTEM (p. 71). Various views of the completed test devices are shown in figure 19.

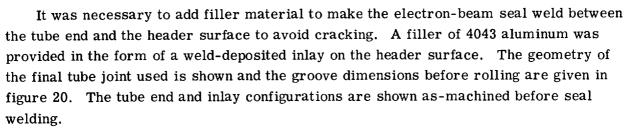
Salt bath brazing was used in the first method to join the tubes to the headers. Tube header thickness was about equal to tube diameters, and 0.003 to 0.005 inch (0.0762 to 0.127 mm) diametral clearance was allowed between the two. A braze alloy of 88 percent silicon was applied as a slurry to each header. Approximately 1/2 inch (1.3 cm) of the adjacent tube length was dipped in a  $1570^{\circ}$  R ( $873^{\circ}$  K) salt bath for 4 minutes. To restore tube strength, the brazed assembly was annealed at  $1350^{\circ}$  R ( $750^{\circ}$  K) for 15 minutes and air quenched. This process was followed by aging at  $810^{\circ}$  R ( $450^{\circ}$  K) for 16 hours. The tubes had strengths comparable to the T4 heat treat condition. The tubes were then straightened by stretching them approximately 0.6 percent, which further increased the tube strength.

The second and preferred method for making the tube to header joint consisted of rolling the tubes into the sheets and then heliarc welding a seal weld at each outer header surface. Tube spacers were also rolled into position on the tubes.

To eliminate the guesswork in rolling and to ensure consistent tube tightness, an available retractive-type tube roller was tried. This type of roller extrudes metal in one direction only as it progressively expands the tube to a fixed inner diameter. Tests were run with single tube-header samples to determine the proper initial clearances and diameters of the header and tube for the strongest joint. Too much expanding or rolling resulted in the rollers binding in the tube and header and having to be cut out, or in flaking of the inner surface. Too little rolling (large header to tube clearance) resulted in weak joints. The strongest joint, which still did not gall the tubes, allowed a 0.006-inch (0.1524 mm) diametral clearance between the outside diameter of the tube and the inside diameter of the header before rolling and an apparent interference of 0.006 inch (0.1524 mm) after rolling.

Two modifications were incorporated to increase the strength of the as-rolled joints. Grit blasting the tube end outer surface and the surface of the hole in the header to a 100-microinch (2.54  $\mu$ m) rms finish resulted in joint strengths of over 1000 pounds (4448 N). When the inside surface of the hole in the header was circumferentially grooved prior to rolling, the tube yielded before the joint loosened.





A 30-kilovolt, 250-milliampere Sciaky electron-beam welder was used with the following parameters:

Voltage, kV
Current, mA
Weld speed, in./min; cm/min
Beam diameter (approximate), in.; mm 0.015; 0.38
Number of passes
Vacuum, torr; N/cm <sup>2</sup>
Focusing coil, in.; cm 1.5; 3.81
Focusing current (dc), A

The seal welding operation reduces the strength of the as-rolled joint. Though the resulting strength of the welded joint is adequate, possible techniques for eliminating this degradation were explored. Rerolling the welded joint after aging at 810° R (450° K) for 16 hours restored as-rolled strength and did not result in loss of sealing or evidence of cracking.

Samples of the principal components of the test heat exchangers shown in figure 21 are the shell, tube header, tubes, and tube spacers. The tube spacers are used to position the tubes with respect to each other and the shell. Sample spacers are shown both on and off the tubes. They are positioned on the tube by rolling the tube in the region of the spacers using the same expander that was used for the header joint. Various prerolling clearances were tried to determine the holding strength and the expansion of the outside diameter of the spacers after rolling. This was done to determine the clearance required for strength and the change in spacer diameter after rolling so that a tight postrolling assembly could be achieved. A clearance of 0.001 inch (0.0254 mm) on the diameter resulted in onset of sliding under a 90-pound (405 N) axial load on the spacer rings and was considered satisfactory. These joints were tested for 10 cycles between 672° R (373° K) and liquid-nitrogen temperature without any loss of strength. Exposure to boiling water for 10 hours increased the joint strength and this increase persisted through the same sort of cycling described previously. The expansion of the outside diameter of a plain ring type spacer with 0.027-inch (0.94 mm) wall thickness is 0.005 inch (0.127 mm).

Figure 22 shows the three different styles of spacers used to keep the tubes sup-





ported in the shell. The six tabbed spacers are used on the central tube in the hexagonal array. The other two types are used in the outer row of tubes. The spacers are arranged in two different cross-sectional patterns, each blocking 20 to 24 percent of the total flow area. The axial distance between the patterns is 2 inches (5.08 cm). Each set of two patterns represents a support point and the sets are arranged so that there are 8 inches (20.3 cm) between support points. Calculations indicated that such a spacing was required to prevent tube instability due to hydrodynamic forces in the exterior water flow.

To prevent the tubes from rotating and twisting during the rolling operation, a slot was machined in the extended tube ends as shown in figure 21. A fixture was made to orient the tube spacers with the slot. The headers were slipped over the tube ends and a comb-type fixture was fitted between the tubes engaging the slots to prevent rotation. The slotted tube end is machined off prior to electron-beam welding.

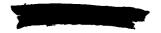
The test heat exchanger fabrication procedure used is as follows:

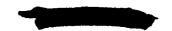
- (1) Fabricate shell, header flanges, complete with 4043 aluminum inlay, tubes, and spacers.
  - (2) Assemble spacers to tubes and roll lightly to hold spacers in position.
  - (3) Assemble tubes and spacers in shell and install headers over tube ends.
- (4) Heliarc weld headers to shell being careful not to overheat components. (After alinement of header in shell, tubes can be disengaged from one header at a time while it is welded to shell.)
  - (5) Roll tubes into headers using fixture to avoid rotation.
  - (6) Finish rolling spacers to tighten bundle in shell.
  - (7) Machine tube and header ends to proper configuration for electron beam weld.
  - (8) Electron beam weld tube ends to header; age and reroll.
  - (9) Finish machine end flanges.

The test heat exchangers successfully operated both at normal conditions and during a larger number of off-design and transient conditions (see section on HEAT EXCHANGER EXPERIMENTS, p. 86). It is, therefore, felt that the incorporation of a fine geometry aluminum shell-and-tube heat exchanger into the pressure vessel structure should be a feasible approach to the system arrangement.

#### **SYMBOLS**

- E modulus of elasticity, psi; N/cm<sup>2</sup>
- k thermal conductivity, Btu/(ft)(hr)(OR); J/(hr)(M)(OK)
- q heat-generation rate, W/g





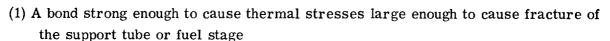
- $\Delta T$  temperature difference across plate thickness,  ${}^{O}R$ ;  ${}^{O}K$
- t plate thickness, ft; cm
- $\alpha$  thermal coefficient of linear expansion, in./in./ $^{\circ}$ R; cm/cm/ $^{\circ}$ K
- $\nu$  Poisson's ratio
- $\Sigma_a$  macroscopic absorption cross section, cm<sup>-1</sup>

#### III. FUEL-ELEMENT ASSEMBLY DESIGN

The general arrangement of the fuel-element assembly is discussed in the section FUEL ASSEMBLIES, and arrangements using both the fine geometry honeycomb and the concentric cylinder designs are shown in figures 6(a) and (b). This section deals with some of the problems associated with the fuel-element assembly and solutions to these problems. The areas of consideration are the structural and vibrational behavior, insulation between the hot fueled material and the aluminum pressure tubes, heat transfer in regions where these components must be bridged for structural reasons, and heat transfer to the propellant. A variety of design and analytical studies and experimental programs have been conducted in these areas. Although the results of all these studies have been taken into account in the reference design, this section treats only part of the total effort on fuel-element assemblies. Additional material is given in references 1, 10, and 11.

#### STRUCTURAL CONSIDERATIONS

The individual fuel stages are positioned axially and radially by a series of radial pins joining them to the axially continuous support tube. The fabrication and assembly of this sort of stage support should pose no problems. Each support tube can be loaded and pinned outside the core before insertion into the pressure vessel. The relative radial expansion between the support tube and the hotter fuel stage should result in no thermal stresses in either member as long as the pins remain free to slide in the fuel stage. At the higher temperature stages, it is likely that some bonding will occur between the pins and the fuel stage unless steps are taken to prevent it. The maximum relative radial growth between the support tube and the fuel stages is near the cooler end of the core where bonding is not as likely to occur. The occurrence of bonding may result in an undesirable situation, such as



(2) A weak bond, repeated fracture of which, as the reactor is cycled through several power operations, causes a galling of the bearing surfaces and subsequent high resistance to sliding

Either of these situations is no worse than the consequences of a design in which no allowance for expansion is initially provided. The possibility does exist that bonding can be prevented by coating one of the contacting surfaces. Tests at  $3860^{\circ}$  R ( $2145^{\circ}$  K) on the compatibility of zirconium oxide and tungsten at a contact pressure of 50 psi ( $34.5 \text{ N/cm}^2$ ) indicates no tendency to bond and no reactions between the two materials after a 2-hour exposure (see section on COMPATIBILITY OF TUNGSTEN AND ZIRCONIA, p. 55).

The support tube which holds the fuel stages is probably the most critical item in the fuel assembly. It is subjected to axial tensile loads resulting from the aerodynamic forces on the stages, bending loads due to lateral forces, and internal pressure loads. It must operate at temperatures from 300° R (167° K) to 4500° R (2500° K). An attempt was made to reduce these loads as much as possible in the hotter regions. By supporting the tube axially at the cold end, the stresses due to the aerodynamic loads were minimized at the hot end. The pressure differential across the tube was minimized at the hot end and also made to act from inside to outside to eliminate buckling. This was accomplished by venting the insulating space outside the tube to core exit pressure and sealing the space at the cold end. The calculated aerodynamic loads on the stages varied from 3 pounds (13.3 N) at the first stage to 20 pounds (88.9 N) at stage 26. The maximum pressure differential across the tube wall is 124 psi (85.5 N/cm<sup>2</sup>) at the first stage. For the 0.015-inch (0.381 mm) wall thickness of the reference design, axial and pressure loads represent small values of stress. The major problem with regard to stresses in the support tube are the bending stresses resulting from lateral loads on the thin-walled tube approximately 55 inches (1.4 m) long.

The lateral loads are the result of maneuvering or vibration. A variety of lateral supports are used in the reference design, one at each end and others at various axial positions. The cold end of the support tube is clamped to the inlet tube sheet of the pressure vessel to carry both axial and lateral loads. At the hot end, the support tube is supported laterally by four lugs which engage slots in a portion of the pressure tube. This arrangement allows for the large relative axial expansion between the support tube and the pressure tube. Figure 23 shows two views of the details of this support. The reference design also incorporates a spring support between the support tube and the pressure tube located approximately 24 inches (61 cm) from the inlet tube sheet. This spring is a corrugated tungsten sheet metal spring whose inside diameter bears on the support tube and whose outside diameter bears on the pressure tube. The sheet thickness is 0.005 inch (0.127 mm) and the spring length is 1.50 inches (3.81 cm) and there are 12 lobes on



the circumference. The calculated operating temperature of the support tube at this axial position is  $2000^{\circ}$  R (1110° K), and the relative radial expansion between the support tube and the pressure tube is only 0.002 inch (0.058 mm). Calculations based on conservative assumptions indicate that resulting stresses are less than 10 000 psi (6.9×10<sup>3</sup> N/cm<sup>2</sup>). Shown in figure 24 are the mechanical and physical properties of tungsten at elevated temperatures used in calculating stresses and determining acceptability of designs. The fact that this stress level offers no problem even if the entire spring reaches support tube temperature has been experimentally verified, as reported in reference 1.

The relative radial expansion between the support and pressure tubes does not present any problem at this location. At the hotter regions of the support tube, the stresses in the spring due to differential expansion become prohibitively large. Therefore, the two additional spring lateral supports located at 34 and 45 inches (86.4 and 114 cm) from the inlet tube sheet (fuel stages 16 and 22) are installed with initial clearance between their maximum diameter and the inside diameter of the pressure tube. This clearance will be set so that the spring engages the pressure tube at operating temperature. In this way, the spring will offer support during reactor operation without having to absorb large relative radial growths. This approach is possible only because vibration tests indicate that the one centrally located lateral support spring is adequate to keep stresses resulting from booster-induced vibrations down to acceptable levels for the support tube at room temperature.

# FUEL-ELEMENT SUPPORT TUBE VIBRATION TEST PROGRAM

Booster induced vibrations are a potential source of damage to the TWMR. Among the reactor components expected to be most susceptible to vibration damage are the fuel-element assemblies and the fuel-element support tubes. Early in this program, room-temperature vibration tests were conducted on mockups of concentric cylinder fuel stages constructed of recrystallized tungsten. Specimens withstood vibration acceleration loads (14 g's) in excess of expected boost phase loads for more than 12 minutes without cracking.

The problem of determining vibration-induced deflection and stresses in the fuelelement support tubes was undertaken both analytically and experimentally (refs. 10 and 11). Since the reactor will not be operating at boost, room-temperature vibration tests were deemed satisfactory for determining behavior during this phase of flight. Test assemblies consisting of the support and pressure tubes and one, two, and three lateral support springs in the annular gap, with and without a water annulus around the pressure tube, were subjected to lateral vibration tests. Stress, as measured with strain gages mounted on the surfaces of the support and pressure tubes, was the index of



operational suitability. These tests demonstrated the feasibility of greatly reducing support tube bending stress at a small sacrifice of increased pressure tube bending stress, as described subsequently.

A search of available large-booster (such as Saturn V) test-program reports yielded information indicating that typical lateral vibration inputs to the booster payloads might range as high as 1 g in magnitude through the frequency band from 5 cps to 2 kcps (5 Hz to 2 kHz). On the basis of the then available data, the following vibration testing levels were adopted:

Frequency band	Input magnitude
5 to 12 cps (5 to 12 Hz) 12 cps to 2 kcps (12 Hz to 2 kHz)	0.0675 in. (1.715 mm) peak displacement (0.172 to 0.993 g peak acceleration) 1.0 g peak acceleration

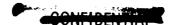
# Description of Test Specimen

The support tube model used in this test program (fig. 25) was designed to simulate dynamically the current reference design. The tube is a stainless-steel - molybdenum - tungsten assembly 54.25 inches (138.8 cm) in length. The materials were joined with silver solder, with the stainless-steel - molybdenum and molybdenum-tungsten joints reinforced by 0.25-inch-wide (6.35 mm), 0.015-inch-thick (0.381 mm) circumferential molybdenum straps.

The 8.5-inch-long (21.6 cm) section of stainless steel at the entrance end of the tube was designed to have the same total mass as the corresponding section of the reference-design tube including the effective mass of the beryllium plug. Twenty-six steel cylinders weighing 0.86 pound (390 g) each were substituted for the fuel stages at the appropriate locations along the tube length. These weights were held in the support tube by two pins whose axes are normal to the direction of shake. They were press fitted into the steel cylinders and were joined to the support tube with silver solder and epoxy reinforcing. This method of supporting the weights afforded certain advantages in fabrication and was considered to be an adequate simulation of the design configuration for these tests for the following reasons:

- (1) Pins located with axes normal to the direction of vibration have little or no direct effect on the lateral rigidity of the support tube even though the pin ends are fastened to it. There is some secondary effect at high lateral displacements due to their tendency to keep the tube round.
  - (2) Strain gage measurements at the positions of maximum stress are not signifi-





cantly affected by local stress perturbations in the vicinity of holding devices located on the neutral axis of the support tube.

The pressure tube used in the test was fabricated from aluminum tubing and had a 2.50-inch (6.35 cm) outside diameter, a 0.060-inch (1.52 mm) wall thickness, and measured 53 inches (1.35 m) in length.

The lateral support springs were formed from 0.005-inch-thick (0.127 mm), 1.0-inch-wide (2.54 cm) tungsten strips by pressing 11 corrugations into each strip and then fastening the ends of the strips together with a staple to obtain a corrugated cylinder with a minimum inside diameter of 2.132 inches (5.41 cm), a maximum outside diameter of 2.38 inches (6.05 cm), and an axial length of 1.0 inch (2.54 cm). Vibration characteristics of such springs are given in reference 1.

A vibration table fixturing scheme was devised whereby the tube was rigidly clamped over its circumference along a 1.0-inch (2.54 cm) axial span at the entrance end and simply supported by a narrow bearing surface located 0.5 inch (1.27 cm) from the exit end. This scheme was considered to be nearly identical to the actual support scheme employed in the then current reference design. The fixture was also designed to afford clamped support to each end of the pressure tube.

### Test Setup and Procedure

The vibration testing of the fuel-element support tube was conducted in two steps. In the first step, a partly instrumented tube was subjected to the specified vibration environment with no lateral support devices along its length and with no pressure tube present to limit displacements. Figure 26 shows the locations of the strain gages and accelerometer for this test. The second series of tests included a more fully instrumented version of the same support tube with the addition of lateral support springs, pressure tube, and a water jacket around the pressure tube. Figure 27 shows the locations of the support tube strain gages and lateral support springs for this portion of the test. The support tube strain gages located at the 2-inch (5.08 cm) station and the accelerometer located at the 30-inch (76.2 cm) station in the first series of tests (see fig. 26) were removed before the second series because of space limitations in the annular region between the support tube and the pressure tube. Figure 28 shows the locations of the strain gages on the aluminum pressure tube.

The holding fixture, shown in figure 29, was designed to have a fundamental natural bending frequency of about 1900 cps (1900 Hz). However, vibration tests conducted on the empty fixture showed the presence of resonant frequencies as low as 480 cps (480 Hz). It was determined experimentally that the fixture was usable to about 1 kcps (1 kHz) by controlling the table input with an accelerometer located at the end of the fixture. With



this mode of table control, both ends of the fixture could be driven in phase at the desired amplitude. Close to 1 kcps (1 kHz), the ends of the fixture began to move out of phase with each other and an amplitude difference was detected. On the basis of fixture and support tube response data up to 1 kcps (1 kHz), it was decided to use the fixture with no major change since no significant support tube resonant responses were expected to be present above 1 kcps (1 kHz). Table 2 presents a list of the equipment used in the test and the usable range of this equipment.

The procedure used in the test runs was to subject the test specimen to the specified acceleration level while sweeping between the 5 cps and 1 kcps (5 Hz and 1 kHz) frequency limits at a rate of 1 octave per minute. The resonant frequencies in this band were detected, and then constant frequency tests at 1 g were run at various frequencies near and at each of the detected resonances. The purposes of this procedure were first to detect all resonances in the band of interest during the sweep and then to ensure a maximum resonant response to the input during the constant frequency dwells.

# Test Results and Analysis

Vibration tests were run as described previously on several different configurations. These configurations included the support tube by itself, the pressure tube by itself, the two tubes together with no lateral support, and the two tubes together with one, two, and three lateral support springs. All the runs except the run with support alone were made with and without water outside the pressure tube. After the three-spring assembly was tested, the spring 36 inches (91.5 cm) from the inlet end was removed for the two-spring run. The only lateral support present in the one-spring test was located 24 inches (61 cm) from the inlet end.

A summary of the first mode resonant response data is given in tables 3 to 5. In addition to the low stress values exhibited in all the tests, even including those in which no lateral support devices were included, several other points of interest can be noted. The mass of the water has a significant effect on the natural frequency of the structural members. The natural frequency of the aluminum pressure tube drops from 154 cps (154 Hz) dry to 42 cps (42 Hz) wet. This tendency is also exhibited in the drop in natural frequency of the entire assembly from about 53 cps (53 Hz) dry to about 39 cps (39 Hz) wet. Also, although the addition of one lateral support spring reduces the stresses in the support tube by a factor greater than 3.0, the addition of two more support springs of the same degree of stiffness into the same central span of the tube has little extra effect on the stress levels. Only the support spring closest to the inlet end of the reference design has the same location as the corresponding spring in the cold tests.

Some calculations were made of natural frequencies to determine conditions of fixity.



#### - CONFIDENTIAL

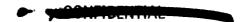
For the case of the aluminum pressure tube by itself, a calculation of natural frequency for the clamped-clamped end support condition resulted in 209 cps (209 Hz). Since this value did not agree with the observed value of 154 cps (154 Hz), a clamped-pinned support case was calculated and resulted in 149 cps (149 Hz). It was therefore concluded that although the fixture was designed for the clamped-clamped support, the aluminum pressure tube was actually being simply supported at the outlet end. The natural frequency of the support tube as a clamped-pinned beam was calculated to be 41 cps (41 Hz). The agreement between this value and the 40 cps (40 Hz) observed confirms that the fixture design in this case did accomplish its objective of clamped-pinned support.

An attempt to determine if the strain gages were actually measuring close to the maximum stress in the support tube was also made by calculations of the stress distribution in such a member under a static loading. For this calculation, it was assumed that there was one lateral support at an axial position 25 inches (63.5 cm) from the inlet end. The spring constant of the resulting composite support was estimated by using a measured static spring constant of the spring devices and the rigidity of the aluminum tube assuming a series arrangement for the two springs. The estimated effective spring constant for this composite support was 1180 pounds per inch (2060 N/cm). The results of this calculation are plotted in figure 30 normalized to the maximum calculated stress. The stresses measured in the test runs involving the dry assembly with and without springs were normalized to each of their maximum measured values and are plotted in the same figure. A comparison of the calculated and measured stress distributions indicates that there are probably no steep gradients in the region of high stresses that are not being picked up by the strain gages. Therefore, the stresses measured in the tests should be close to the maximum, and their low levels indicate satisfactory performance during boost.

While no rigorous error analysis has been made, the worst case accumulation of the maximum inaccuracies specified by the manufacturers of the instrumentation equipment would indicate a possible error of  $\pm 10$  percent in the stresses read on the recorders.

# Spring Constants and System Damping

The spring constants of the pressure tube, the support tube, and the lateral support devices will determine the overall spring constant of the reference-design fuel assembly. While the geometry of the tubes is relatively straightforward, the degree of fixity present in the end supports is not so easy to predict, as shown in the section Test Results and Analysis (p. 31). In the case of the corrugated spring devices used for auxiliary lateral support, the geometry is quite complex, and spring constants are best determined experimentally.



Such testing was done both statically and dynamically, and the results are reported in reference 1. Static loading of corrugated springs resulted in nonlinear spring rates, with values at low deflections much higher than those at moderate deflections. The effective spring rate of the lateral support device in a vibration situation is therefore a constant over a small range of relative deflections between the support tube and pressure tube. The high spring rates of the corrugated devices would tend to result in effectively constant behavior in the presence of low loads or a relatively flexible pressure tube.

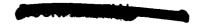
Digital computer calculations (ref. 10) were made of the vibration behavior of one of the mockup fuel assemblies tested. Effective spring constants for the lateral supports were assumed to be about one quarter of the maximum values determined from static and vibration tests on individual springs. The resulting stresses were in the same range as those measured for the same configuration.

Another important characteristic of a vibrating system is damping. Three different types of damping are present: friction, internal material, and viscous damping. Viscous damping is the result of relative motion between the pressure tube and the water moderator. The test results have not been used to determine quantitatively any of these individually or in combination. It is obvious, however, that enough total damping is present to prevent resonant destruction of the fuel assembly under expected boost vibration loads.

### Vibration Tests of Operating Temperature Fuel-Assembly Mockup

The determination that no unreasonable stresses resulted from expected boost vibrations with only one corrugated spring lateral support between the support and pressure tubes was important in the reference design. Since the one support required to be in contact with both the pressure and support tubes during boost is in a relatively cool region of the reactor, differential expansion problems are not severe. Any additional springs required in the hotter regions during operation can be installed with initial radial clearance to avoid destructive thermal stresses when operating temperatures are reached.

Two such additional springs are included in the reference-design fuel assembly shown in figure 5. Room-temperature vibration tests on a mockup of this assembly were also run using essentially the same test setup described in the section Test Setup and Procedure (p. 30). The mockup in this case included a pressure tube support at the orifice plate location (see fig. 5) as well as three corrugated spring lateral supports between the tubes. Materials used for the support tube and springs in the mockup were selected to give the same dynamic properties as the actual members at operating temperature. Springs were fabricated of molybdenum, and the support tube consisted of axial sections of stainless steel of tapering thickness, Monel 400 and 70-percent-copper 30-percent-nickel alloy.





After locating the natural frequency of the assembly, a 1.0-g lateral acceleration was imposed at that frequency, and strain gage measurements were made at various positions along both the support and pressure tubes. Although attempts made at calculating these stresses indicate that higher than allowable stresses will exist (see refs. 10 and 11), such calculations are extremely dependent on assumed values for various types of damping. Results of testing the mockup of the hot support tube showed stresses in a 0.015-inch-thick (0.0381 cm) support tube to be well below the yield point of recrystallized tungsten at operating temperature.

#### INSULATION BETWEEN FUEL ASSEMBLY AND PRESSURE VESSEL

The proximity of high-temperature fuel assemblies and cool water moderator is an inherent part of the basic concept being dealt with. To minimize heat transferred to the water under these large temperature gradients and to maintain reasonable pressure vessel temperatures, insulation between the fuel assembly and the aluminum pressure vessel is necessary. The portions requiring maximum insulation are the pressure tubes and the outlet tube sheet.

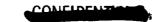
Since gamma heating of any insulating materials increases the heat being transferred to the water, the use of a stagnant hydrogen insulation gap was adopted as the primary insulation technique in both these areas. This section is concerned with the heat transferred through this insulation gap. Since it is necessary to connect the hot and cold parts across the insulation gap in some regions, heat transfer in these regions is also discussed.

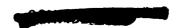
#### Heat Loss to Pressure Tube

A layer of nonflowing gas is maintained for insulation in the annular space between the pressure tube and the support tube. The hydrogen has access to this annulus through an opening located at the outlet end of the fuel assembly. The low thermal conductivity of the hydrogen will maintain a large temperature difference between the support tube and the pressure tube. There is no forced convection; therefore, the modes of heat transfer include conduction, radiation, and free convection.

It is desirable to minimize free convection in order to increase the temperature difference maintained across the insulation gap and also to reduce the uncertainties in calculating heat transfer in the annulus.

A heat-transfer computer program is used for heat-transfer calculations within the fuel assembly, including the heat loss from the support tube to the pressure tube through





the insulation annulus. The program neglects free convection in the annulus. The value of heat loss across the insulation is obtained as a sum of the amounts of heat transferred by radiation and by conduction. It is desirable, therefore, to make separate calculations of the significance of the neglected free convection under the conditions present in the reference design.

This problem is discussed in reference 12 where it is noted that the free-convective heat transfer in a fluid enclosed by two vertical walls is dependent on the height of the fluid layer as well as on its thickness. For situations in which the height of the gap between vertical walls is large compared with its thickness, the heat transfer is equal to that which can be calculated for pure conduction. The following inequality is given as the criterion for such behavior:

$$Gr_{S}Pr < \frac{124}{Pr} (0.952 + Pr) \frac{L_{m}}{S}$$

The value of  $\mathrm{Gr_S}\mathrm{Pr}$  in the reference design varies with axial position since the temperatures of the pressure tube, support tube, and stagnant hydrogen in the gap between them varies along the core length. This product was determined based on the results of calculations discussed in the section HEAT TRANSFER TO PROPELLANT (p. 41) and is plotted in figure 31 as a function of axial length of the fueled zone of the reference design. Earth gravity was used in the Grashof number evaluation.

The plot of  $\mathrm{Gr_s}\mathrm{Pr}$  is shown dashed for axial positions less than 3.75 inches (9.52 cm) from the inlet end of the fueled zone. In that inlet region, the still-cold propellant is keeping the support tube temperature below water temperature. Heat is therefore being transferred from the pressure tube to the support tubes under these circumstances and absolute values of  $\mathrm{Gr_s}\mathrm{Pr}$  are presented in the figure.

The highest value shown on the solid portion of the curve is 2100 at approximately 8.0 inches (20.3 cm) from the inlet end. An evaluation was made of the right side of the given inequality using the design value of  $L_{\rm m}=3.5$  feet (1.07 m) for the fueled region length of the support tube, S=0.01 foot (3.05 cm) and the local value of Pr=0.670. The resulting value, 105 000, being much larger than 2100, indicates that free convection is in fact negligible. This is also true for the position of maximum  $Gr_{\rm S}Pr$  in the inlet region for which a similar comparison was made.

The calculations of the heat transferred from the fuel assembly through the stagnant hydrogen gap, considering only conduction and radiation, showed that relatively small amounts of heat are lost to water. Of the total heat transferred to the gas in all 26 fuel stages of an assembly, 0.15 percent goes into the water. Less than 1.0 percent of the heat produced in the final stage is transferred to the water. The resulting heat flux on





the surface of the pressure tube in the region of the final stage is approximately 80 000 Btu per hour per square foot (9.1×10<sup>8</sup> J/(hr)(m<sup>2</sup>)).

#### Outlet Tube Sheet Insulation

The outlet tube sheet is a critical item in the reactor structure. To minimize mechanical loads on this member, the pressure in the outlet water plenum will be maintained equal to the core exit gas pressure. To minimize internal gamma heat generation, the material is made as thin as is reasonable, 0.125 inch (3.17 mm). It is protected from the hot gas in the nozzle by a tungsten radiation shield, and it is insulated from the radiation shield with a stagnant hydrogen region. Details of this arrangement are shown in figure 5.

A schematic diagram of the region of concern is shown in figure 32. It is apparent that the problem of protecting the aluminum can be divided into two regions. In region A (fig. 32), the tungsten radiation shield, which is heated by the 4460° R (2475° K) hydrogen by a convection process, is able to dissipate energy by radiation to the walls of the nozzle which are at a temperature of approximately 1660° R (922° K). As a result of this mechanism, the aluminum temperature is relatively insensitive to the value of the gasside heat-transfer coefficient and the controlling parameter is the water-side coefficient on the inner aluminum wall.

In region B, the tungsten support tube has a view only of itself, and thus radiation cooling is not available here. Moreover, the water flow on the aluminum side is not restricted by a flow divider at this location. As a result, the local water velocity and heat-transfer coefficient will be less than those existing in that region where a water flow divider is provided.

Initial one-dimensional calculations have been performed to evaluate various configurations that might be employed. However, any of these calculations require a knowledge of heat-transfer coefficients at the gas and water interfaces.

The value of the hot-gas-side coefficient that has been used is the coefficient that will exist at location B in figure 32. This coefficient has a value of approximately 1550 Btu per hour per square foot per  ${}^{O}R$  (3.18×10 $^{7}$  J/(hr)(m $^{2}$ )( ${}^{O}K$ )). The use of this value for region A is probably not correct but will tend to be conservative.

On the water side of the aluminum, determination of heat-transfer coefficients is complicated by the unusual flow geometry for the water. If the vertical sections of the pressure tube are considered, the heat-transfer coefficient due to vertical water flow can be derived from a Nusselt-type correlation:





Nu = 0.023 
$$\left(\frac{DV\rho}{\mu}\right)^{0.8} \left(\frac{c_p \mu}{k}\right)^{0.4}$$

The heat-transfer coefficient for the flow divider geometry can be compared with that without the flow divider:

$$\frac{h_{w, 1}}{h_{w, 2}} = \left(\frac{\rho_1 V_1}{\rho_2 V_2}\right)^{0.8} \left(\frac{D_2}{D_1}\right)^{0.2}$$

$$= \left(\frac{W_1}{A_1} \frac{A_2}{W_2}\right)^{0.8} \left(\frac{D_2}{D_1}\right)^{0.2}$$

$$= \left(\frac{2.47}{3.998}\right)^{0.8} \left(\frac{0.2}{1.146}\right)^{0.2}$$

$$= 0.478$$

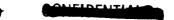
The heat-transfer coefficient to the pressure tube with the flow divider geometry is approximately 4800 Btu/(hr)(ft<sup>2</sup>)( $^{O}R$ ) or 9.84×10<sup>7</sup> J/(hr)(m<sup>2</sup>)( $^{O}K$ ). Thus, an estimate of the coefficient on the water side without a flow divider at location B is 2280 Btu/(hr)(ft<sup>2</sup>)( $^{O}R$ ) or 4.67×10<sup>7</sup> J/(hr)(m<sup>2</sup>)( $^{O}K$ ) for an ideal water distribution.

In addition to the velocity component due to water coming down the flow dividers, the water in the plenum will be flowing radially outward to the edge of the core. This type of configuration has been studied before (ref. 13) but for Reynolds number values lower by 2 orders of magnitude than those existing in the plenum. If these data are extrapolated to our conditions, the correlation used is

$$h_{\rm w} = 370[1 + 0.0067(T_{\rm f} - 460)] \frac{v_{\rm max}^{0.6}}{D_{\rm o}^{0.4}}$$

= 
$$370[1 + (0.0067)(250^{\circ} R)] \frac{(10.4 \text{ ft/sec})^{0.6}}{(2.62 \text{ in.})^{0.4}}$$

= 
$$2750 \text{ Btu/(hr)(ft}^2)(^{\circ}R) \text{ or } 5.64 \times 10^7 \text{ J/(hr)(m}^2)(^{\circ}K)$$



The heat-transfer coefficient that exists on the aluminum surface normal to the pressure tubes is most uncertain. This type of geometry is neglected in the literature; the bulk of work has been concerned with banks of tubes as opposed to the tube sheet holding them together. As an approximation, the same heat-transfer coefficient can be used as exists on the pressure tubes (2280 Btu/(hr)(ft<sup>2</sup>)( $^{O}$ R) or 4.67×10 $^{7}$  J/(hr)(m $^{2}$ )( $^{O}$ K) to be conservative).

If the heat-transfer coefficients having the approximate values just given are used, it appears that there are several means of insulating the tube sheet for protection from radiation (location A in fig. 32). A 0.012-inch (0.305 mm) sheet of tungsten can be used as a radiation shield to dissipate energy to the nozzle walls.

The simplest of the insulating materials that might be employed is a stagnant layer of hydrogen gas as is used to protect the pressure tube in the propellant channels. An analysis is presented in Eckert and Drake (ref. 12) which correlates data taken with stagnant gas between two horizontal parallel planes and permits calculation of natural convection and conduction effects with an effective thermal conductivity.

A calculation of the heat transfer for such an arrangement under the reference conditions indicates that a 0.125-inch-thick (3.17 mm) outlet tube sheet can be maintained below  $760^{\circ}$  R ( $422^{\circ}$  K). Quantities used in this calculation were

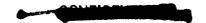
Water side coefficient, Btu/(hr)( $ft^2$ )( $^{\circ}R$ ); J/(hr)( $ft^2$ )( $^{\circ}K$ )	67×10 <sup>7</sup>
Gas side coefficient, Btu/(hr)(ft <sup>2</sup> )( $^{O}$ R); J/(hr)(m <sup>2</sup> )( $^{O}$ K)	$18 \times 10^{7}$
Bulk water temperature, <sup>O</sup> R; <sup>O</sup> K	n. 380
Gamma heating rate in aluminum, Btu/(hr)(ft <sup>3</sup> ); $J/(hr)(m^3)$ 1.94×10 <sup>6</sup> : 7.	$2 \times 10^{10}$

This 0.125-inch (3.17 mm) thickness is adequate to take the 100-psi (69  $\rm N/cm^2$ ) load which is assumed to be required for water circulation during startup and during afterheat removal with no hydrogen flow.

# Heat Transfer Through Lateral Support Devices

Required lateral support devices will have to bridge the insulating gap between the hot support tube and the aluminum pressure tube. Therefore, the possibility exists that the pressure tube will overheat in such regions. An analytical investigation was conducted on the temperature distributions in the vicinity of two different types of lateral support: a light spring and a more rigid support such as the one near the exit end of the fuel assembly.

Because of the complex nature of the heat-transfer problem associated with the lateral support structure, it is impractical (if not impossible) to make accurate calculations without the aid of a multidimensional digital code. For this particular problem, a



steady-state, three-dimensional program using a relaxation technique, was used. This program allows internal heat generation and considers heat transfer by conduction, convection, and radiation, all of which are significant in the lateral support problem.

For an initial study, a generalized V-shaped spring similar to the lateral support was chosen (fig. 33) and the effects of varying the thickness, length, and contact resistance were determined. In these calculations, values of certain items, such as heatgeneration rates and fuel, water, and hot gas temperatures, were assumed to remain constant at levels determined from early reference-design calculations with no springs present.

This analysis was made for a spring located approximately 1 inch (2.54 cm) upstream from the exit of the last stage. The following values were used in the analysis:

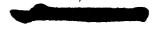
Fuel temperature, <sup>O</sup> R; <sup>O</sup> K
Hot gas temperature, <sup>O</sup> R; <sup>O</sup> K
Water temperature, <sup>O</sup> R; <sup>O</sup> K
Gas gap thickness, in.; mm
Support tube thickness, in.; mm 0.015; 0.381
Pressure tube thickness, in.; mm
Gamma heating in tungsten, $W/g$

The values for fuel and hot gas temperatures were taken from results prior to those shown in figure 39.

Material of the lateral support device and the heat-generation rate were assumed to be the same as those of the tungsten support tube. The minimum grid (node) size, which determines how closely a local temperature can be calculated and how much time a given problem requires on the computer, was chosen to be 0.005 inch (0.127 mm) in the vicinity of the contact point. The location of a given temperature which lies between two nodes (e.g., the aluminum surface temperature) is interpolated to an accuracy of about half this amount (i.e., to about  $\pm 0.0025$  in. (0.064 mm)) and could result in a small discrepancy between the quoted temperature and the value which could be obtained by using a smaller grid size.

Some results of this study are shown in figure 34. For this set of calculations, the dimensions of the lateral support spacer were held constant at t=0.007 inch (0.178 mm) and L=0.600 inch (1.52 cm, see fig. 33). The contact coefficients between the spacer and the pressure tube and between the spacer and the support tube were varied over a range representing the possible values which might occur if there were either perfect contact  $(h=\infty)$  or if a thin gas layer separated the lateral support space from the tubes  $(h\cong 1000 \text{ Btu/(hr)(ft}^2)(^0\text{R}) \text{ or } 2.05\times 10^7 \text{ J/(hr)(m}^2)(^0\text{K}))$ . An intermediate value of contact resistance was also used.

As shown in figure 34, the presence of the support device does not affect the temper-





ature significantly beyond 0.25 inch (6.35 mm) from the point of contact. In the immediate vicinity of the spacer, the temperature rise caused by a spacer with perfect thermal contact is twice as great as that in the case where a contact resistance of  $1000 \text{ Btu/(hr)(ft}^2)(^{O}R)$  or  $2.05\times10^7 \text{ J/(hr)(m}^2)(^{O}K)$  is assumed.

However, the variation in temperature due to variations in contact resistance is  $20^{\circ}$  R ( $11^{\circ}$  K), at most, and the area of pressure tube over  $760^{\circ}$  R ( $422^{\circ}$  K) is about the same in both cases. Since contact resistance is not an important factor, perfect contact can be assumed.

Isothern, showing the temperature variation within the pressure tube for infinite contact coefficient are shown in figure 35. The size of the area of the pressure tube which has a temperature greater than the allowable limit is, therefore, 0.2 to 0.3 inch (5.1 to 7.6 mm) wide (twice that shown in figs. 34 and 35 to account for symmetry) multiplied by the length of the spacer.

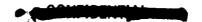
An additional series of calculations was performed using different dimensions for the lateral support device. The results are shown in figure 36 and indicate that considerable improvement is possible if the thickness t of the material is reduced. The effect of changing the characteristic length L of the spacer is not so pronounced, since the longer conducting path is somewhat offset by the increased heat load due to internal heat generation. For example, for the 0.007-inch-thick (0.178 mm) strip, the net heat transferred to the water from all sources was nearly identical for both cases (i.e., L=0.6 and 1.2 in. (1.52 and 3.04 cm)). Thus, the conducted heat in the spacer (i.e., that transferred by conduction from the support tube to the pressure tube) decreased by about the same amount as the additional heat generated in the longer strip (an increase of about 1 percent of the total load) to result in no net change in the heat transferred to the water.

The previous study of the lateral support spring was confined to the exit of the reactor since it was felt that the higher gas and support tube temperatures would produce the highest temperatures. However, to ascertain whether this hypothesis were indeed true, a typical case of the V-spring was analyzed at the point of maximum heat generation. The comparison between the two cases is shown in figure 37 and indicates that the local aluminum temperatures is higher by approximately  $45^{\circ}$  R ( $25^{\circ}$  K) at the exit so that the previous assumption appears to be substantiated.

A variation of the V-spring case can be made by inverting the support so that two points of contact are on the aluminum pressure tube rather than on the tungsten support tube. To investigate this case, the same conditions used in the study shown in figure 37 were applied to the inverted V. The results are shown in figure 38, and when compared with the original case, show that the maximum aluminum temperature for both the V and inverted V are approximately equal.

Several facts are indicated from these analyses regarding the temperatures near lateral support springs:





- (1) Because the aluminum is nearly at the allowable temperature  $(760^{\circ} \text{ R } (422^{\circ} \text{ K}))$  before the introduction of the lateral supports, it is impossible to prevent overheating of the aluminum at least on some local basis.
- (2) The effect of the contact resistance on the aluminum temperature is significant in the vicinity of the point of contact but does not appreciably change the size of the area which has a temperature in excess of  $760^{\circ}$  R ( $422^{\circ}$  K).
- (3) Reducing the thickness of the spacer is a most effective method of reducing the maximum temperature of the aluminum. (It also reduces the size of area which is over the temperature limit.)
- (4) The characteristic length L of the spacer (fig. 33) does not affect the temperature of the aluminum significantly. The increase in the conduction path due to a longer spacer is offset by a corresponding increase in the heat generated within the spacer, with the result that no net change in the heat transfer to the water occurs for nominal changes in the length of the spacer.

No analysis has been made of the three springs in the reference design. The spring thickness is 0.005 inch (0.127 mm) and the spacer length L is approximately 0.6 inch (15.24 mm). The hottest of them is located in the region of stage 22. The gas temperature there ( $3600^{\circ}$  R ( $2000^{\circ}$  K)) is about equal to that assumed in the preceding calculations. Figure 36 indicates that, with no contact resistance, a hot spot temperature of  $785^{\circ}$  R ( $436^{\circ}$  K) can be expected in the pressure tube.

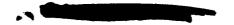
A heat-transfer analysis using a code similar to the one described at the beginning of this section (p. 38) was used to predict operating temperatures in the region of the hot end rigid support shown in figure 23. Details of the calculations are given in reference 10. Results using more recent and lower values of gamma heating indicate a maximum local temperature in the aluminum pressure tube of 763° R (423° K). The increase in insulation gap of stagnant hydrogen in this region below the fuel stages is instrumental in maintaining a low aluminum hot spot temperature despite higher gas temperatures.

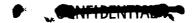
The work performed to date on the heat transfer through both types of lateral support indicates that aluminum pressure tube temperatures can be limited to reasonable values in the reference design.

#### HEAT TRANSFER TO PROPELLANT

Considerable work has been done on heat transfer from the fuel-element stages to the propellant. Most of this work was on the concentric cylinder design for two major reasons:

(1) It was the earliest basic design considered in the program





(2) Its geometry lends itself to a relatively simple one-dimensional calculation in which conductivity is ignored

After calculations at nominal design conditions led to an acceptable design from the heat-transfer standpoint, hot channel calculations were made. These calculations indicated tendencies to overheat the fuel elements, and design modifications were explored for their effect on hot channel factors.

Calculations were also made on the hexagonal version of the fine geometry fuel element in an attempt to assess the magnitude of the thermal gradients.

## Reference Design Using Concentric Fuel Cylinders

The heat-transfer and flow characteristics of a fuel assembly in the present reference design of the TWMR are described by the data shown in table 6 and by those plotted in figure 39. The figure shows several curves obtained from results of calculations made on the highest power fuel assembly, which is located near the core centerline. The computer program used was written by Einstein (ref. 14) and modified by Einstein and others for the cylindrical fuel assembly. As modified, it uses the heat-transfer correlation of Miller and Taylor (ref. 15). The calculations neglect circumferential variations and treat the fuel assembly stage by stage. Stage exit pressures are equalized for all annuli by flow distribution before the next stage is entered. The gas temperature modifications resulting from this redistribution are taken into account. Entrance and exit effects are also included. The curves may be described as follows:

- (1) The axial power distribution along the centerline of the core peaks in stages 8 and 9. It is represented by a curve joining points which give, for each of the 26 stages, the value of the ratio of heat generated in the stage to the total heat generated in the fuel assembly. The curve shows a high value of power in the inlet stage due to the presence of an inlet end beryllium reflector. The shape of the curve and the resulting ratio of peak to average power of 1.46 show the effect of zoning by using a mixture of 70 percent enriched tungsten and 30 percent natural tungsten in stages 12 to 21.
- (2) The distribution of coolant gas temperature among flow annuli at the outlet end of each stage is shown by the series of curves in figure 39(a). For each stage, this figure shows a radial plot of gas temperature out of each annulus, from the innermost flow annulus (at the left of each curve) to the outermost flow annulus (at the right). Gas temperature in the outermost flow annulus is lower than that in the inner annuli due to heat loss through the support tube and through the insulation annulus to the pressure tube and the water moderator. In order to reduce the effect of this heat loss on gas temperature, the widths of the outer flow annuli are reduced, as shown in table 6.
  - (3) A plot of distribution of fuel surface temperature among fuel cylinders at the out-





let end of each stage is also presented in figure 39(a). Each curve is a radial plot with the innermost fuel cylinder temperature at the left and the outermost at the right, and with the unfueled support tube temperature shown by a circle far below the rest of the temperatures for the stage. The support tube temperature is approximately the same as the coolant gas temperature adjacent to it. The series of curves shows that the highest fuel surface temperature,  $4894^{\circ}$  R  $(2720^{\circ}$  K), occurs at the outlet end of stage 22 in the eighth fuel cylinder from the stage centerline.

- (4) The pressure drop curve (fig. 39(b)) shows the difference between pressure at the assembly inlet and that at the stage outlet. Total pressure drop, that plotted at the outlet end of stage 26, is approximately 124 psi (85.5 N/cm²). This value includes momentum and friction pressure drops within flow annuli (amounting to 83 psi (57.3 N/cm²) to 95 psi (65.5 N/cm²) depending on the annulus) and also the contraction and enlargement pressure changes at the ends of all stages. The stage end pressure drops are based on the changes in flow area in entering and leaving the stage, and amount to about one-fourth to one-third of the total pressure drop. A factor is used to allow for an entrance effect in each stage. However, no attempt was made to include the effect of high surface- to bulk-temperature ratios on friction factor.
- (5) The dynamic head of the coolant gas varies not only with longitudinal position in the fuel assembly but also is different in different annuli in each stage. The highest value at the outlet of each stage is the value plotted. This value reaches 13.25 psi  $(9.15 \text{ N/cm}^2)$  at the outlet of stage 26 for the flow annulus next to the innermost annulus. The average for all flow annuli at the outlet of stage 26 is approximately 12.5 psi  $(8.62 \text{ N/cm}^2)$ .

Table 6 indicates uniform flow annulus widths and hydraulic diameters for most flow passages. The annulus adjacent to the unfueled center tube has a lesser width and consequently a lesser flow rate of coolant because the gas receives fission heat from only one side, and less cooling is required. The same situation exists in the outermost flow annulus next to the unfueled support tube. Also, heat is removed from the support tube through the insulation annulus outside it. For these reasons, it seemed desirable to reduce the width and hydraulic diameter not only of the outermost flow annulus, but also of the annulus next inside it. The result was that in the hottest stage (stage 22) fuel surface temperatures were fairly uniform (4817° to 4894° R (2680° to 2720° K)) except for the outermost fuel cylinder which was 4605° R (2560° K). In general, excessive fuel surface temperature on any cylinder may be reduced by increasing hydraulic diameters of adjacent flow passages or by reducing hydraulic diameters of flow passages adjacent to cooler cylinders.

An axial power distribution is shown in figure 40, which is the same as that of the reference design (fig. 39), except that there is no zoning; that is, no natural tungsten is included in any stage. A calculation was made with this power distribution. Table 7





shows a comparison of results with the two distributions. It is seen that zoning reduces the highest fuel surface temperature in the assembly by  $157^{\circ}$  R ( $87^{\circ}$  K). Calculation shows that if the surface temperature obtained with the unzoned distribution ( $5051^{\circ}$  R ( $2805^{\circ}$  K)) can be tolerated, the zoning used for the reference design makes it possible to increase the outlet gas temperature by  $152^{\circ}$  R ( $84^{\circ}$  K). This temperature increase corresponds to an increase in power of 3.7 percent.

## Hot Channel Analysis

The purpose of a hot channel analysis is to establish the effect of manufacturing and assembly tolerances and analytical, experimental, and operational uncertainties on the fuel stage wall operating temperature. The procedure is based on the statistical analysis method (refs. 16 and 17). The given conditions for the problem were

- (1) The concentric-cylinder fuel element and its mechanical design specifications (table 6)
- (2) The fuel-element design operating conditions (table 6)
- (3) The core power, heat transfer, coolant flow, and power and temperature control uncertainties and confidence levels (table 8, together with identifying numbers, n; see pp. 45 to 47 for discussion)
- (4) It is assumed that a set of values for any of the quantities involving uncertainty has a normal distribution about its nominal value.
- (5) It is further assumed that the uncertainties are independent of each other. The main steps in the hot channel analysis are as follows:
- (1) Establishment of hot channel factors for each uncertainty

The hot channel factor is defined as the ratio of the quantity as perturbed by the uncertainty to that same quantity at design operating conditions. Two hot channel factors directly affecting the fuel stage operating temperature are considered here: a coolant bulk temperature rise factor and a wall- to bulk-coolant-temperature difference.

For each quantity n, heat-transfer calculations were made by using the appropriate uncertainty applied to the design value. These results were compared with those obtained by using the design value to yield the hot channel factor.

The number of calculations can be reduced by investigating the effects of parameters whose relation to two or more of the uncertainties can be established. For example, if hot channel factors are calculated for changes in coolant outlet temperature, the results can be applied to items 3 and 4 (see table 8). Similarly, items 7 and 8 can be associated with perturbations in coolant flow rate and items 9 and 10 with variations in radial power distribution within a fuel stage.

(2) Establishment of the standard deviation in wall temperature for each stage First, the variation in wall temperature due to 1 standard deviation in each of the





uncertainties listed in table 8 is calculated by adding the effects on wall temperature of each of the two hot channel factors associated with 1 standard deviation of each uncertainty. The results are shown in figure 41 and are discussed later in this section.

The combined 1-standard-deviation effect of all the individual and independent uncertainties is the square root of the sum of the squares of their individual wall-temperature perturbations (see ref. 18). This combined effect  $\sigma_1$  for each stage is also given in figure 41.

# (3) Establishment of overtemperature probability for each stage

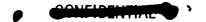
The value of the combined variation in wall temperature associated with 1 standard deviation can be used to establish the probability for any wall temperature variation. For a normal distribution curve of combined uncertainties, these probabilities are given in figure 42 in terms of standard deviations. The probability of a stage reaching any temperature over its design value can be determined by dividing this temperature increase by  $\sigma_1$  for that stage from figure 41. The result, in standard deviations, is used to get the probability from figure 42. As is to be expected, the greater the difference between the design and allowable hot spot temperature, the less likely the occurrence of the overtemperature.

The factors contributing to fuel cylinder wall temperature and considered significant in this analysis are listed in table 8, along with estimates of the percentage uncertainties and assigned confidence levels. As a general rule, items which were subject to inspection and quality control or were obtained from many experimental measurements backed by analysis were assigned a confidence level (99.7 percent) of 3 standard deviations. Those which were specified by calculation, by extrapolated experimental data, or by a limited number of measurements were assigned a confidence level (95.4 percent) of 2 standard deviations.

A completely satisfactory method for arriving at the uncertainty values to be used in this analysis is not known. In the following paragraphs, the considerations are presented which entered into the choice of numbers, together with an indication of the way in which these numbers were used in the calculation.

Fuel assembly power (n = 1). The basic factor involved here is neutron flux, since fuel loading is handled separately (n = 10). If a critical experiment were conducted on each core, a distribution of flux could be obtained by measuring neutron flux density (perhaps by insertion of wires in appropriate locations). On the basis of these results, the fuel assembly orificing could be matched to the flux distribution. A reasonable count of wires could be made with a 2-standard-deviation uncertainty of  $\pm 2$  percent, and other errors such as uncertainty in wire locations might add another  $\pm 2$  percent for a total 2-standard-deviation uncertainty of  $\pm 4$  percent. The effect of any difference in moderator temperature between experiment and design can be computed relatively accurately.

The uncertainty in fuel assembly power would appear, in part, as an uncertainty in



outlet coolant gas temperature. The calculation, therefore, uses an adjusted value of outlet gas temperature. However, the individual fuel assembly considered is in an array with a number of parallel assemblies which are operating at design condition pressure drop. The calculation of the assembly being considered, therefore, uses an adjusted value of gas flow rate to balance the effect on pressure drop due to the adjustment in gas temperature, keeping the pressure drop at design value. The stage gas temperature and the highest wall temperature in each stage with the adjusted temperature and flow conditions is used to find the hot channel factors for the stage.

Heat-transfer coefficient (n = 2). Available data obtained under conditions similar to those in the fuel assembly indicate the heat-transfer coefficient correlation as used for these calculations to be applicable, with about 95 percent of the data falling within  $\pm 15$  percent of the correlation line.

Temperature sensing (n = 3). Outlet gas temperature is the quantity considered. On the basis of thermocouple performance at lower temperature, it was estimated that this temperature might be known to within  $\pm 100^{\circ}$  R (55° K), which is about 2.4 percent of the temperature rise in the assembly, and therefore 2.4 percent of the power.

Power adjustment (n = 4). Power adjustment represents uncertainty in the behavior of a control mechanism, such as its accuracy and speed in returning outlet gas temperature to design value after a disturbance. It is independent of the uncertainty in the temperature sensing (n = 3) by which it operates. It is estimated that the adjustment could be made with a divergence in outlet gas temperature of about  $\pm 50^{\circ}$  R ( $\pm 27.8^{\circ}$  K).

Flow passage width (n = 5). Since each annular flow passage is formed by a pair of adjacent cylinders in the concentric design, deviation in each cylinder results in a variation of flow passage width. These deviations result from diameter variations and from out-of-roundness of the cylinders. The computer program is not capable of treating the circumferential changes in annular flow passage width associated with out-of-roundness. The hot spot factor calculated was one resulting from two adjacent cylinders both oversize by 0.002 inch (0.051 mm). This results in a fueled cylinder with one normal and one undersize passage adjacent to it and the presence of one oversize passage in the same stage which adds to the hot spot effect. The 0.002-inch (0.051 mm) variation used is considered reasonable for the sum of achievable out-of-roundness and diameter tolerances.

Stage power (n = 6). This factor results from the uncertainty in the neutron flux at any particular fuel stage independent of any uncertainty in the total fuel assembly power (n = 1). It was thought that stage power variation might be based on the same considerations as that for the complete fuel assembly (n = 1), and a comparable value was assigned.

Orifice mismatch (n = 7). Orifice mismatch represents a discrepancy between coolant flow rate values, design and realized. It comes from the fabrication tolerance in orifice size and arrangement and is applied to the calculation as an adjustment of gas flow





rate, together with an adjustment in outlet gas temperature which will keep the fuel assembly power equal to design power. The power equality is maintained because power, or heat generation rate, depends on neutron flux and fuel, and does not change because of nondesign flow rate. Fuel assembly pressure drop changes with change in flow rate so that total pressure drop, through both fuel assembly and orifice, is equal for all parallel assemblies.

Orifice design data are fairly complete and well established. The only estimated uncertainty value for which it is thought that information is adequate to allow a 3-standard-deviation confidence level is the one for orifice mismatch.

Upper plenum pressure distribution (n = 8). The uncertainty in upper plenum pressure distribution results in an uncertainty in coolant gas flow rate for a particular fuel assembly which appears because of a possible difference between its inlet pressure and that of other assemblies. It is assumed that outlet pressure is the same for all assemblies. A variation at the inlet depends on arrangement of inlet gas plenum components and connections. Its value is an estimate subject to experimental tests.

Power distribution among fuel cylinders (n = 9). The uncertainty here is the same as that which would appear in measurements of heat-generation rate for a given thickness of fuel at a given radius. The reference design is based on radially uniform power generation within each stage. Neutron flux and spectrum calculations were made to determine fuel loadings which would result in uniform power. Uncertainties in these calculations result in variations in power generation over and above those due to fuel loading manufacturing errors. The uncertainty value might be based on the same considerations as that for the power in the complete fuel assembly (n = 1) and that for stage power (n = 6).

Fuel loading (n = 10). The uncertainty here is in the amount of fuel in a particular cylinder of the stage being computed and arises due to variations in fabrication. Both total volume of the cylinder and the composition of the fueled matrix are involved. The amount of fuel can be controlled to about  $\pm 1$  percent by volume. For a 20-percent uranium dioxide fuel this would be an uncertainty of about  $\pm 5$  percent with a 3-standard-deviation confidence level, and for a 30-percent uranium dioxide fuel it would be an uncertainty of about  $\pm 3$  percent with a 2-standard-deviation confidence level.

As shown in figure 41, all factors result in uncertainties which, near the assembly inlet, vary rapidly with longitudinal position. Some factor uncertainties change with longitudinal position throughout the assembly, namely, heat-transfer coefficient, flow passage width, stage power, cylinder power, and fuel loading. Others are almost unvarying throughout the downstream two-thirds of the assembly. In the upstream half, the uncertainty that has the greatest effect on surface temperature is that in the heat-transfer coefficient. In the downstream half, the most troublesome uncertainty is that in fuel assembly power because wall-to-bulk temperature differences are relatively small and the





heat-transfer coefficient is consequently relatively less important, while the gas temperature rise and total heat added to the gas are becoming large.

Overtemperature probability was computed, as previously explained, for stage outlet locations only with an allowable hot spot temperature of  $5500^{\circ}$  R ( $3055^{\circ}$  K). These locations are those where stage temperatures are highest. The results are given for each stage in figure 43. The first 9 stages do not contribute to overtemperature probability, and stages 22 and 23 are the greatest contributors. An integration of probabilities over the fuel assembly results in a combined probability of  $1.05 \times 10^{-3}$ . In other words, one would expect an overheated stage in 1 out of every 951 fuel assemblies or 1 out of every 8 complete cores. These calculations were based on the highest power assembly. Since the probabilities would be lower for the lower power assemblies in the outer region of the core, these values are conservative for the values given in table 8.

Additional calculations were made to explore the effect of possible design changes on the likelihood of overheating. A new hot channel analysis was made for the reference design with its length increased to 29 stages instead of 26. This 11.5 percent increase in length reduced the heat flux by the same ratio, thus reducing surface temperatures throughout the fuel assembly and reducing the highest surface temperature by  $61^{\circ}$  R  $(34^{\circ}$  K).

The 29-stage hot channel analysis was simplified by using stage outlet hot channel factors derived from the factors obtained for the 26-stage analysis. The 26-stage outlet factors were plotted against distance from the inlet as a fraction of total length. Then the new values were read at the new stage outlet positions. The results are shown in figure 44. It is obvious that increasing the length by only three stages has had a large effect on overtemperature probability. Under these circumstances only 1 stage in every 8800 assemblies or 75 complete cores can be expected to exceed 5500° R (3055° K).

Increasing the length of the core, already discussed, reduces the overtemperature probability but increases core weight roughly in proportion to the increase in length. Therefore, it was desirable to examine other methods of reducing overtemperature probability.

Estimates were first made of the effect of reducing hydraulic diameter by examining the change in surface temperature with change in diameter at the hottest point in the reactor for the reference design. These results were used to select three combinations of hydraulic diameter and mass velocity, and the temperatures in the entire fuel assembly were calculated to determine the maximum temperature.

The calculations to estimate the effect of hydraulic diameter used the referencedesign flow rate together with heat flux and bulk coolant temperature at the hottest point in the reference-design fuel assembly. It was assumed that the changes in flow area and heat-transfer surface area accompanying any reduction in hydraulic diameter were the same as those resulting from the same reduction in diameter of a round tube. This



assumption greatly simplified the determination of these quantities because the radii of cylinders and flow passages changed as hydraulic diameter was reduced. Figure 45 presents the results of these calculations.

A reduction in fuel-element surface temperature of 61°R (34°K) was achieved by lengthening the fuel assembly from 26 to 29 stages. In order to achieve the same results by reducing hydraulic diameter while maintaining coolant flow rate, figure 45 indicates that a 13-percent reduction to a hydraulic diameter of 0.110 inch (2.8 mm) is required.

If this were done without changing the number of annuli, the overall diameter of the fuel assembly would be smaller. If, however, the space recovered were occupied, for example, by an eleventh fuel cylinder and a twelfth annulus, the fuel surface area for heat transfer would be greater by about 9 percent. The cross-sectional area for coolant flow would be slightly smaller due to additional blockage by the eleventh fuel cylinder.

Use of such dimensional changes could be supplemented by changes in fuel assembly power and coolant flow rate, keeping coolant temperature distribution unchanged, if such changes appear to be advantageous.

The following three combinations of conditions may be considered as alternative to increasing reactor length to 29 stages. Changes are based on values which apply to the concentric-cylinder reference design, and are listed as follows:

## Case I - Reduction of hydraulic diameter by 13 percent:

Hydraulic diameter, percent
Overall fuel assembly diameter, in.; mm
Wall surface area, percent7
Coolant flow area, percent
Coolant flow rate, percent
Coolant temperature, OR; OK
Power, percent
Heat flux, percent
Coolant flow per unit area, percent
Heat-transfer coefficient, percent
Highest fuel wall temperature. OR: OK65; -36.1
Overtemperature probability
Pressure drop, percent
Outlet dynamic head, percent

Except for overtemperature probability, these are approximate values obtained by calculating an array of concentric cylinders arrived at by reducing all reference-design hydraulic diameters by 13 percent. No hot channel analysis was made, but since fuel wall temperature was reduced by about the same amount here as for the case with



11.5 percent increase in length, it was assumed that overtemperature probability here would be reduced in a similar manner. This assumption is tentative, and needs verification with a hot channel analysis for each case to be considered.

This reduction in wall temperature was obtained at the expense of a large increase in dynamic head, which was already near an upper limit for concentric cylinders in the reference design. Furthermore, reduction in hydraulic diameter constitutes reduction in annulus widths where cylinder surfaces already are so close as to make spacing variations allowed by tolerances to become an important factor in determining fuel wall temperature.

The addition of an eleventh fuel cylinder and twelfth flow annulus to case I geometry restored the overall fuel-assembly diameter of the reference case and reduced dynamic head. The changes relative to values for the reference design are listed as follows:

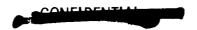
Case II - Reduction of hydraulic diameter by 13 percent and addition of one fuel cylinder:

Hydraulic diameter, percent	13
Overall fuel assembly diameter, in.; cm	. 0
Wall surface area, percent	
Coolant flow area, percent	
Coolant flow rate, percent	
Coolant temperature, <sup>O</sup> R; <sup>O</sup> K	0
Power, percent	0
Heat flux, percent	
Coolant flow per unit area, percent	5
Heat-transfer coefficient, percent	e e
Highest fuel wall temperature, <sup>O</sup> R; <sup>O</sup> K	50
Overtemperature probability	-4
Pressure drop, percent	9.4
Outlet dynamic head, percent	44
,, persons	14

Again, the values are approximate results of calculating an array of concentric cylinders, except for overtemperature probability which is an estimate. There is a penalty in pressure drop and dynamic head, although smaller than for case I. Also, the same problem exists as for case I involving excessively small widths of some annuli.

If the coolant flow is increased in the geometry of case  $\Pi$  so that the heat flux is the same as in the reference design, conditions, relative to those of the reference design, are listed as follows:





#### Case III - Case II geometry with 9 percent increase in coolant flow:

Hydraulic diameter, percent
Overall fuel assembly diameter, in.; cm
Wall surface area, percent
Coolant flow area, percent
Coolant flow rate, percent
Coolant temperature, <sup>o</sup> R; <sup>o</sup> K
Power, percent
Heat flux, percent
Coolant flow per unit area, percent
Heat-transfer coefficient, percent
Highest fuel wall temperature, <sup>O</sup> R; <sup>O</sup> K
Overtemperature probability
Pressure drop, percent
Outlet dynamic head, percent

These results, compared with case II, show that the gain in power is accompanied by a slight rise in fuel temperature and a considerable increase in outlet dynamic head.

The preceding three sets of calculated results were compared with and discussed relative to the concentric-cylinder reference design. Since, for this design, outlet dynamic head is limited to a value below those computed for these three cases, the changes suggested are unacceptable for concentric cylinders. However, in the fine geometry array, much higher values of outlet dynamic head can be allowed because of the more rigid structure. The results of any of the three calculations are probably generally applicable to the fine geometry and indicate acceptable approaches using such fuel stages. It is possible that overtemperature probability might be reduced still further by reducing hydraulic diameter more than 13 percent, or power might be increased further, keeping overtemperature probability at  $10^{-4}$  and hydraulic diameter at the 13 percent reduction. Such conclusions, as stated here, are subject to verification by further calculation, including hot channel analyses. The minimum permissible hydraulic diameter for the fine geometry type of fuel element depends on fabrication and inspection possibilities.

# Performance of Honeycomb Fuel Assembly

It was desired to make calculations which would yield the heat-transfer and flow characteristics of a fuel assembly using a honeycomb of fueled material with hexagonal flow passages for cooling, as shown in figure 46. For such an array, circumferential variations are important. Although a computer program was available which would



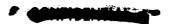


handle the variety of flow passage conditions appearing in the array, it could not take into account the effect of conduction in the webs of the honeycomb.

Therefore the one-dimensional heat-transfer computer program for concentric cylinders was modified to make calculations, including wall conduction, on a geometry which would simulate the hexagonal array. In order to make a realistic approximation to the hexagonal geometry, each flow annulus between two concentric cylinders was assumed to be divided into such a number of flow passages as to give each flow passage the same hydraulic diameter, flow area, and surface area for heat transfer as each passage in the corresponding ring in the hexagonal array. This division was assumed to be made by an appropriate number of radial fuel plate ligaments connecting the two cylinders. A one-dimensional, radial calculation of conduction across each annulus from cylinder to cylinder through the equivalent ligaments was introduced by multiplying the thermal conductivity of the fuel by the ratio of fuel plate ligament thickness to ligament spacing in the annulus.

For the actual hexagonal fuel array enclosed and supported by an unfueled round support tube, the flow passages adjacent to the support tube must provide a transition between the two geometries. The modified concentric cylinder model was arranged so that, in this transition region, it could simulate the irregular fuel walls extending out from the hexagonal array at its outer circular periphery. Fueled ligaments, connected to the outermost fuel cylinder and extending radially outward toward the support tube, represented these in the model. Simulation of performance was accomplished by duplicating the hydraulic diameter, flow area, and surface area averaged over the unlike passages at the periphery of the honeycomb.

The design investigated for the hexagonal array was one for which the hydraulic diameter of each hexagonal flow passage was 0.119 inch (3.02 mm). There were six complete rings of hexagonal flow passages surrounding the center passage, and a seventh ring in which each corner hexagon was open to the outer flow region bounded by the support tube, as shown in figure 46. Thus, there were 163 passages with a 0.119-inch (3.02 mm) hydraulic diameter. The outer flow region consisted of a number of partial hexagons all opening into an annulus which separated the support tube from the butt ends of the fuel walls. For the reference design, this annulus had a width of 0.005 inch (0.127 mm) so that the hydraulic diameter of the composite passage was 0.107 inch (2.72 mm). However, calculations were made for a range of annulus widths from 0 to 0.030 inch (0 to 0.762 mm), with corresponding hydraulic diameters from 0.105 to 0.133 inch (2.66 to 3.38 mm), since fabrication tolerances may cause large variations in this dimension. Although radial conduction was computed for the ligaments in all interior annuli, in the outer flow region the ligaments were assumed not to make thermal contact with the unfueled support tube, and therefore provided no conductive heat transfer to the support tube.





In general, calculation results for the hexagonal array design case are not greatly different from those for the concentric-cylinder reference design. Although the highest fuel wall temperature is about  $100^{\circ}$  R (55.6° K) higher, the radial power distribution had not been optimized for the hexagonal design. Also, the general trends of longitudinal variations are similar to those shown in figure 39 for the concentric-cylinder reference-design case.

Figure 47 shows the calculated average effects (using the modified code for concentric cylinders with conducting ligaments) of changing the width of the outermost annulus. One plotted curve shows the effect on the highest computed value of fuel surface temperature, which for all four points occurs in the innermost cylinder of the twenty-third stage from the inlet end. An increase in annulus width and flow area of the outer flow region allows more of the gas to flow through this region. The flow rates in the inner passages and, therefore, the heat-transfer coefficients, are reduced as the annulus next to the support tube is widened, so that the temperatures of the inner fuel surfaces must rise. For the reference hexagonal design, with a hydraulic diameter of 0.107 inch (2.72 mm) in the outer annulus, the highest fuel surface temperature in the assembly is about 4980° R (2770° K).

The other plotted curve in figure 47 shows the effect of changing the width of the outer flow region annulus on the highest temperature difference in the assembly between adjacent cylinders. This is a measure of the temperature gradient which must be supported by the fueled ligaments. This highest temperature difference occurs in all cases between the two outermost fueled cylinders. An increase in the annulus width and flow area of the outer flow region provides additional cooling for the outermost fuel cylinder, lowering its temperature, increasing the temperature difference between it and the adjacent fuel cylinder, and increasing the temperature gradient across the fuel plate ligaments joining them. The maximum temperature difference between cylinders for the design investigated is 250° R (139° K).

The previous calculations were based on the average heat-transfer and flow characteristics of the irregular passages. To investigate the variation of any of these passages from their average, a revised version of the MCAP digital program (ref. 5) was used. This code allows for a variation in number and size of passages and calculates the thermal characteristics of each type of passage by balancing the pressure losses across each stage to determine the flow distribution among channels.

For the first set of calculations, the number and size of the irregular passages were varied. The assumption was made that the total cross-sectional area of these irregular passages remained constant regardless of the size, shape, and number of channels studied. In addition, the number (area) of nominal channels was kept constant for all the runs at a value corresponding to that for the reference-design hexagonal array.

Figure 48 shows the results obtained for the initial calculations and indicates that the



relative number of various size irregular passages has little effect on the thermal performance of such passages. We therefore can conclude that the larger number of nominal channels (relative to irregular passages) is the controlling factor on pressure drop. A modification to this calculation method was made to obtain more accurate results. It was originally assumed that all the flow passages in the peripheral region had a ratio of heat-transfer surface area to total surface area of 0.75. The surface temperatures calculated were therefore average surface temperatures for a given passage including both fueled and unfueled surfaces. To obtain the actual temperature of the fueled surface, the difference between the average surface temperature and the gas temperature should be corrected by the ratio of heat-transfer to total surface area for each passage. Thus,

$$T_{w}^{t} = T_{b} + \frac{T_{w} - T_{b}}{\frac{A_{s}}{A_{t}}}$$

where  $T_W'$  is the corrected value. Figure 49 gives the results of these calculations for a planned hexagonal design in which the equivalent diameters of the irregular passages varied from 0.059 to 0.125 inch (1.5 to 3.15 mm), and the radial clearance between the fuel and support tubes was 0.005 inch (0.127 mm). The indicated variation in surface temperature among the different passages of  $2500^{\circ}$  R (1390° K) is large and is a potential source of trouble even though the intercell conductivity neglected in these calculations would reduce the calculated gradients.

It also appears that the size of the smallest irregular passage should be greater than one-half a full hexagon for which D=0.072 inch (1.83 mm) and  $A_{\rm S}/A_{\rm t}=0.6$  to avoid overheating of its surfaces.

A possible means of improving the thermal characteristics of the irregular channels in the periphery of the hexagonal fuel array would be to rotate the fuel elements from stage to stage intentionally. In this manner, the gas leaving a hot channel of one stage would not enter the same type of irregular channel in the next stage, and the accumulation of overheated passages would be minimized.

Since there is usually  $30^{\circ}$  symmetry in hexagonal fuel elements, a  $15^{\circ}$  rotation might be accompanied by enough radial flow in the space between stages to keep gas temperature in all channels close to average. While there would be no real assurance that sufficient interstage mixing would occur without performing some tests of this nature, the maximum effect of rotation can be simulated analytically by assuming that complete mixing does occur. Figure 50 shows the result of such a calculation in which two representative types of channels (D = 0.080 in. (2.03 mm) and D = 0.120 in. (3.05 mm)) were rotated so that the exit gas from one channel became the inlet gas for the other channel in the next stage and vice versa for the entire length of the reactor core. Also shown in

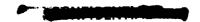


figure 50 are the results obtained for no rotation; that is, the irregular passages of one size were alined for all stages.

Mixing between stages will reduce even minimal differences in temperatures between channels. Techniques for improving mixing can therefore be considered as a means of smoothing the variation between channels.

Although it appears that the possible difficulties indicated by the analysis may be overcome, a search for an alternate fine geometry was initiated to circumvent the problems. The origins of the difficulties lie in the difference in shape between the stage basic hexagonal structure and the round support tube. The ring and ligament design previously discussed and shown in figure 6(c) was evolved as a result of these and other considerations. In this design, the hydraulic diameter of the passages in any row can be varied as in the concentric-cylinder design, and there are no irregular passages at the outside between the support tube and the fueled stage. This configuration then should reduce the thermal stresses to which the rigidity of the fine geometry type of element is susceptible if its fabrication presents no severe problems.

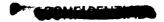
# COMPATIBILITY OF TUNGSTEN AND ZIRCONIA

There are several regions in the fuel assembly in which contact between hot components and cooler members is necessary for structural support. To prevent bonding and to reduce heat conduction in these locations, it may be possible to use thin layers of zirconia ( $\rm ZrO_2$ ) deposited on portions of the fuel assembly. Since regions of possible interest may experience temperatures as high as  $4000^{\rm O}$  R ( $2220^{\rm O}$  K), a test was conducted to study the compatibility of tungsten and plasma-sprayed  $\rm ZrO_2$  in hydrogen at approximately this temperature and under bearing loads.

A test was set up wherein a layer of  $\rm ZrO_2$  was plasma sprayed onto a tungsten substrate which had been cleaned in hydrogen at  $3460^{\circ}$  R ( $1920^{\circ}$  K) for 1/2 hour. A weighted tungsten contact surface (pins) and an unweighted tungsten contact surface (disk) were assembled, as shown in figure 51. A compressive load of 50 psi ( $35~\rm N/cm^2$ ) resulted from the weighted tungsten contact surface. This assembly was then slowly heated, in about  $1/2~\rm hour$ , to  $3860^{\circ}$  R ( $2145^{\circ}$  K) in a hydrogen atmosphere flowing at 20 standard cubic feet per hour ( $0.5685~\rm m^3/hr$ ), and held at temperature for 2 hours. The assembly was subsequently furnace cooled to room temperature in about  $1/2~\rm hour$ .

There was no visual indication of reaction between the  ${\rm ZrO}_2$  and either the weighted or unweighted tungsten contact surface. The  ${\rm ZrO}_2$  did not spall, as may be seen in figure 52.

However, metallographic examination did reveal a third phase at the  ${\rm ZrO_2}$ -tungsten interface. This third phase appears to have been molten at test temperature and to have



# S CONTINUE TO THE PARTY OF THE

penetrated into the tungsten grain boundaries (fig. 53(a)). Examination of a similarly coated tungsten specimen (see fig. 53(b)), which was not tested, indicated that this third phase was present prior to the high temperature test and probably resulted from the plasma-spraying process.

The third phase seen in figure 53(b) was found to be a metallic contaminant of Ni-Cr. This contaminant was the result of electrospark etching of the tungsten surface with a Ni-Cr electrode prior to application of the  $\rm ZrO_2$ . Such roughening is necessary for adherence; therefore, a tungsten electrode was used in preparing the surface of the next sample. This procedure modification completely eliminated the undesirable third phase, and after testing there was no evidence of contamination or reaction between the  $\rm ZrO_2$  and tungsten (see fig. 54(a)).

On the basis of the results it would appear that surface preparation is of primary importance when  ${\bf ZrO_2}$  is applied to a tungsten surface by a plasma-spray technique. In the areas where adequate roughening was attained, the adherence of the  ${\bf ZrO_2}$  was good (fig. 54(a)), whereas the areas where little or no roughening resulted, the adherence was poor (fig. 54(b)).

There does not appear to be any reaction between the  $\rm ZrO_2$  and the tungsten after 2 hours at  $3860^{\rm O}$  R (2145° K) in flowing hydrogen. The 50 psi (35 N/cm²) compressive load did not appear to affect the  $\rm ZrO_2$ -tungsten interface adversely. Therefore, it would appear that  $\rm ZrO_2$  plasma sprayed on tungsten could withstand 2 hours at  $3860^{\rm O}$  R (2145° K) in hydrogen without spalling or a reaction occurring.

Methods of application other than plasma spraying should be considered for applying this insulation barrier in order to obtain a more adherent coating, for example, troweling or a slurry dip. If, however, plasma spraying is used, extreme care must be exercised in substrate preparation to preclude contamination and to ensure uniform roughening for good overall adherence.

## **SYMBOLS**

A flow area, ft<sup>2</sup>; cm<sup>2</sup>

A<sub>s</sub> heat-transfer area, ft<sup>2</sup>; cm<sup>2</sup>

A, total surface area, ft<sup>2</sup>; cm<sup>2</sup>

c<sub>p</sub> specific heat, Btu/(lb)(OR); J/(kg)(OK)

D hydraulic diameter, in.; mm

 $\mathbf{D}_{\mathbf{O}}$  outside diameter of pressure tubes, in.; cm

Gr<sub>s</sub> Grashof number based on insulation gap width,  $\left[g\rho^2\beta S^2(T_s - T_p)\right]/\mu^2$ , nondimensional

### P CONFIDENTIAL

acceleration directed along axis of annulus,  $\mathrm{ft/sec}^2$ ;  $\mathrm{m/sec}^2$ g contact coefficient between spacer and plates, Btu/(hr)(ft<sup>2</sup>)(OR); J/(hr)(m<sup>2</sup>)(OK) h heat-transfer coefficient, Btu/(hr)(ft<sup>2</sup>)(OR); J/(hr)(m<sup>2</sup>)(OK) h<sub>w</sub> thermal conductivity, Btu/(sec)(ft)(OR); J/(hr)(m)(OK) k characteristic length of spacer, in.; cm  $\mathbf{L}$ minimum length of insulation gap for suppressing free convection, ft; m  $L_{m}$ Nusselt number, hD/k, nondimensional Nu identifying number for hot channel factors, nondimensional n Prandtl number,  $c_{p}\mu/k$ , nondimensional Prinsulation gap thickness, ft S stress s maximum stress smax bulk temperature of gas, OR; OK  $T_{b}$ film temperature, <sup>O</sup>R; <sup>O</sup>K  $T_f$ maximum surface temperature,  ${}^{0}R$ ;  ${}^{0}K$ Tmax wall temperature, OR; OK  $T_{w}$ wall temperature, corrected, OR; OK  $T_{w}^{\prime}$ thickness of lateral support spacer, in.; cm t velocity, ft/sec; m/sec V maximum velocity, ft/sec; m/sec  $v_{max}$ water flow rate, lb/sec; kg/sec W coefficient of expansion, 1/OR; 1/OK β viscosity, lb/(ft)(sec); kg/(m)(sec)  $\mu$ density, lb/ft<sup>3</sup>; kg/m<sup>3</sup> ρ standard deviation in wall temperature due to combined factors,  ${}^{O}R$ ;  ${}^{O}K$  $\sigma_1$ Subscripts: 1 no flow divider present

2

flow divider present

# • COMPLEGIALITY

## IV. REACTOR CONTROL

#### REFERENCE SYSTEM

The reference control system concept (see figs. 1 and 4) allows for variation of nuclear reactivity in the reactor by adjusting the concentration of a neutron absorbing salt dissolved in water and circulated in a separate flow circuit in the reactor. Maximum pressure and temperature in this loop are 600 psi (414 N/cm $^2$ ) and approximately 660 $^0$  R (367 $^0$  K). The following basic problem areas are associated with the control system:

- (1) Selection of poison salt
- (2) Selection of materials of construction
- (3) Determination of consequences and extent of gas generation in the solution
- (4) Determination of consequences and extent of thermal and radiolytic effects and on the stability and solubility of the solution

In addition to these basic problems, the engineering design and performance of the reference control system were investigated. The results of this work are reported in references 19 to 23 and indicate general feasibility of such a system with regard to response time, component design, temperature control, and flexibility of operation.

#### Selection of Poison Salt Candidates

In the selection of poisons for use in the aqueous control system of the TWMR, the following properties of the poison candidates were considered:

- (1) Neutron absorption cross sections
- (2) Solubility in water
- (3) Corrosiveness to materials of construction
- (4) Thermal stability
- (5) Radiation stability

Compounds of boron, cadmium, samarium, gadolinium, and europium were considered because of their high absorption cross sections. Based on solubility and radiation stability considerations, only sulfates, borates, and halides were regarded as potential anion candidates. The halides were eliminated because of their corrosiveness. The primary poison compound candidates were

- (1) Boric acid
- (2) Cadmium sulfate
- (3) Gadolinium sulfate
- (4) Europium sulfate
- (5) Samarium sulfate



A literature survey indicated that all the poison candidates or their isotopes have sufficient solubilities to be used in the chemical control system. However, the rare earth salts are less desirable because they hydrolyze to form insoluble poison compounds. This characteristic is undesirable because it could reduce the effective amount of control and permit a situation to exist which might lead to a nuclear accident. This potential accident is discussed in the section Thermal and Radiolytic Stability of Poison Salt (p. 62). Cadmium sulfate also exhibits a tendency to form insoluble compounds, but to a lesser extent than the rare earth salts. Therefore, boric acid and cadmium sulfate were selected as the two poison candidates.

Cadmium sulfate was used as the primary poison candidate with boric acid as a 'backup' candidate for the following reasons:

- (1) The alpha particles released from the  $B^{10}(n,\alpha)Li^7$  reaction contribute to water decomposition and gas evolution. Calculations show (see ref. 24) that the hydrogen partial pressure may be as high as 600 psia (414 N/cm<sup>2</sup> abs). In-pile experiments at high neutron fluxes (comparable to those in TWMR) would be required to demonstrate feasibility. Cadmium is not an alpha emitter.
- (2) In the thermal energy region, the neutron absorption cross section for boron is inversely proportional to neutron velocity. This contributes to a positive temperature coefficient of reactivity which is undesirable. Cadmium does not have this property (non-1/v absorber).

#### Selection of Materials of Construction

Several materials were investigated as potential structural material candidates for the poison control system; aluminum, zirconium alloys, and stainless-steel alloys. Preliminary experiments (refs. 24 and 25) indicated aluminum adsorbed up to about 750 micrograms of cadmium per square centimeter of surface area. Stainless steel is less desirable for use in the reactor core than either aluminum or Zircaloy because of its relatively high neutron absorption cross section. Although no information was available on Zircaloy corrosion under conditions expected in the TWMR, a literature survey (ref. 24) indicated that stainless steel and Zircaloy are generally more corrosion resistant than aluminum. Therefore, Zircaloy was selected as the primary structural material for incore use and stainless steel or Zircaloy were selected as potential out-of-core materials.

#### Gas Generation

Hydrogen and oxygen are generated in the control solution as a result of radiolytic





decomposition of the water. Hydrogen is generated as a product of the aqueous corrosion of the materials in the system. Excessive accumulation of these gases causes the following problems:

- (1) Solution pump cavitation and flow reduction
- (2) Overpressurization of the system
- (3) Power perturbations due to formation of voids

The consequences of the effects of pump cavitation have not been investigated experimentally. However, some estimates of the effects on fluid flow of 0.5 percent weight fraction of undissolved gas as water vapor were made (see ref. 19). These estimates indicated that the required pressure drop in components of the control system would be 1.5 to 2 times greater than the single-phase pressure drop. The subsequent flow reduction might be as much as 30 percent. The existence of two-phase slug flow in the core region would cause reactivity and neutron flux perturbations.

Excessive gas could also cause abnormally high system pressures. The control system is designed to operate at a total pressure of 600 psia (414 N/cm $^2$  abs) both at 100 percent power and during shutdown. If the mole fraction of hydrogen in the system is greater than  $5.5\times10^{-4}$ , the gas will start to be evolved forming voids in the solution. The control system concentrate tank and pressurizer are equipped with displaceable bladders which could permit small increases in system volume at 600 psi (414 N/cm $^2$ ) total pressure. When this volume is filled with gas at 600 psi (414 N/cm $^2$ ), any further increase in gas generation will cause an increase in total system pressure. Total control system internal pressure is shown in figure 55 as a function of hydrogen generated in the poison solution. The flat portion of the curve represents gas generation in the system up to saturation and displacement of the bladders to a volume of 3 gallons (1.14×10 $^{-2}$  m $^3$ , design bladder capacity). Beyond this concentration of gas, the total system pressure increases at constant volume possibly causing damage to the control system structure.

Any void formation in the control system could cause some displacement of poison solution from the reactor. This loss of solution affects reactivity in two opposing ways:

- (1) The moderator is displaced from the control system causing a loss of reactivity.
- (2) The neutron absorber is displaced from the system causing an increase in reactivity.

The net effect is an increase in reactivity. An estimation of the reactivity change due to void formation is shown in figure 56. The reactivity effect is small and since gas generation takes place over a long period of time, compensation by poison concentration will present no problem.

If the mole fraction of hydrogen in the control system is limited to  $5.5 \times 10^{-4}$ , the saturation value at 600 psia (414 N/cm<sup>2</sup> abs), all the problems discussed previously will be avoided.

The gas generation due to water radiolysis was investigated (ref. 25), and the extent





of corrosion product gas evolution was experimentally determined (ref. 22). The amount of hydrogen and oxygen produced during water radiolysis was estimated by postulating probable chemical and radiochemical reactions, determining rate constants for these reactions, and solving the chemical kinetics equations by using a computer. The most conservative estimates of gas generation indicate that the mole fraction of hydrogen in the system is about  $1\times10^{-4}$ . The oxygen content is about 2 orders of magnitude less. Although these estimates have not been experimentally verified, they are the best available at this time.

Corrosion tests were performed duplicating, as closely as possible, the range of operating conditions expected in the TWMR. Three types of such experiments were undertaken:

- (1) Flask: Solutions and materials were exposed to atmospheric pressure,  $675^{0}$  R (375° K) temperature, and solution pH of 1 to 7. These experiments provided rapid and inexpensive results for early screening of material candidates.
- (2) Autoclave: Temperatures and pressures up to  $860^{\circ}$  R (478° K) and 600 psia (414 N/cm<sup>2</sup> abs) were obtained with materials and solutions.
- (3) Loop: The effects of solution velocity and heat flux were investigated, and the thermal condition associated with 100 percent reactor power operation was simulated.

The ranges of operating parameters investigated in these tests are summarized in table 9. The amount of corrosion per unit area of material was determined by measuring the change in weight of material specimens and dividing the weight change by the surface area. The experimentally measured weight changes were used to calculate the total hydrogen content of the water based on the following corrosion reactions:

$$Zr + 2H_2O \rightarrow ZrO_2 + 2H_2$$

$$3 \text{Fe} + 4 \text{H}_2 \text{O} \longrightarrow \text{Fe}_3 \text{O}_4 + 4 \text{H}_2$$

The pertinent experimental results indicate the following types of behavior:

Loop tests: The average weight gain for Zr-2 specimens subjected to an  $810^{\circ}$  R ( $450^{\circ}$  K) solution and a heat flux of 75 000 Btu/(hr)(ft<sup>2</sup>) or  $8.52\times10^{8}$  J/(hr)(m<sup>2</sup>) for 90 hours is 16 milligrams per square centimeter. This weight gain corresponds to a hydrogen generation of  $1\times10^{-3}$  mole per square centimeter.

Autoclave tests: The average weight gain for Zr-2 specimens subjected to water at  $810^{\circ}$  R ( $450^{\circ}$  K) and zero heat flux for 500 hours is 0.5 milligram per square centimeter. This weight gain corresponds to a hydrogen generation of 0.31×10<sup>-4</sup> mole per square centimeter. After about 300 hours of exposure, there was no additional increase in weight.

Even after 500 hours exposure to the same conditions, however, the stainless-steel



specimens continued to increase in weight. Because the TWMR may be shut down for about 2 years, rather than 500 hours, it is necessary to extrapolate the experimental data from 500 hours to 2 years. The following empirical correlation was postulated to relate stainless-steel metal attacked,  $\Delta W$  in milligrams per square decimeter, to water temperature, T in  $^{0}R$ , and exposure time,  $\theta$  in hours:

$$\Delta W = 90\ 000\theta^{0.26}\ \exp\left(\frac{-8460}{T}\right); \ \left[\Delta W = 90\ 000\theta^{0.26}\ \exp\left(\frac{-4700}{T}\right)\right]$$

After a 2-year exposure at  $760^{\circ}$  R ( $422^{\circ}$  K) water temperature (maximum water temperature expected when reactor is shut down), the hydrogen generated from stainless-steel corrosion is  $4\times10^{-4}$  mole per square decimeter.

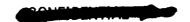
About 55 percent (ref. 22) of the hydrogen generated at the Zr-2 surface reacts with the surface to form hydrides, and only 45 percent dissolves in the water. The surface areas of stainless steel and Zr-2 in the reference system are 2260 and 2460 square decimeters, respectively, and the total system volume is 0.104 cubic meter. Therefore, the mole fraction of hydrogen in water due to corrosion of both stainless steel and Zr-2 is  $3.5\times10^{-4}$ , and the total due to corrosion and radiolysis is  $4.5\times10^{-4}$ . This value is about 18 percent below the solubility limit of  $5.5\times10^{-4}$  and indicates satisfactory operation.

# Thermal and Radiolytic Stability of Poison Salt

It is desirable to keep the poison salt in solution to prevent its deposition on metal surfaces in the reactor core. Cadmium sulfate, the primary poison salt candidate, might be removed from solution by precipitation or by ion exchange with the walls of the control tubes. The extent of cadmium deposition must be limited because it could restrict the margin of effective control and could cause a power excursion if all the deposited cadmium were suddenly sloughed off the tube walls and swept out of the reactor. Obviously, this assumption is extremely conservative. The consequences of such an incident are illustrated in figure 57. Here the maximum temperature attained after the cadmium is sloughed off all the tube walls is shown as a function of the initial cadmium deposition and the percent enrichment of the isotope cadmium 113.

The data shown were calculated as follows:

- (1) The reactivity worth of natural cadmium was determined from criticality experiments in a mockup of the TWMR using cadmium nitrate (ref. 26).
- (2) The cadmium worth for different enrichments with isotope cadmium 113 was calculated by using the thermal absorption cross sections for natural cadmium and cadmium 113.



- (3) The maximum fuel temperature increase was calculated as a function of reactivity insertion on an analog computer by using the model described in reference 27. Reactivities were inserted as ramps with a characteristic ramp time of 0.7 second, the transport time of the poison solution through the reactor core.
- (4) The cadmium "self-shielding" is assumed to be negligible; that is, the reactivity worth of cadmium on the control element walls is the same as if the cadmium were homogeneously mixed with the poison solution.

Also shown in figure 57 is the assumed limiting maximum temperature rise in the reactor ( $100^{\circ}$  R ( $55.5^{\circ}$  K)), which corresponds to a reactivity insertion of 0.035 percent  $\Delta k/k$ . If the reactivity worth of cadmium deposited on the control elements must be limited to 0.035 percent, the cadmium deposition must be limited to about 0.8 microgram per square centimeter. Greater amounts of deposition could be tolerated if the cadmium 113 enrichment were reduced. For example, about 6 micrograms per square centimeter of natural cadmium would be worth the same as 0.8 microgram per square centimeter of 90 percent cadmium 113 enrichment.

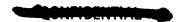
When cadmium is deposited on the tube walls, the effective margin of control is reduced. For example, as poisons build up in the reactor, such as xenon and samarium, cadmium must be removed from the control system to maintain criticality. About 6 percent  $\Delta k/k$  (ref. 26) worth of cadmium must be removed to override these poisons. Any part of this 6-percent- $\Delta k/k$  worth which is present as deposited cadmium could not be removed.

The same tests used to study gas generation due to corrosion were used to determine the extent of thermal instability of the cadmium sulfate in unirradiated solutions. The range of operating variables tested is summarized in table 9. In these tests the same metallic specimen was used to determine corrosion and cadmium deposition. Other experiments (ref. 28) that use electrons from a Van de Graaff accelerator were conducted to determine the stability of the cadmium sulfate solutions in a radiation environment. Electrons were used to simulate the reactor environment (neutron and gamma) because no reactors were available which could duplicate the dose rates expected in the TWMR control systems (150 W/cm³) and Van de Graaff experiments are generally less expensive than in-pile experiments. Calculations (ref. 25) also indicated that for the same dose rate, the Van de Graaff experiments would produce conservative (equal or greater instability) results.

The thermal instability test results indicate that

- (1) The cadmium deposition on the heated Zr-2 surfaces is about 1.3 micrograms per square centimeter  $\pm 150$  percent (1 standard deviation) for a solution temperature of  $810^{\circ}$  R ( $450^{\circ}$  K).
- (2) At temperatures of  $810^{0}$  R ( $450^{0}$  K) and less, the cadmium deposition did not increase with exposure (between 100 and 500 hr).





- (3) Cadmium deposition on stainless steel is generally 2 to 10 times greater than that on Zr-2 surfaces.
- (4) Large amounts of cadmium residue were found in the test loop and autoclave compared with the amount found on specimen surfaces.

The radiation stability test results indicate that

- (1) The cadmium deposition on Zr-2 surfaces is 1.0 microgram per square centimeter  $\pm 22$  percent (1 standard deviation).
- (2) The deposition can be reduced by lowering the solution pH. For example, the deposition might be reduced by a factor of 3 if the pH of the solution is reduced from the unadjusted value (pH  $\approx$  6) to a value of 2.0.
- (3) Some of the cadmium redissolves when the radiation is stopped (reactor shutdown).

The total cadmium deposition (2.3  $\mu g/cm^2$  ±150 percent) due to thermal and radiolytic instabilities was estimated by summing the depositions obtained from tests just described. For 90 percent enriched cadmium sulfate solutions, this amount of deposition could cause a fuel temperature increase of nearly 300 R<sup>O</sup> (167 K<sup>O</sup>) if the sloughing accident occurred. The fuel temperature rise could be held within limits by reducing the cadmium 113 enrichment to about 20 percent. Figure 58 shows the cadmium concentrations required for hot critical and shutdown reactor conditions as a function of cadmium 113 enrichment. If the cadmium 113 enrichment is reduced from 90 to 20 percent, the hot critical concentration of total cadmium in solution would have to be increased from 1.4 to 4.8 milligrams per cubic centimeter, and the shutdown concentrations would have to be increased from 1.9 to 6.2 milligrams per cubic centimeter. The effects of this increase in concentration on the extent of gas generation and stability would have to be experimentally investigated.

Other methods of reducing the severity of the sloughing accident are

- (1) Precoating the control elements with cadmium depleted in cadmium 113
- (2) Reducing the solution pH by adding sulfuric acid
- (3) Providing an auxiliary fast-acting control device which would reduce reactor power and fuel temperatures before the fuel temperature limit is reached

# GAS CONTROL SYSTEM - METHOD OF FABRICATING CONTROL ELEMENT

Another method of controlling reactivity in the TWMR utilizes helium 3 as a neutron absorber (ref. 29). Reactivity is varied by changing the density (pressure) of helium held in control elements uniformly distributed throughout the reactor core. Two types of gas control element geometry are discussed in reference 29: interstitial, in which the gas is held in control elements placed in the interstitial region between fuel elements





(fig. 59(a)); and circumferential, in which the gas is held in control elements which completely surround a fuel element (fig. 59(b)). The interstitial element is constructed with two concentric aluminum tubes to form an annular gas passage. These tubes are interconnected by aluminum distribution ducts at the exit end of the core for transporting helium to and from the reactor core. The circumferential elements of interlocking hexagons surround each fuel assembly.

The circumferential or hexagonal control element offers simplicity of fabrication and structural strength as potential advantages over the interstitial concept. The hexagonal control element design incorporates a pattern of thin aluminum ribs on the inner or gasside surface to aid in heat removal and to reduce the temperature rise across the gas. These ribs absorb the kinetic energy of the protons and tritons produced in the  ${}_{2}\mathrm{He}^{3}\left({}_{0}\mathrm{n}^{1},{}_{1}\mathrm{p}^{1}\right)$ ,  ${}_{1}\mathrm{h}^{3}$  reaction and reduce heat generated in the gas. This rib pattern occupies 20 percent of the space between walls. A perspective view of the interlocking hexagonal control elements including the rib pattern is shown in figure 60.

A 2- by 3-inch (5.08 by 7.62 cm) section of the wall of a typical circumferential control element was fabricated from aluminum to demonstrate fabrication techniques. The ribs were chemically etched in a 0.060-inch-thick (1.52 mm) aluminum plate leaving a 0.020-inch (0.51 mm) plate with a 0.040-inch (1.02 mm) fin height, as shown at the right in figure 61. Another 0.020-inch-thick (1.02 mm) plate was used as the mating wall. The two surfaces were seal welded and the fin surfaces were spot welded to the mating surface by using an electron beam welder. One of the two assembled test cells is shown at the left in figure 62. The tube shown was used for leak testing.

One test cell was internally pressurized to 125 psig (86.2 N/cm $^2$  gage) and a "helium sniffer" was used to detect any helium leaking outside the cell. The cell was also externally pressurized with 500 psig (345 N/cm $^2$  gage) helium and the 1/8-inch (3.2 mm) cell line was examined to detect internal leaks. No leaks were detected and post-test visual examination revealed no damage.

A second test cell was subjected to the same external pressure test, and no leaks occurred. During the internal pressurization test, however, helium was detected after pressurizing to 75 psig ( $52 \text{ N/cm}^2$  gage). Post-test examination indicated the spot welds in the central region of the cell were misplaced and did not contact the fins. Some spot welds in the peripheral region of the cell which were correctly positioned failed, rupturing the skin and causing the leak. These cells were only visually examined prior to testing. These pressure tests were used to indicate the quality of the fabrication technique. In normal operation, the moderator pressure is higher than the gas pressure and there will be no load on the spot welds. Even if the moderator pressure were lost, the internal gas pressure is no greater than 60 psi ( $41.4 \text{ N/cm}^2$ ). It would appear that the fabrication techniques employed to produce these samples are basically satisfactory for a flight system.



#### STUDIES OF OTHER CONTROL SYSTEMS

The control systems previously described offer a great deal of reactor performance advantage since each fuel element is symmetrically surrounded by control devices producing little or no circumferential power distortion. In addition, since regulation occurs by uniform variation of the amount of absorber in these devices, the axial and radial power distribution is not perturbed.

However, to determine the penalties incurred by the use of a control system which cannot fulfill these goals, a study has been made of systems employing mechanical control devices. Some of the results from the heat-transfer portion of this study are presented in this section.

In determining the thermal characteristics of a nuclear reactor utilizing a mechanical control system, several assumptions are necessary in order to compare its performance with a reactor using a control system in which the poison is uniformly distributed. Basically, the assumptions require that the total hydrogen flow rate and total reactor power be held constant. This will ensure that the mixed mean gas temperature and specific impulse remain constant for all systems considered. The core length, pressure drop, etc., can then be used as a measure of the merit of such control systems.

Another assumption which was made throughout this study was that the hydraulic characteristic of all the flow passages in a fuel element were the same (i.e., equal equivalent diameters). Because any deviation from this condition must be superimposed on the reactor using either liquid or mechanical control, consideration of the problems associated with nonuniform flow passage hydraulic diameter (discussed in the section Performance of Honeycomb Fuel Assembly, p. 51) was not necessary for the purpose of this study.

# Thermal Analyses of Reactors with Push-Pull Control Rods

In a nuclear reactor that uses push-pull control rods, there are several methods of rod programming or fuel zoning by which the necessary reactivity can be achieved. Heat-transfer calculations were made for some of these methods of reactor control as listed in table 10. In each case, 19 control rods were distributed within the core, as shown in figure 62.

One of the inherent problems in push-pull control rod systems in which rods enter from the inlet end of the core systems is the resulting axial power distribution. Figure 63 shows comparisons between the reference design axial power distribution and those associated with the three cases listed in table 10. In each of the rodded core situations, the relative power in the exit portion of the core is higher than that for the refer-





ence design. Higher surface temperatures will probably result in that region for the same absolute power level. To reduce the local absolute power level, core length or core diameter must be increased to achieve a given total core power. Increasing the length results in higher pressure drops. Increasing the diameter, for the same power and flow rate, reduces the heat-transfer coefficient between the gas and metal and therefore tends to defeat the purpose of the size increase.

Circumferential power variation in individual fuel elements is another problem which may cause difficulty in a core controlled by push-pull rods. It can be seen in figure 62 that, for axial portions of the core in which rods are present during operation, the power will be depressed in the circumferential portion of the fuel elements adjacent to the control rods. Figure 64(a) shows an experimentally determined power distribution for such a situation (ref. 30). An additional source of circumferential power variation may be water-flooding of the space vacated by the rods as they are withdrawn from the core. This flooding would occur if the water moderator were used to cool the control rods and a dynamic seal were not achievable. Figure 64(b) shows the experimentally determined power distribution in a fuel element if the space vacated by the adjacent control rod were occupied by water (ref. 30).

As a result of the nonuniform circumferential power distribution associated with the push-pull control rods, the temperature rise of the coolant in the various passages of the fuel element is quite varied. The coolant in those passages having the greater power level is heated to higher temperatures than is the coolant in the passages in which the power is lower. This higher coolant temperature, coupled with the higher heat flux which also exists in these passages, results in local fuel temperatures which are significantly greater than would occur if there were no circumferential power distortion. To reduce the temperature of these hot spots to an acceptable level, the size of the reactor core must be increased over and above the increase required because of the axial power distribution previously mentioned.

Since circumferential variations in power must be taken into account in rodded cores, a different computer program than that described in the section Reference Design Using Concentric Fuel Cylinders (p. 42) was used which includes such power variations. Results for the reference design, with uniform power circumferentially, shown in figure 65, agree quite well with those shown in figure 39.

The first series of calculations on a push-pull control rod system was made on the unzoned, single-bank configuration, case 1 (see table 10). These calculations neglected circumferential power variations in order to get the separate effect of axial power distribution. The results are shown in figure 66 and indicate that a core length in excess of 48 inches (122 cm) is required to keep surface temperatures at or below  $5000^{\circ}$  R ( $2780^{\circ}$  K). A core length of 58.5 inches (148.5 cm) resulted in a maximum wall temperature of  $4870^{\circ}$  R ( $2710^{\circ}$  K).





Similar calculations for case 2 (see table 10), which has two fuel zones, resulted in about the same maximum surface temperature for a 58.5-inch (148.5 cm) core. No such calculations were made for case 3 (see table 10) because circumferential power variations will necessarily exist in the high temperature regions of the central area of the core, as indicated in figure 63(c).

All the remaining calculations were performed by using the circumferential power distributions given in figure 64 at the appropriate core axial positions. This presupposes that it is not possible to keep water from filling the vacated control rod space.

The results for an unzoned core, case 1, are shown in figure 67 for three different core lengths, 58.5, 105, and 132 inches (148.5, 266.5, and 335.5 cm). For the 58.5-inch (148.5 cm) core, surface temperatures are more than 850  $R^{O}$  (473  $K^{O}$ ) higher than those in which circumferential power variation was not considered. Even the 132-inch (335.5 cm) core experiences fuel temperatures 200  $R^{O}$  (111  $K^{O}$ ) higher than the reference design core. The extent of the mismatch between the flow rate and the power in particular passages is indicated by the maximum outlet gas temperature of approximately  $5150^{O}$  R ( $2860^{O}$  K) compared with the mixed mean outlet gas temperature of  $4460^{O}$  R ( $2480^{O}$  K). Additional evidence is presented in figure 68 in which the thermal performance of a passage adjacent to the control rod is compared with that of a passage  $180^{O}$  away from a rod. A difference of about 1000 R $^{O}$  (555 K $^{O}$ ) exists in outlet gas temperatures and in surface temperatures in the 58.5-inch (148.5 cm) core.

Much the same sort of behavior would exist in the two-zone core. Figure 69 shows the behavior of passages adjacent to and  $180^{\rm O}$  from the control rod for a 58.5-inch-long (148.5 cm) core, case 2. Figure 69(a) is calculated for the axial power distribution which would exist at the beginning of core life (see fig. 63(b)). Figure 70 shows the results of calculations for the end of core life rod position ( $\Delta k/k$  1.7 percent higher than the beginning of life). The maximum fuel temperature in this case in 150 R<sup>O</sup> (83.4 K<sup>O</sup>) higher than in the beginning of life case probably for two reasons: the first is the large power spike in the more highly loaded region of the core as the rods are withdrawn; the second is the greater length of the core affected by water flooding the control rod space.

The heat-transfer performance of the two-rod bank core, case 3, is much worse than that of the other two cases (cases 1 and 2). Results of calculations on a 58.5-inch-long (148.5 cm) core are presented in figure 70. Here again performance of a passage adjacent to and  $180^{\circ}$  from a control rod is shown. These results are for a fuel element in the outer region. The rods in this vicinity would be completely withdrawn during the entire operating life of the reactor. The axial power distribution is essentially a chopped cosine, as shown in figure 63(c). High fuel-element temperatures exist accompanied by extreme temperature differences among the passages both on the surfaces and in the gas. This behavior results from the presence over the entire length of the outer core region of the circumferential power variations associated with flooded control rod positions.



As stated earlier, all these calculations were made for a core containing 19 control rods. If many more less absorptive rods were used, the circumferential power variation and the accompanying poor performance would be greatly improved. Such an arrangement, of course, would present mechanical and space problems. Another method of improving performance of rodded cores is to induce a large amount of mixing in the axial space between stages. In this way, the cumulative effect of the circumferential power variations would be reduced. The ultimate in this mixing chamber approach would be complete mixing between stages. A heat-transfer calculation was made by assuming this condition for a 58.5-inch-long (148.5 cm) core, case 2. The results are shown in figure 71 and indicate maximum fuel-element temperatures of about  $4700^{\circ}$  R ( $2610^{\circ}$  K). This value is  $900 \text{ R}^{\circ}$  ( $500 \text{ K}^{\circ}$ ) below the calculated value for limited mixing shown in figure 69(b).

It is not obvious what sort of effective mixing device should be inserted between fuelelement stages to realize this performance improvement in rodded cores. Obviously, penalties will be involved in core pressure drop and axial length requirements.

The computer program used in the calculations presented thus far in this section neglected conduction in the fuel-element material. The large thermal gradients calculated with normal mixing in the 1/8-inch (3.2 mm) axial gap between stages would result in some conductance tending to reduce the temperature differences in a given fuel-element stage. The results of the previous calculations on the end-of-life condition for the two-fuel-zone arrangement were used as the starting point for a multidimensional heat-conduction calculation. These results included convective heat-transfer coefficients as well as gas and surface temperature distributions. Figure 72 compares the results of the conduction calculation with those in which conduction is ignored. The maximum difference in fuel-element temperature between the two results is about 200 R<sup>O</sup> (111 K<sup>O</sup>) even with the large overall gradient that exists. These results indicate that, in the presence of high convective heat-transfer coefficients, conduction has only a small effect in equalizing fuel-element temperatures.

As a result of the thermal analysis performed on reactors for nuclear rocket application employing only push-pull type control rods, the following conclusions can be drawn:

- (1) The effect of axial power distribution alone is an increase in the required length of the reactor of 30 to 50 percent relative to the reference-design core where a uniformly distributed liquid poison control system is used.
- (2) When the circumferential power distribution resulting from a reasonable number of control rods and water-flooding of vacated rod spaces is considered, the required core length becomes extremely large.
- (3) The use of interstage mixing devices is an effective means of reducing the undesirable effects of circumferential power variation. In the limit, complete mixing between





each stage will yield results approaching those for a circumferentially uniform power distribution. For such a case, the size disadvantage of the rodded cores would be that associated with axial power distribution (item (1)). It is not obvious, however, what form such a device should take and what additional length and pressure drop penalties would be involved.

(4) As a first approximation, the effect of conduction on fuel-element surface temperatures may be neglected. In general, discrepancies less than 200  $R^{O}$  (111  $K^{O}$ ) result from ignoring conductance for a reasonable design.

# Thermal Analysis of Reactors with Combination Drum and Rod Control

One way to overcome the axial power problem associated with rodded cores is to use rods to provide shutdown requirements only and to use external drums to supply the remainder of the reactivity swing requirements. Under these circumstances, the rods are completely withdrawn during operation, and the axial power distribution can be the same as that for the reference-design core. The only variation in power distribution over the operating life of the reactor will be that due to control drum rotation.

The thermal problems associated with a nuclear reactor which uses both drums and rods are somewhat different from those encountered in a reactor which uses only rods or a uniform poison for control. Normally, to obtain maximum power output of the reactor, the hydrogen flow distribution among cells is tailored to match the radial power distribution. For perfect matching of flow to power, the mixed mean exit gas temperature of each individual fuel element is exactly the same and is equal to the chamber temperature of the nozzle. Under drum control, a shift in the radial power distribution will occur as the drums revolve from the all-in to the all-out position. Overheating and overcooling of various fuel elements will accompany this shift, depending on the relative location of an element within the reactor. The exit gas temperature of the fuel elements cannot be equal at all drum positions because of the power shift, and the chamber temperature will be equal to the mixed mean temperature of the total hydrogen flow rate.

Table 11 shows the shift in power for two specific fuel cells in the drum controlled core, the center cell and one near the side reflector where the drums are located. These two cells represent the highest and the lowest power cells in the reactor core.

It is obvious that if the hydrogen flow is tailored based on the drums-in condition, the peripheral element will overheat considerably because of the 44.5-percent increase in power which occurs when the drums are rotated to the all-out position. A more logical approach would be to tailor the flow based on the drums-out power distribution since the positive shift in power for the center cell (16.4 percent) is less than in the alternate method.



To compensate for the mismatch of power and flow which is caused by drum rotation, it is necessary to reduce the total power output of the reactor until the maximum surface temperature criteria ( $5000^{\circ}$  R ( $2780^{\circ}$  K)) is achieved. Figure 73 summarizes the results of an analysis performed on the drum core with the initial flow tailoring based on the drums-out condition. It can be seen that the reactor power would need to be reduced by approximately 15 percent to achieve a maximum surface temperature of  $5000^{\circ}$  R ( $2780^{\circ}$  K) in the center cell. It can also be seen that, under this reduced power condition, the peripheral fuel element is considerably overcooled with a maximum surface temperature of  $3230^{\circ}$  R ( $1795^{\circ}$  K).

While the exit gas temperature of the center cell is approximately equal to the normal design chamber temperature ( $4460^{\circ}$  R ( $2480^{\circ}$  K)), the mixed mean chamber temperature has dropped to  $3850^{\circ}$  R ( $2140^{\circ}$  K) at the reduced (15 percent) power level as a result of the much lower gas temperature of the overcooled peripheral elements in the drums-in condition.

It would, therefore, be necessary to operate the reactor at a power reduced by 15 percent when the drums are in the all-in position; the reactor power could be gradually increased to the full-power full-temperature condition as the drums are rotated to the all-out position.

The amount of power reduction required to operate the reactor at the drums-in condition depends on the reactivity held down by the drums. In the TWMR reactor, a significant amount of xenon override capability was included. If mission analyses indicated that less override capability is necessary, the drums-in allowable power level could be increased.

## V. WATER FLOW SYSTEM

In the TWMR, the water serves several functions. First, it serves as a nuclear moderator for the reactor. In addition to this important function, the water also acts as a coolant and is the chief reason that a low-temperature metal (i. e., aluminum) can be used as a structural material so close to the hot propulsion gas.

Lastly, by virtue of the heat added to the coolant as it flows through the reactor, the incoming hydrogen may be preheated by utilizing a heat exchanger in which the energy is extracted from the water. The additional heat thus added to the hydrogen brings the temperature of the cryogenic fluid to a level compatible with a full topping cycle, or a combination topping-bleed cycle.

Obviously, a satisfactory design could more easily be achieved if an unlimited coolant (water) flow rate were available. Such a large flow rate would, however, require an excessive amount of pumping power and larger pumping equipment and would be detri-



# CONFIDENTIAL

mental to the performance of the system, particularly if the propellant gas used to drive the water pump turbine were discharged overboard as it is in the reference design. It would appear, therefore, that for optimum efficiency of the system the minimum coolant flow rate commensurate with an acceptable design should be used.

To obtain a proper balance between performance and efficiency, the following criteria must be satisfied under all operating conditions:

- (1) The water must have a low enough temperature and a sufficient velocity to provide adequate cooling of the necessary structural members.
- (2) The water temperature must be high enough to prevent freezing in the cryogenic hydrogen-to-water heat exchanger.

Since the amount of energy absorbed by the water as it flows through the reactor depends on the construction and nuclear characteristics of the system, the independent variables by which the criteria can be met are limited to the flow rate of the water and the design of the heat exchanger. The dependent variable, the operating temperature of the water, can be controlled by the proper choice of the two independent variables but is directly limited by the choice of structural material used in the design.

Although the maximum aluminum temperature is  $760^{\circ}$  R ( $422^{\circ}$  K) in the TWMR concept,  $735^{\circ}$  R ( $408^{\circ}$  K) was chosen as a nominal design objective. Therefore, the water temperature must be less than  $735^{\circ}$  R ( $408^{\circ}$  K). At the other end of the scale, the minimum water temperature must be greater than  $492^{\circ}$  R ( $273^{\circ}$  K) to prevent freezing. This temperature range ( $492^{\circ}$  to  $735^{\circ}$  R ( $273^{\circ}$  to  $408^{\circ}$  K)) can be refined by additional analysis to the point where an optimum choice of operating temperature and heat-exchanger design can be made.

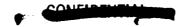
#### HEAT SOURCES IN WATER SYSTEM

To establish the proper operating temperature and flow rate for the water, it was necessary to perform a detailed analysis of the entire system. Collaborative testing was also required to ensure the validity of the analytically predicted heat-transfer, pressureloss, and flow-distribution characteristics.

One of the more important factors in determining the cooling requirements of the system is the establishment of the heat input to the water. Several sources of heat can be considered that are either generated in or transferred to the water:

- (1) Heat generated directly in the water by neutron and gamma radiation
- (2) Heat generated in the aluminum by gamma and beta radiation and transferred to the water
- (3) Heat transferred from the hot fuel assembly, through the aluminum pressure tube and into the water





(4) Heat generated in other areas (beryllium top and side reflectors and in the heat exchanger) and transferred to the water

Figure 74 is a schematic representation of a typical cell in the reactor and figure 75 shows the relative radial power distribution among the 121 fuel elements as calculated in reference 30. The heat generated in the water due to neutron heating varies as the power with a calculated average value of 100 watts per cubic centimeter of water.

Gamma and beta heat generation have a somewhat different distribution than the neutron heating and were calculated by using the ATHENA program (see ref. 30). The radial distribution of heat transferred to the water through the pressure tube by conduction and radiation from the hot fuel assembly is nearly constant. Figure 76 compares the distribution of the various sources of energy along with the combined distribution for all forms of heating. The average heating rates are given in table 12.

Superimposed on the radial variation in heating rates is the axial distribution shown in figure 77. It was assumed that the beta and gamma heat generation has this same axial distribution. The product of the local axial and radial factors multiplied by the average heating rate given in table 12 determines the specific heat generation at any given point in the reactor.

Figure 78 shows the heat transferred to the coolant from the hot propulsion gas by virtue of conduction through the aluminum pressure tube for each stage. Note that near the inlet of the reactor, heat is conducted from rather than into the water.

A small quantity of heat is also generated in the heat exchanger, side reflector, and top reflector. The total heat load on the water system from all sources is 50 917 Btu per second ( $5.36\times10^7$  J/sec). A breakdown of the individual heating values is shown in table 13, and the individual heat load from all sources for each cell within the core is given by figure 79.

#### COOLING REQUIREMENTS OF CORE

Based on the heating rates discussed in the preceding section, it is now possible to establish the cooling requirements of the individual cells. Table 14 is the average heat load for a cell in each of the hexagonal rings and the local value relative to the center element and the core average. The ratio of the heat load into the water outside the flow divider tube to that inside the flow divider is about 1.47 (fig. 79).

To establish the total water flow rate of the system, it is convenient to establish a factor F relating the overall flow requirement to that of the inside-the-divider flow of the center cell. For the purpose of this calculation, the center cell is assumed to have the same geometry as a propulsion type fuel assembly. For the nuclear reactor core, the factor is given by





 $F = 121 \times 0.74 \times 2.47$ 

F = 221

where the three multipliers are the number of cells, 121; the ratio of the power of the average cell to that of the center cell, 0.74; and the ratio of the total cell heat load to that inside the flow divider, 2.47. Therefore,

$$\dot{\mathbf{w}}_{\mathbf{core}} = 221\dot{\mathbf{w}}_{\mathbf{ic}}$$

An additional 13 percent flow is required for the beryllium side reflector in order to maintain the same coolant temperature rise in the reflector as in the core region. The total flow requirement relative to that inside the flow divider of the center element is then given by

$$\dot{\mathbf{W}}_{\mathbf{t}} = 1.13 \ \dot{\mathbf{W}}_{\mathbf{core}} = 250 \dot{\mathbf{W}}_{\mathbf{ic}}$$

From ideal minimum flow requirement considerations, therefore, the total flow rate should be 250 times the value necessary to cool the center (or hottest) pressure tube. Figure 80 shows the flow-rate - inlet-temperature combinations that will result in a maximum aluminum temperature of  $735^{\circ}$  R ( $408^{\circ}$  K). Because a small change in flow rate results in a large change in temperature at low flow rates, the flow rate for the center tube should be greater than about 3.5 pounds per second (1.59 kg/sec) to obtain the best operating point. At the same time, increasing the flow much beyond 4.5 pounds per second (2.04 kg/sec) results in relatively small increases in allowable inlet water temperature. It would appear, therefore, that the design total flow rate for the system lies between 875 and 1125 pounds per second (397 and 511 kg/sec) depending, of course, on the heat-exchanger analysis.

Figure 81 shows the radial effect of flow on the maximum surface temperature of the pressure tubes, if the core inlet reactor temperature is set at  $660^{\circ}$  R ( $367^{\circ}$  K). The ideal radial distribution of flow rate would be the intersection of the family of curves with the design temperature value ( $735^{\circ}$  R ( $408^{\circ}$  K)).

# **Necessity of Flow Divider**

As shown in figure 74, a flow divider separates each cell into the distinct water flow regions, one between the flow divider and pressure tube and the other external to the flow



divider. This divider was incorporated into the design to improve the cooling characteristics of the pressure tube without increasing the flow rate of the water excessively or lowering the inlet temperature to the point where freezing of the heat exchanger might occur. The flow divider also ensures a high velocity stream over the entire surface of the pressure tube, whereas local areas of low velocity might occur if the divider were not present.

The reduction in water flow rate that is possible with the flow divider concept to produce a high-velocity region for cooling and a low-velocity region for moderation can be approximated by using a method developed in reference 30 and the following equations:

Total temperature rise of fluid:

$$Q = \dot{W}c_p(T_b - T_{in})$$
 (1)

Local temperature difference between fluid and aluminum:

$$\varphi_{x} = h(T_{w} - T_{b})_{x}$$
 (2)

Heat-transfer coefficient:

$$Nu = \frac{hD}{K} = 0.023 \text{ Re}^{0.8} \text{ Pr}^{0.4}$$
 (3)

The local heat flux  $\varphi_{x}$  and total heat input into the coolant Q are the same with or without the flow divider. Since the fluid properties remain essentially constant for small temperature changes, equations (1) and (3) can be combined to yield

$$\frac{\dot{w}_2}{\dot{w}_1} = \frac{(T_b - T_{in})_1}{(T_b - T_{in})_2} \tag{4}$$

and

$$\frac{h_1}{h_2} = \left(\frac{G_1}{G_2}\right)^{0.8} \left(\frac{D_2}{D_1}\right)^{0.2} \tag{5}$$



# CONFIDENTIAL

where  $G = \dot{W}/A_f$ , and the subscripts 1 and 2 refer to the cases with and without the flow divider.

For the case with a flow divider, the flow is divided into two streams, one inside and one outside the flow divider. Thus,

$$\dot{\mathbf{W}}_{1} = \dot{\mathbf{W}}_{1} + \dot{\mathbf{W}}_{0} \tag{6}$$

and

$$Q = Q_i + Q_0 \tag{7}$$

The geometric relation of interest for the comparison of the effectiveness of the flow divider in the reference design are

$$\frac{D_1}{D_2} = \frac{0.2}{1.14} = 0.175$$

$$\frac{A_{f, 1}}{A_{f, 2}} = \frac{0.8164}{3.227} = 0.253$$

Equations (1), (2), and (5) to (7) can be combined keeping the maximum aluminum surface temperature at the same level with and without a flow divider to obtain

$$\frac{\dot{\mathbf{w}}_{2}}{\dot{\mathbf{w}}_{1}} = \left(\frac{1}{1+\gamma}\right) \left(\frac{\mathbf{A}_{f,2}}{\mathbf{A}_{f,1}}\right) \left(\frac{\mathbf{D}_{2}}{\mathbf{D}_{1}}\right)^{0.25} \left[\frac{\mathbf{T}_{w} - \mathbf{T}_{in}}{\mathbf{T}_{w} - \mathbf{T}_{b,2}} - \left(\frac{1+\gamma}{1+\beta}\right) \left(\frac{\mathbf{T}_{b,1} - \mathbf{T}_{in}}{\mathbf{T}_{w} - \mathbf{T}_{b,2}}\right)\right]^{1.25}$$
(8)

where

$$\beta = \frac{Q_0}{Q_i}$$

and

$$\gamma = \frac{\dot{\mathbf{w}}_{\mathbf{c}}}{\dot{\mathbf{w}}_{\mathbf{i}}}$$



This expression can be solved simultaneously with equation (4) to obtain the flow increase required with no flow divider.

In the reference design, the heat added to the water outside the flow divider  $Q_0$  is 1.47 times that added to the water inside the flow divider. If the temperature rise in the two streams is maintained equal, the ratio of  $\dot{W}_0$  to  $\dot{W}_1$  is also 1.47, that is,  $\beta = \gamma =$  1.47. Inserting these quantities and the previously given geometric relations for the reference design into equation (8) results in the following relation for a design surface temperature of  $735^0$  R ( $408^0$  K):

$$\frac{\dot{\mathbf{W}}_{2}}{\dot{\mathbf{W}}_{1}} = 2.23 \left( \frac{735 - \mathbf{T}_{b, 1}}{735 - \mathbf{T}_{b, 2}} \right); \left[ \frac{\dot{\mathbf{W}}_{2}}{\dot{\mathbf{W}}_{1}} = 2.23 \left( \frac{408 - \mathbf{T}_{b, 1}}{408 - \mathbf{T}_{b, 2}} \right) \right]$$

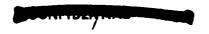
The results obtained where this expression is combined with equation (4) for an inlet temperature of  $660^{\circ}$  R ( $367^{\circ}$  K) indicate that the flow rate required without a flow divider is 1.22 times that required with the reference design.

Additional decreases in total flow rate can be achieved. If the flow rate in the inner passage is maintained at the required value and the outer flow rate is decreased, the same aluminum temperature can be maintained at lower total flow. The limit for this type of improvement is the increasing outlet temperature in the outer flow stream and in the temperature of the mixed streams at the outlet tube sheet. Eventually, the temperature of the tube sheet would exceed the allowable limit of  $760^{\circ}$  R ( $422^{\circ}$  K). As an example of these effects, if  $\gamma$  were reduced from 1. 47 to 1.12, the reduction in total flow would be accompanied by an increase in outlet temperature of the slower moving stream  $T_{\circ}$  from about  $710^{\circ}$  R ( $394^{\circ}$  K) to over  $740^{\circ}$  R ( $411^{\circ}$  K). For such a situation, the flow rate without a divider would be 1.4 times that required with the divider.

Another method for decreasing the overall flow rate without increasing the pressure tube temperature is to decrease the annular spacing between the flow divider and the pressure tube. By decreasing the hydraulic diameter of the flow passage, the flow rate can be reduced while the heat-transfer coefficient is maintained. Fabrication tolerances, orificing requirements, and pressure drops limit the extent to which the spacing could be reduced from its reference-design value of 0.100 inch (2.54 mm).

#### Water Flow Tests

The minimum water flow rate commensurate with maintaining adequate cooling of the structure will be obtained if the radial flow distribution can be made to match the flow at each ring corresponding to the  $735^{\circ}$  R ( $408^{\circ}$  K) tube temperature shown in figure 81.





Because of the complex nature of the flow paths within the reactor vessel, the calculation of pressure losses and orifice requirements necessary to obtain the proper distribution is somewhat uncertain.

A full-scale water flow test has been performed in which the system was studied to determine the pressure-loss and flow-distribution characteristics (see ref. 31). In this flow test, provision was made for readily changing the orifices at the entrances to the annular flow passages inside each of the flow dividers. Figure 5 shows the arrangement of these components in the reference design. It was also possible to vary the size of the holes in the outlet water baffle to modify the distribution of moderator flow outside the flow divider tubes. The water flow passages through the inlet end reflector were originally sized in an attempt to get close to the desired radial flow distribution and were not modified during the test.

The initial orificing was also based on the preliminary estimates of the pressure loss and ideal flow distribution of the system; subsequent orifice changes were made on a trial-and-error basis by using the results of the previous tests to estimate the requirements of the individual elements. Figure 82 shows the results of the last of eight successive tests in which the trial-and-error procedure was followed. Also shown is the ideal distribution replotted from figure 81 and the distribution with no orificing.

Although the radial flow pattern was markedly improved over the range of the eight test cases, it falls short of the desired distribution. For test 8, the ratio of water flow outside the flow divider tubes to inside the flow dividers was 1.11 instead of 1.47. It may be that some of the limitations encountered in the flow test mockup such as a fixed-flow passage configuration through the inlet end reflector and significant leakage past the orifices at the inlet to the flow inside the dividers prevent a ready attainment of the desired distribution. It may also be that inherent aspects of the design cause this difficulty. Included among these is the uninhibited radial crossflow in the low velocity region between the inlet end and outlet end baffles.

In any case, if it is assumed that test 8 represents an achievable distribution in the reference design, a total flow significantly higher than the ideal flow will be required. In addition, the temperature of the water at the exit of the passages inside the flow dividers is lower than that of the water flowing outside the flow divider. The percentage of flow through the side reflector region for test 8 was lower than that required based on the heat loads presented in table 13. The total flow in test 8 was adjusted so that the flow in each ring was equal to or greater than the ideal flow thus ensuring that the  $735^{\circ}$  R  $(408^{\circ}$  K) aluminum surface temperature would not be exceeded.

A comparison of the ideal flows and those resulting from test 8 is shown in the following table:



Radial flow	Ratio of outside			required		
distribution	to inside flow	percent of total	lb/sec	kg/sec	ideal	
Ideal	1, 47	13	937.5	424	100	
Test 8	1, 11	6.3	1040	472	111	

Thus, the total flow is 11 percent higher than the ideal; the average temperature of the water as it leaves the flow regions outside the divider is  $717^{\circ}$  R (398° K) compared with  $700^{\circ}$  R (389° K) for the regions inside the flow divider. The variation of beryllium reflector temperature with water flow through the reflector is shown in figure 83. The  $810^{\circ}$  R (450° K) beryllium temperature resulting from the 66 pounds per second (30 kg/sec) flow in test 8 should present no problem.

The predicted pressure losses for the prescribed flow distribution in the test vessel are given in figure 84. These values are based on a flow rate of 1040 pounds per second (472 kg/sec) and were computed by using the analytical methods outlined in reference 32. A comparison of the predicted and experimental pressure losses throughout the system is given in table 15.

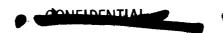
The experimental results fall close to the predicted values. The one exception appears to be in the orifice pressure loss where trial-and-error procedures were used in an attempt to obtain the desired distribution. However, this discrepancy can be attributed to several possible causes:

- (1) The orifice design in the test facility was poor.
- For ease of assembly, the orifice was designed as an annulus which could easily be assembled and disassembled over the pressure tube. Leakage between the tube and orifice became a large factor, particularly for the smaller orifice. Note that when the nominal leakage was considered (table 15), the results were in close agreement.
- (2) The radial flow distribution in the test was fairly uniform, while the predicted values of pressure were based on the ideal flow distribution.

Possibly, much better agreement could be obtained if the orifice were designed to prevent leakage. Future tests could be limited merely to testing one element with its associated orifice rather than conducting a full-scale test.

Based on the results of the full-scale water flow test, the probable pressure loss and flow distribution can be determined for the reference design. The procedures outlined in reference 30 were used to determine the pressure losses from the following equation:

$$\Delta P = C \frac{\left(\frac{\dot{w}}{A_f}\right)^2}{2g\rho}$$





The values of the constant C for various configurations are tabulated in the reference. The flow distribution is that from the last of the test runs and the geometry is that of the reference design.

Pressure recovery due to changes in velocity are evaluated from

$$\Delta P_r = \frac{\rho}{2g} \left( v_2^2 - v_1^2 \right)$$

Figure 85 shows the predicted pressure loss and prescribed flow distribution in the reference design. The overall pressure loss for the system is 153 psi  $(105 \text{ N/cm}^2)$ . The reason that this value is higher than the total loss in the test  $(84 \text{ psi } (58 \text{ N/cm}^2))$  is that, outside the reactor core section, the reference system was not simulated exactly; for example, the heat-exchanger loss was only 29 psi  $(20 \text{ N/cm}^2)$  in the model, whereas it is  $66 \text{ psi } (45.5 \text{ N/cm}^2)$  in the reference design. Other differences are in the diameter and length of the piping and in the regions between the pressure vessel and the side reflector.

### Use of Roughened Surface to Improve Heat Transfer

In an effort to decrease the coolant flow rate without adversely affecting the performance of the core or the heat exchanger, several concepts for improving the cooling ability of the fluid were studied. One of these innovations, which appears promising, is the use of a roughened surface to improve the heat-transfer characteristics. A rough surface tends to increase the turbulence of the fluid, breaking up the laminar sublayer and increasing the film coefficient.

Of the several methods employed by various experimenters to roughen surfaces, the most promising from the point of uniformity and reproducibility appears to be the use of a knurled surface (ref. 33). Obviously, the knurling will result in higher friction factors so that an increase in the pressure loss across the knurled surface occurs.

Some differences of opinion have been expressed by various experimenters (ref. 33) as to the efficiency of roughened surfaces with regard to the gains derived at a constant pumping power, that is, whether or not a gain in heat transfer can be achieved at the same pumping power. While some conflicting data on this subject have been reported, ''only gains have been reported where the flow is through an annulus in which the wall transferring heat is roughened and the other wall is smooth'' (ref. 33).

Since the quoted configuration would be present if the pressure tube were knurled and a smooth flow divider were used, the application of this concept to the reactor design seems feasible. In addition, the frictional loss across the pressure tube represents only a small portion of the total loss in the system, so that a small reduction in total flow



could more than compensate for a two- or threefold increase in the frictional resistance across the core.

Experiments conducted with water flowing in an annular channel showed that a marked improvement in the heat-transfer coefficient results as the depth of the knurling  $\epsilon$  is increased. Those results indicate the heat-transfer and pressure-drop behavior shown in figure 86.

Any increase in heat-transfer coefficient can be utilized to advantage in two ways:

- (1) At a constant flow, the allowable level of water operating temperature can be increased to achieve a higher margin from freezing in the heat exchanger without increasing core pressure tube temperature.
- (2) At a constant level of water operating temperature, the flow rate can be decreased with no increase in metal temperature.

The extent of the first of these possible advantages can be seen in figure 87 which shows the allowable increase in core inlet temperature of the water for various ratios of increasing heat-transfer coefficient. At a flow rate of 4 pounds per second (1.82 kg/sec), the near optimum knurling roughness (see fig. 88) results in a heat transfer improvement ratio of 1.75 and an increase of 15° in allowable water inlet temperature.

The information given in figures 86 and 87 can be used to determine the relative pumping power increase across the core with either a constant flow rate ( $\dot{W}_r/\dot{W}_s=1.0$ ), or a constant inlet temperature ( $\dot{W}_r/\dot{W}_s<1.0$ ). For this calculation, the approximations were made that the pumping power  $\theta$  was proportional to the flow rate times the pressure loss, and that the pressure loss was proportional to the friction factor times the flow rate squared. These relations can then be expressed as a ratio of the required pumping power with a rough surface to that required if no knurling were used:

$$\frac{\theta_r}{\theta_s} = \frac{f_r}{f_s} \left( \frac{\dot{w}_r}{\dot{w}_s} \right)^3$$

Figures 88 and 89 show the results of this study when the parameters involved are varied over the range of interest. It can be readily seen that by doubling the pumping power across the core, the allowable operating temperature can be increased 10 to 30  $\rm R^0$  (5.55 to 16.7  $\rm K^0$ ) at a constant flow rate, or the flow rate can be reduced 10 percent or more at a constant operating temperature. It is again emphasized that, since the pressure loss across the core represents less than 5 percent of the total loss in the loop, this factor of 2 does not have a significant affect on the overall system. In fact, if the flow rate is reduced, the total pumping power requirements will actually decrease since a 10-percent reduction in flow results in about a 30-percent reduction in the power re-



quired in the remainder of the loop, thus far offsetting the relatively high increase in the localized core region.

From the brief analysis presented, knurling the outer pressure tube surface offers an attractive possibility for improving the performance of the water system.

#### SIZING OF HEAT EXCHANGER

Within the temperature and flow limits necessary to establish the proper cooling of the structure in the nuclear reactor, various combinations of parameters will also yield an acceptable heat-exchanger design (i.e., one in which freezing does not occur under any steady-state conditions). Figure 90 shows the characteristic behavior of a water-to-cold-gaseous-hydrogen heat exchanger constructed of aluminum, with hydrogen flow inside the tubes, as certain geometry and flow parameters are varied. In each case, the nonvarying parameters are maintained at values in the known or reasonable operating range, for example, flow rates, fluid temperatures, and heat load in figures 90(a) and (b); tube size and spacing in figure 90(d).

Based on these considerations, a heat exchanger was chosen which provides a reasonable margin from freezing without an excessive pressure drop on either the water or hydrogen side. The important dimensions and temperatures of the heat exchanger are listed in table 16. In the reference design, the heat exchanger is subdivided into six sections equally spaced around the reactor core. This heat-exchanger location shortens the hydrogen and water flow paths and provides more uniform flow patterns in the region of the core. Each section contains 120 tubes. The use of parallel flow, rather than counter flow, increases the length of the heat exchanger by 2 or 3 inches (5 or 7.6 cm) but provides an additional 30 to 40 R<sup>O</sup> (16.7 to 22.2 K<sup>O</sup>) margin from freezing. Efficiency is not an important factor provided that the length of the heat exchanger is compatible with the overall core length. The length of the heat exchanger in the reference design is 2.75 feet (83.8 cm).

The performance of the heat exchanger for various heat loads is shown in figure 91. At the design-point heat load of  $50.9\times10^3$  Btu per second  $(5.37\times10^7 \text{ J/sec})$ , a  $65 \text{ R}^0$  (36  $\text{K}^0$ ) margin from freezing exists, and core aluminum temperatures do not exceed  $735^0$  R ( $408^0$  K). At lower heat loads, the margin from freezing is reduced, and freezing will occur at 83 percent of the design value. At higher heat loads, core aluminum temperatures will increase. At 5 percent above the design heat load, the assumed limiting value of  $760^0$  R ( $422^0$  K) is reached in the aluminum. This off-design capability could be made equal for loads above and below design load by a slight change in the reference design, for example, by increasing the length (see fig. 90(c)).



### Off-Design and Transient Behavior of Heat Exchanger

Calculations of heat-exchanger performance were made over a wide range of flow rates and inlet temperatures. Included in these calculations were many situations in which predicted wall temperatures were below the freezing temperature of water, and icing of the tube walls could be expected to occur.

Figure 92 shows the results of explicit calculations (shown in the figure as symbols) performed by using a digital tube-and-shell heat-exchanger computer program in which freezing and the subsequent buildup of ice on the tube walls is accounted for. It can be seen from these results that, as hydrogen flow is increased for a given set of conditions, the calculated overall heat-transfer coefficient U increases until ice begins to form (indicated by solid symbols) and remains fairly constant at about this critical value  $U_{crit}$  as additional ice is formed.

This behavior has certain implications with regard to the performance of the system during transients. If during a transient, the ratio of hydrogen flow to water flow were high enough to cause some ice to form, the situation would not present a problem unless the ice blockage would be so great that the increase in heat-exchanger pressure drop would lower the water flow rate sufficiently to cause overheating of the core structure. In the reference-design parallel-flow heat exchanger, ice will begin to appear locally at the exit end as icing conditions are encountered. As icing conditions become more severe, the ice at the exit end becomes thicker and icing spreads axially upstream. For small thicknesses of ice at the exit end, the length of exchanger in which ice appears is a small part of the heat-exchanger length. The resulting change in overall water system pressure drop is also small. Therefore, a significant decrease in water flow rate would probably not occur until a heavy ice layer had built up at the exit end.

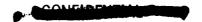
To facilitate calculations of off-design performance of the heat exchanger, the explicit calculations (fig. 92) were curve fitted with an empirical equation of the form

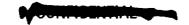
$$U = A(\dot{w}_{H_2})^B; \left[ U = A(2.205 \,\dot{w}_{H_2})^B \right]$$
 (9)

for operation free of ice  $U < U_{\mbox{crit}}$ . After ice begins to form, the overall heat-transfer coefficient remains essentially constant. The critical value at which ice begins to form is computed from the empirical equation

$$U_{crit} = 48(J - N); \left[U_{crit} = 9.808 \times 10^{5} (J - N)\right]$$
 (10)

In these equations, the following values are used:





$$A = 0.0135 E^2 - 0.013 E - 0.0838 + 0.947 M - 1.522 M^2;$$

$$\left[A = (1.341 \text{ E}^2 - 0.585 \text{ E} - 1.712 + 19.351 \text{ M} - 31.10 \text{ M}^2)10^3\right]$$

$$B = 0.8919 - 3.572 M + 5.878 M^2 + 0.4686 E - 0.2888 E^2;$$

$$\left[ B = 0.8919 - 3.572 \text{ M} + 5.878 \text{ M}^2 + 1.033 \text{ E} - 1.404 \text{ E}^2 \right]$$

$$N = 0.0545 - 0.4859 M + 1.689 M^2$$
;  $N = 0.0545 - 0.4859 M + 1.689 M^2$ 

$$J = \frac{\dot{W}_{H_2}}{\dot{W}_{H_2O}}$$

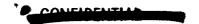
$$E = \frac{\dot{W}_{H_2O}}{1000}$$

$$M = \frac{T_{\text{in, H}_2O} - 492^{\circ} R}{T_{\text{in, H}_2O} - T_{\text{in, H}_2}}; \left[ M = \frac{T_{\text{in, H}_2O} - 273^{\circ} K}{T_{\text{in, H}_2O} - T_{\text{in, H}_2}} \right]$$

An additional aspect of the tendency and effects of ice formation in the system has to do with the time required to form ice after the heat-exchanger walls have reached the freezing point. A recent analysis (ref. 34) describes the transient behavior of the ice layer buildup in terms of the steady-state thickness  $\mathbf{X}_{\mathbf{S}}$  and the dimensionless parameters listed as follows:

Dimensionless time:

$$\tau' = \frac{h_l(T_l - T_f)\tau}{\rho LX_s}$$



Subcooling parameter:

$$S = \frac{c_p(T_f - T_c)}{L}$$

Thermal resistance parameter:

$$R = \frac{\frac{X_s}{K}}{\frac{1}{h_c} + \frac{a}{K_w}}$$

where K is the conductivity of solidified liquid. Figure 93 shows the interrelation of these parameters; in particular, the time necessary to reach 98 percent of the steady-state ice thickness is shown as a function of the subcooling parameter and the thermal resistance parameter.

By utilizing these dimensionless parameters (ref. 32) in conjunction with the curve fit equation describing the characteristic behavior of the heat exchanger, it is possible to perform a pseudo-transient analysis of the startup of the reactor to determine the severity of a transient in terms of ice blockage. Figure 94 shows the generalized variation of the flow rates and inlet temperatures in the heat exchanger during a typical startup transient. The exact behavior during startup and the value of the delay times W, X, and Y as well as the total transient time Z are dependent on the results obtained from control studies. Several possible combinations of these variables and the results of the pseudo-transient analysis for the combinations are given in table 17. In addition to listing the time to onset and end of icing, the table also gives a measure  $\,U/U_{\hbox{crit}}\,$  of the maximum penetration into the icing regime and the time at which it occurs. The ratio between the actual overall heat-transfer coefficient and that at which freezing would start at the same bulk fluid temperature is designated as  $\,U/U_{\hbox{crit}}.\,\,$  The higher the ratio is, the greater is the ice thickness. The amount of ice formed at steady-state conditions corresponding to those at the maximum values of  $\,U/U_{\hbox{\scriptsize crit}}\,$  shown in the table were calculated and are also listed.

The results obtained for case 1 (shown in table 17) are also given in figure 95 and can be used to illustrate the applicability of results from this analytical technique. Possible ice formation can occur during the period from 5.0 to 20.5 seconds, 15.5 seconds during the 30-second transient. The variation in the dimensionless parameters of reference 32 are also shown in figure 95. During the potential icing period, the subcooling parameter varies from 12. ( to 10.5, while the thermal resistance parameter increases during the same period from 2.8 to 8.0. In the same interval, the ratio of the real time



to the dimensionless time varies from 0.28 to 0.12.

The preceding information is used to calculate the time necessary to form 98 percent of the steady-state ice thickness (fig. 93) which varies from 0.54 to 1.68 seconds during the icing period. This formation time is, in essence, a delay time from the beginning of an icing condition to the time at which 98 percent of the steady-state thickness has formed. Since this average 1-second delay time (0.54 to 1.68 sec) is short relative to the total time that an icing condition exists (15.5 sec), the time involved in transient ice formation is insignificant in determining the thickness of the ice which would form during this startup. Therefore, the results of a series of steady-state calculations for ice thickness, including those listed in table 17 for maximum thickness, should be fairly accurate.

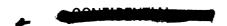
Figure 96 shows the results of such a steady-state analysis of the heat exchanger using the conditions existing during the icing period of case 1. The maximum ice thickness is about 0.013 inch (0.330 mm), considerably short of the 0.05 inch (1.27 mm) necessary to cause blockage of the water flow. For this particular startup transient, ice blockage does not appear to be a problem.

An examination of the maximum calculated thicknesses and the total times in the icing condition (table 17) can lead to certain conclusions regarding those factors in the startup transient which are of greatest importance in avoiding problems. As would be expected, the shorter the startup time Z, the less time will be spent in icing conditions and the less likely is overheating of the core components due to blockage. Table 17 also indicates that a short delay time Y before increasing the water flow will keep ice formation down to low values. It is, therefore, desirable to bring the water pump up to speed as quickly as possible.

The exact extent of the icing problem during the startup transient will depend on the limitations on the design of an engine control system. Studies of engine startup transients (ref. 4) indicate a need for a modification of the reference design in order to completely avoid ice formation in the heat exchanger and/or overheating of the aluminum pressure tubes during startup. If these conditions must be avoided, a 20-percent increase in water flow rate may be required.

#### HEAT EXCHANGER EXPERIMENTS

A 19-tube version of the reference-design heat exchanger was fabricated (see the section on FABRICATION OF HEAT EXCHANGER, p. 22) and tested in a facility which permitted operation over a wide range of both steady-state and transient conditions. The purpose of these tests was to demonstrate satisfactory operation, to establish the limits of ice free operation, and to assess the accuracy of calculational techniques for predicting performance. The first series of tests was conducted at steady state in which param-



eters such as hydrogen inlet temperature, water inlet temperature, and ratio of hydrogen to water weight flows were varied. These tests were followed by transient tests in which the effects of various startup parameters were investigated.

# Steady-State Tests

The heat balance for these experimental runs is generally accurate within 10 percent. There is some question as to the exact ortho-para composition of the gaseous hydrogen even though it was obtained from para-liquid prior to the tests. Since gaseous hydrogen was mixed with liquid hydrogen in most of the runs, the exact ortho-para composition of the mixture flowing through the heat exchanger is also questionable. The heat absorbed by the hydrogen  $Q_{H_2}$  in the experiments was calculated using normal (75 percent ortho, 25 percent para) gaseous hydrogen and para-liquid hydrogen with their respective flow rates. Figure 97 is a plot of these values of  $Q_{H_2}$  as a function of the heat released by the the water  $Q_{H_2}$ 0.

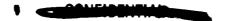
A comparison of the experimental overall heat-transfer coefficients with their corresponding calculated values is shown in figure 98. The solid symbols represent conditions where ice is predicted. The open symbols represent no ice. The agreement between calculated and experimental values with no ice is generally better than 10 percent, while the ice, measured values are generally between 10 and 20 percent greater than the calculated values.

When ice is present, the calculation of the overall heat-transfer coefficient becomes more complicated. It is affected by the thermal conductivity of the ice, the temperature of the surface of the ice on the water side, and the relation between ice thickness and water flow uniformity. The assumption of a 492° R (273° K) water-ice interface temperature appears to be valid, as shown in reference 34. The effect of the remaining parameters can only be speculative without measurements of the individual heat-transfer coefficients.

Figure 99 is a plot of the total measured hydrogen pressure drop as a function of the predicted pressure drop. The best agreement between predicted and measured values occurs without icing. The total pressure drop is made up of the friction pressure drop and the pressure drop due to change in momentum. When the pressure drop due to the change in momentum is a large part of the overall pressure drop, the accuracy with which the heat-transfer coefficient can be predicted affects the accuracy of the prediction of the total pressure drop.

Isothermal water pressure drops, both measured and predicted, are shown in figure 100. Here the total pressure drop for a straight section, consisting of the center





2 feet (61 cm) of the heat exchanger is plotted as a function of the water flow rate. In the interest of simplicity, the calculation of the pressure drop due to the spacers was done separately. Figure 100 shows the predicted pressure drop across the heat exchanger without and with spacers. It can also be seen that the total predicted pressure drop is less than the measured pressure drop by approximately 40 percent. It is reasonable to expect that this will also be the case for pressure drop comparisons when heat transfer is present.

Figure 1°1 is a plot of the measured water pressure drop as a function of the total predicted pressure drop with heat transfer. Here, for conditions where ice is not predicted (open symbols) the measured pressure drop is greater than the predicted by the same magnitude as in the isothermal condition. When ice is predicted, the measured values are also higher than the predicted values.

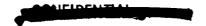
When ice is present on the tubes of the heat exchanger, the cross-sectional flow area is decreased by the amount of the cross-sectional area of the ice. With constant water flow rate, the pressure drop with ice present will be higher than without ice. Therefore, if the agreement between predicted and measured pressure drop is better with ice than without, it would seem to indicate that the ice layer is not as thick as predicted.

The results of this investigation of a shell and tube heat exchanger operating at steady-state conditions with cryogenic hydrogen flowing through the tubes and water through the shell can be summarized as follows:

- (1) Over the range of conditions investigated, the heat exchanger will operate in a stable manner even in the range where ice is predicted. These conditions involved departures from normal reference design operation as severe as reducing hydrogen inlet temperature by 80  $R^{O}$  (44.4  $K^{O}$ ), water inlet temperature by 60  $R^{O}$  (33.3  $K^{O}$ ), and increasing hydrogen- to water-flow-weight ratio by a factor of 4.
- (2) At conditions where no ice is predicted, (a) agreement between predicted and measured overall heat-transfer coefficient and hydrogen pressure drop was good and (b) measured water pressure drop for both isothermal and heat-transfer runs was considerably higher than the predicted values.
- (3) At conditions where ice is predicted, the measured overall heat-transfer coefficient and hydrogen pressure drop were higher than predicted values.
- (4) It appears that the actual ice layer was thinner than predicted because the ratio of measured to predicted values of overall heat-transfer coefficient and hydrogen pressure drop was higher for predicted ice conditions than for no icing.

## **Transient Tests**

During startup of the rocket reactor, the hydrogen and water flow rates, inlet tem-



perature, and inlet pressure will change with respect to time. Simulated startup transients were run by using the test heat exchanger to check startup behavior and the accuracy of techniques for predicting this behavior.

To simulate these conditions, the six parameters, hydrogen and water inlet temperatures, inlet pressures, and flow rates, were programmed, or ramped, in such a way as they might occur during startup. One such ramp is shown in figure 102 where the inlet temperature and flow rates of the water and hydrogen are shown as a function of time.

The inlet pressures vary linearly with time between the values shown and the resulting parameter values at the beginning (time zero) and end (time = 30 sec) of the ramp are given. This ramp represents an increase from 17 percent to full power in 30 seconds. Each data point represents the average of 25 readings taken over a period of 0.64 second.

Prior to the start of the ramp, an attempt is made to obtain steady-state conditions at the values of the parameters at time equal zero. Steady-state conditions are never quite realized as it is difficult to maintain constant flow rates and, consequently, constant inlet temperatures at these low flows.

Measured transient overall heat-transfer coefficients obtained from the ramp shown in figure 102 are shown in figure 103 plotted as a function of the percentage of total ramp time. Included for comparison are two ramps similar to that shown in figure 102 but having one-half and one-fourth the ramp rates. Examination of the figure shows no detectable effect of ramp rate on the transient overall heat-transfer coefficient. Values below 16 percent of total ramp time are not included as the hydrogen pressure and/or temperature were near their critical value resulting in uncertainty in the value of the inlet enthalpy.

Also shown for comparison is the measured steady-state heat-transfer coefficient at 100 percent of ramp time. Comparing this value with the value of the transient heat-transfer coefficient at 100 percent ramp time indicates that the steady-state and transient values are the same for this point in the ramp.

Figure 104 is a plot of the transient overall heat transfer for a 30-second ramp similar to the one described in figure 102 but with an inlet water temperature 40 R<sup>O</sup> (22.2 K<sup>O</sup>) lower. Here the heat-transfer coefficient is also plotted as a function of total ramp time. Three measured steady-state heat-transfer coefficients at conditions similar to those existing at that instant in the ramp are included for comparison: one at 26 percent of total ramp time, one at 60 percent, and one at 100 percent. There is good agreement between steady-state and transient values at times equal to 26 and 100 percent of ramp time, while at 60 percent the transient value is 12 percent below the steady-state value. This disagreement may be a result of a lower value of hydrogen inlet temperature at this time in the transient run than the closest corresponding steady-state run available. It appears from this curve that the transient overall heat-transfer coefficient can be reasonably well predicted from a corresponding measured steady-state value.



# CONFIDENTIAL

Calculations for this run indicate the presence of ice for about the first 18 seconds (60 percent) of the total ramp time. No blockage or other adverse effects were observed.

From these transient tests it appears that a steady-state map of heat-exchanger operation is sufficient to predict its transient behavior. This is true even for transients in which ice formation and melting occur. Ramp time seems to have no effect on the response to given changes in operating parameters in going from low to full power.

#### WATER MODERATOR SYSTEM CHEMISTRY

Two processes in the water moderator system were investigated as possible sources of operational problems. Extensive corrosion could result in a decrease of structural integrity. Even moderate corrosion could result in the formation of quantities of gaseous hydrogen exceeding the solubility limits of the water. Radiolysis of the water also generates gases which must be taken into account.

Accumulation of undissolved gas in the moderator system could cause any of the following undesirable situations:

- (1) Water pump cavitation and flow reduction
- (2) Overpressurization of the system
- (3) Power perturbations due to formation and collapse of voids in the moderator In order to determine the extent of these problems associated with corrosion or radiolysis, analytical and experimental programs were carried out and are reported in references 24, 25, and 35.

### Effect of Corrosion on Structural Integrity

The water moderator is in contact with the pressure vessel components and with the circulating system components. The great bulk of this material in the reference design is 6061 aluminum. The remainder is the stainless steel in the pump, the zirconium in the poison control tubes, and the beryllium reflectors in the core. Interaction between the deionized water and the materials can result in weakening of the structure due to reduction of thickness.

Preliminary investigations of potential problem areas (see ref. 24) indicated that the total corrosion penetration into aluminum will be less than 0.3 mil (0.00762 mm) in a system from which more ''noble'' materials are excluded. Examples of these more noble elements are graphite, copper, mercury, silver, gold, lead, and tin. Even minute quantities of these materials could cause severe localized pitting of aluminum and subsequent reduction in strength. The amount of attack in a clean system represents only



1 percent of the very thinnest aluminum present in the loop, the 0.035-inch-thick (0.889 mm) heat-exchanger tubes. Since the design stress is only 0.8 of the yield point, no structural problems should result from even this amount of corrosion.

#### Extent of Gas Generation

Estimates of the amount of gas generated as a result of water decomposition were made by others (refs. 24 and 25). Experiments were also conducted to determine the extent of hydrogen generation from aluminum corrosion, as reported in reference 35.

The decomposition studies indicate that the amount of hydrogen and oxygen generated due to water radiolysis depends on water pH, initial hydrogen content, and, to a small extent, temperature. The equivalent mole fraction of hydrogen (hydrogen plus oxygen) estimated for  $655^{\circ}$  R ( $364^{\circ}$  K) water having no initial hydrogen and unadjusted pH and an energy deposition of 150 watts per cubic centimeter is  $3.2\times10^{-5}$ . The hydrogen content could be reduced by a factor of about 3 if the pH is reduced to 3.0. Operating with a pH between 5.0 and 7.0, however, seems to have little effect on radiolytic gas content.

The corrosion experiments duplicated as closely as possible the range of water temperatures, pH, velocities, and heat fluxes expected in the TWMR. The range of variables investigated is summarized in table 18. The amount of hydrogen generated was determined by several methods including direct measurement of hydrogen, measuring metal specimen weight changes, and by chemically stripping and measuring the amount of aluminum oxide produced on specimens. As a result of the experiments, empirical correlations were formulated to predict hydrogen generation per unit area of aluminum surface exposed to test conditions. These correlations were used together with known aluminum surface areas and moderator volumes in the TWMR to predict the following hydrogen content of the moderator over the flight life of the TWMR:

Condition	Water temper- ature		Time of exposure,	Aluminum heat:		Hydrogen content, mole		
			hr	Btu/(sec)(ft <sup>2</sup> )	$J/(sec)(m^2)$			
	<sup>o</sup> R	o <sub>K</sub>				fraction		
100 Percent design	760	422	1	60	6.8 ×10 <sup>5</sup>	0.14×10 <sup>-4</sup>		
Initial shutdown	760	422	336	13	1. 48×10 <sup>5</sup>	1.3		
Extended shutdown <sup>a</sup>	660	367	17 500	0	0	1.5		
Total corrosion product (hydrogen)								

<sup>&</sup>lt;sup>a</sup>The extended shutdown data are based on extrapolation of experimental data obtained for a maximum exposure of 1400 hr.



# CONFIDENTIAL

The total mole fraction of hydrogen generated in the moderator system including the corrosion product hydrogen and radiolytic gas is about  $3.2\times10^{-4}$ . The pressure required to keep various concentrations of hydrogen dissolved in water at various temperatures is shown in figure 105. The pressures are essentially the sum of the hydrogen partial pressure and the water vapor partial pressure for our situation in which the amount of oxygen generated is low. From figure 105 it can be seen that a total system pressure of about 350 psia (241 N/cm<sup>2</sup> abs) is required to keep this gas in solution. This gas concentration is less than the  $5\times10^{-4}$  mole fraction permissible with the 600 psi (414 N/cm<sup>2</sup>) normal operating pressure. Therefore, all the gas can be held in solution during normal operation.

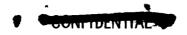
During the initial and extended shutdown period, the water system pressure must be reduced in order to keep the stresses in certain components such as the outlet tube sheet and pressure tubes to reasonable values. The reference design is capable of a 100 psia  $(69 \text{ N/cm}^2 \text{ abs})$  water system pressure during these shutdown periods. As can be seen from figure 105, hydrogen concentration is limited to only  $0.9\times10^{-4}$  mole fraction with this pressure and  $660^{\circ}$  R  $(367^{\circ}$  K) water temperature. Therefore, hydrogen can be expected to come out of solution.

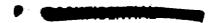
### Effects of Gas Accumulation

Although it is known that pump performance characteristics are affected by the presence of undissolved gases, no quantitative description of these effects is known. Before such gas could be accepted as tolerable, experiments would have to be conducted to evaluate the magnitude of any resulting flow reduction and what the consequences of this reduced flow are for heat transfer.

If adequate provision were not made for the volume changes resulting from gas leaving the solution, the system pressure would exceed the design value of 100 psi (69 N/cm $^2$ ) and rupture of structural components could occur. The reference design incorporates a pressurizer tank with 5.0 cubic feet (0.142 m $^3$ ) of gas accumulation capacity. The flat portion of the curve in figure 106 represents gas generation up to saturation and a full (5 ft $^3$  (0.142 m $^3$ )) displacement of the pressurized tank bladder. It can be seen that the total 3.2×10 $^{-4}$  mole fraction of hydrogen can be accommodated in the system without overpressurization. If the actual gas production exceeded 5×10 $^{-4}$  mole fraction, the system pressure would start to rise, as indicated (see fig. 106), and rupture might occur.

The third possible problem arising from undissolved gas in the moderator is associated with reactor reactivity effects. Power perturbations will result from formation and collapse of gas pockets in the water. It has been pointed out that the estimated gas





production does not exceed the solubility limits at the operating pressure of 600 psi  $(414 \text{ N/cm}^2)$  so that no problems of this nature are to be expected under these circumstances. At a pressure of 100 psi (69/cm<sup>2</sup>) presently required for shutdown conditions, gas will come out of solution and increase fluid volume into the pressurizer bladder region. It is not certain where the excess gas would collect under a zero-gravity coast condition. At restart, therefore, the distribution of the gas in the water system cannot be defined in the present reference system. The startup sequence has already been outlined (see section ENGINE CONTROL, p. 11) and involves circulation of the moderator and poison-control solution while the reactor is being brought up to some low power during which time the fuel and moderator temperatures are raised. The maximum moderator loop pressure during this period is 100 psi (69  $\mathrm{N/cm}^2$ ), and flow induced variation of gas pockets in the core will cause perturbations in the power level. Since the power level is low and the water velocities are also low, these perturbations should not cause any problems with overheating but they may exercise the poison control system to an undesirable degree. When hydrogen flow has reached the level where nozzle chamber pressure is approximately 100 psi (69 N/cm<sup>2</sup>), the water system pressurizer will start following nozzle chamber pressure in its approach to full operating conditions.

The presence of gas in the water moderator during this pressurization and approach to power phase of restart could result in an accident. It can be postulated that for some reason all the gas in the moderator system is gradually deposited in the core region during the warmup period and that the poison-control system has gradually compensated for this accumulation by removing cadmium from the solution. During the power increase, the pressurization of the water system will drive this gas back into solution and increase core reactivity. The change in reactivity associated with this redissolution of the gas in the system is \$4.30. The planned startup procedure calls for an increase in pressure from 100 to 350 psi (69 to 241 N/cm²) in about 10 seconds. Although studies have not been performed on this rate (43 ¢/sec) of reactivity insertion during the approach to power, it does appear to be significant enough to require further investigation.

If the elimination of gas from the system should become necessary because of this reactivity problem or because of the previously mentioned pump cavitation or heat-transfer problems associated with undissolved gas in the water, at least two techniques could be used.

In the first of these methods, the amount of gas produced by corrosion might be reduced. The corrosion tests (ref. 35) included various degrees of preoxidation of the aluminum surfaces. The values used in predicting gas generation were based on the best pretreatment obtained, but there is evidence indicating that a heavier preoxide would reduce corrosion. An investigation aimed at optimizing preoxidation to reduce corrosion without causing spalling may result in a treatment which would reduce the gas generated to a tolerable level.

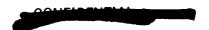




The other method for dealing with the problems of gas is to install a gas removal device in the water moderator system. Such a device would probably be installed at the inlet of the auxiliary water pump to separate the water from the gas. It might be something as simple as a high-velocity elbow. Once the gas is separated at a specific location, its elimination from the system could be easily arranged using the vacuum of the space environment.

#### SYMBOLS

```
flow area, ft<sup>2</sup>; m<sup>2</sup>
         tube thickness, ft; m
a
         specific heat-constant pressure, Btu/(lb)(OR); J/(kg)(OK)
^{c}_{p}
D
         diameter (equivalent hydraulic diam), ft; m
d
         tube diameter, in.; cm
\mathbf{F}
         dimensionless flow ratio
f
         friction factor
         mass velocity, lb/(sec)(ft<sup>2</sup>); kg/(sec)(m<sup>2</sup>)
G
         gravitational constant, ft/sec<sup>2</sup>; m/sec<sup>2</sup>
g
         pump head, ft of water: m of water
Η
         film coefficient, Btu/(sec)(ft<sup>2</sup>)(OR); J/(sec)(m<sup>2</sup>)(OK)
h
         thermal conductivity, Btu/(sec)(ft)(OR); J/(sec)(m)(OK)
K
\mathbf{L}
         heat of fusion, Btu/lb; J/kg
         Nusselt number, hD/k
Nu
         pressure loss, psi; N/cm^2
\Delta P
         pressure recovery, psi; N/cm<sup>2</sup>
\Delta P_r
         Prandtl number, c_n \mu/K
\mathbf{Pr}
         heat-transfer rate, Btu/sec; J/sec
Q
R
        thermal resistance parameter
Re
        Reynolds number, GD/\mu
S
        subcooling parameter
\mathbf{s}
        tube spacing, in.; cm
```



- T temperature, <sup>o</sup>R; <sup>o</sup>K
- U overall heat-transfer coefficient, Btu/(sec)(ft<sup>2</sup>)(OR); J/sec)(m<sup>2</sup>)(OK)
- v velocity, ft/sec; m/sec
- W delay time, sec
- w flow rate, lb/sec; kg/sec
- X delay time, sec
- $X_{S}$  steady-state ice thickness, ft; m
- Y delay time, sec
- Z startup time, sec
- $\epsilon$  knurling depth, ft; m
- $\theta$  pumping power, hp; W
- $\mu$  viscosity, lb/(sec)(ft); N/(sec)(m)
- $\rho$  density, lb/ft<sup>3</sup>; kg/m<sup>3</sup>
- au time to form steady-state ice layer, sec
- $\tau$ ' dimensionless time
- $\varphi$  heat flux, Btu/(sec)(ft<sup>2</sup>); J/(sec)(m<sup>2</sup>)

#### Subscripts:

- b bulk condition
- c coolant
- crit critical valve
- f freezing point
- H<sub>2</sub> hydrogen side of heat exchanger
- H<sub>2</sub>O water side of heat exchanger
- i inside flow divider
- ic center element inside flow divider
- in inlet condition
- l liquid
- o outside flow divider
- r rough



- s smooth
- t total (condition)
- w wall
- x axial position
- 1 with flow divider
- 2 without flow divider

# VI. THRUST NOZZLE

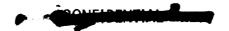
The work conducted on the regeneratively cooled nozzle of the TWMR has been limited to utilizing current technology available for nuclear rocket nozzles and applying it to the requirements of the TWMR. The design of the nozzle was divided into two areas: heat transfer and stress analysis. The heat-transfer calculations were performed for both the coolant tubes and the backup shell. A limited stress analysis was then performed taking into consideration both the pressure loading and thermal loading due to the temperature gradients.

# HEAT TRANSFER AND PRESSURE DROP IN NOZZLE TUBES

When the coolant tubes were designed for the TWMR nozzle, basic performance requirements were outlined to maintain rocket system compatibility. The first requirement was to maximize the temperature increase of the coolant fluid (hydrogen). The TWMR contains a heat exchanger for maintaining the moderator water below 700° R (389° K). The heat-exchanger coolant is the hydrogen leaving the nozzle coolant tubes. To prevent icing of the heat exchanger, it is desirable to preheat the hydrogen as much as possible. The energy added to the hydrogen also increases the power available in the rocket topping turbine at some sacrifice in specific impulse.

Since any increase in heat transferred to the hydrogen coolant will tend to increase the pressure drop in the coolant passages, some compromise is necessary in any design. For the purposes of this study, a maximum allowable pressure drop of 200 psi  $(138 \text{ N/cm}^2)$  was established in order to narrow the range of variables investigated. This value was chosen considering performance of existing nozzles.

The third requirement resulted from the choice of an Inconel alloy as the tube material. For tube wall temperature,  $2460^{\circ}$  R ( $1370^{\circ}$  K) was used as a reasonable upper limit. Finally, the fluid velocity of the coolant was limited to Mach 0.50. This require-



ment is primarily to maintain conservatism in preventing a choked flow condition due to flow maldistribution in the tubes.

These requirements were used to make a design study of the nozzle to determine the effect of various parameters on the nozzle performance. The results of these studies are reported in reference 36. The selection of the reference-design nozzle was based on this work. The assumptions made and analytical techniques used in the design study are summarized in this section. Additional details are given in reference 37.

A nozzle throat contour and a bell-shaped exit cone suitable for the reference-design chamber pressure and temperature were selected based on designs presented in reference 37. A  $40^{\circ}$  convergent section was used to complete the nozzle contour. The nozzle chamber conditions and flow rate are requirements of the rocket system, based on its estimated performance. These values at 100 percent reactor power are chamber pressure, 600 psi (414 N/cm<sup>2</sup>); chamber temperature,  $4460^{\circ}$  R ( $2480^{\circ}$  K); hot gas flow rate, 90.3 pounds per second (41 kg/sec); and coolant flow rate through the tubes, 92.7 pounds per second (42.1 kg/sec).

A second assumption based on other work is the type of construction selected for study. There are two advantages for the tubular configuration used and shown in figure 107. First, manufacturing methods for this type of tube have been established. Second, for any given diameter of the nozzle contour, the total tube flow area can be independently determined by choosing the b dimension. The number of tubes is held constant and is chosen to give reasonable values of b and tube height to width ratio for the desired flow areas. The reference-design nozzle has 224 tubes.

Although an actual flight nozzle will probably have an area ratio of the order of 100, for heat-transfer and pressure-drop purposes, the nozzle was convectively cooled out to an area ratio of 40. Beyond this area ratio, such cooling is no longer required. There is little advantage in extending the cooling tubes beyond this ratio since the amount of heat which would be added to the coolant is small.

The remaining design assumptions were made in order to simplify the calculations: effective heat-transfer area is 1.25 times that computed for the surface tangent to the coolant tubes (see fig. 107); one-dimensional slab-geometry heat-conduction analysis neglects circumferential and axial conduction, and nowhere does the hydrogen enter two-phase flow.

A heat-transfer computer program was used to obtain a balance between the hot-gasside heat flux entering the wall, the wall conduction process, and the heat flux carried away by the coolant. The nozzle coolant passages were divided into a number of stations along their flow length. The dimensions of the coolant passages (area and hydraulic diameter), the isentropic equilibrium properties of the hot gas, and the initial thermodynamic properties of the hydrogen were assigned to the respective stations. A more de-





tailed description of the calculational techniques used in the program is given in reference 36.

Several assumptions were made in determining the properties of the hot gas at each station. The calculation of these properties must account for the energy released by changes in chemical composition of the exhaust gas. Equilibrium flow was assumed during the isentropic expansion process. One-dimensional flow was assumed to occur in the convergent section. In the throat and exit cone, one-dimensional flow was modified as discussed in the following paragraphs.

A computer program (ref. 38) is available which provides nozzle temperatures and pressures at hydrogen equilibrium conditions in one-dimensional flow for assigned chamber temperature, pressure, and area ratios. The output data were corrected by using data on ratios between measured mass velocities and those predicted for one-dimensional flow in bell-shaped nozzles. These ratios, shown in figure 108, were applied to establish two-dimensional-flow properties at an equivalent one-dimensional flow position. Similar ratios for conical nozzles are given in reference 39. In addition to the isentropic properties, this program also provides the characteristic velocity of the hydrogen resulting in an accurate sizing of the nozzle throat using the expression

$$A = \frac{C*W}{(144)P_{ch}g}$$

The gas properties thus determined were used in the heat-transfer program to calculate wall temperatures on both the hot gas and coolant sides, coolant temperature, and coolant pressure at each station. In the course of the work reported in reference 36, several configurations were calculated. One of these, designated case 8B, performed quite well in the reference-design system. The calculational results for this case and others to be discussed are presented in table 19. Although further improvement may be possible, this design was adopted as the nozzle reference design. Figure 109 is a schematic drawing of the reference-design nozzle. Figure 110 is a plot of the coolant flow area, and figure 111 shows the results of the code calculations. These calculations do not include the nozzle extension, the cylindrical section between the converging section, and the core exit. An additional calculation, case 11 (table 19), was made taking into account the extension. It can be seen that the presence of the nozzle extension raises the coolant temperature by 17 R $^{\rm O}$  (9.4 K $^{\rm O}$ ) for a total  $\Delta T_{\rm C}$  of 136 $^{\rm O}$  R (75.6 $^{\rm O}$  K) and increases the pressure drop by about 1 psi (0.69 N/cm $^{\rm O}$ ) for a total  $\Delta P_{\rm C}$  of 133 psi (91.6 N/cm $^{\rm O}$ ) at full power

Several calculations were made to explore performance at off-design conditions of various parameters.



## Inlet Coolant Pressure (Case 19)

Inlet coolant pressure was changed from 1203 to 1500 psi (830 to 1033 N/cm $^2$ ) to measure the effect of such a change in operating conditions. Figure 112 is a plot of the results for this case. Comparison of these results as listed in table 19 with those of case 8B shows that the wall temperature is slightly lower, the  $\Delta P_c$  is lower by 22 psi (15.2 N/cm $^2$ ), and the temperature change is higher by 9 R $^0$  (5 K $^0$ ). Since this case represents quite a large change in inlet pressure, nozzle performance does not appear to be very sensitive to this parameter. Therefore, one could assume that the nozzle for an all-topping cycle would give the same sort of performance even though inlet pressures are higher. It may be of interest to note that the increase in temperature rise is accompanied by a decrease in pressure drop. The higher pressure level results in smaller changes in hydrogen density and therefore lower momentum pressure drops.

## Power Level and Flow Rate (Cases 101 and 302)

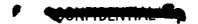
Conditions for these cases were reduced power and flow to maintain specific impulse at lower thrust. Inlet conditions for the nozzle were approximated by back-calculating pressure drops and temperature changes through system components downstream of the nozzle. The results appear in table 19 and in figure 113. Wall temperatures are lower than at full power and pressure drops are lower. The coolant temperature rise in both cases, however, is higher at these low powers than at full power.

## Power Level (Cases 200, 201, and 202)

These cases were made for operating conditions in which the flow was kept at 60 percent of full flow but the power was at less than 60 percent of full power. The result was reduced chamber temperature and pressure in the nozzle. Wall temperatures were, of course, lower for these cases than for case 101 in which flow and power were both 60 percent. Case 200 (47 percent power) results are plotted in figure 113(a) for comparison with those for case 101. In case 201, the effect on the nozzle of bypassing about 20 percent of the flow around the nozzle cooling passages and heat exchanger was investigated. The resulting maximum wall temperature was 67° R (37.2 K°) over case 200 at the same power with no coolant bypass.

Case 202 shows again the effect of changing nozzle coolant inlet pressure, this time at reduced power and specific impulse. The inlet pressure for this case is 481 psi  $(331 \text{ N/cm}^2)$  compared with 627.5 psi  $(432 \text{ N/cm}^2)$  for case 200. In this instance again,





as in cases 8B and 19, increasing inlet pressure had a small effect in increasing the temperature change and reducing the pressure drop.

## Other Calculations

Case 13 was a calculation for full power operation with a wall thickness of 0.006 inch (0.15 mm) instead of 0.010 inch (0.25 mm). Wall temperatures for this case were lower.

The remainder of the cases listed in the table were run at various reduced powers and a variety of chamber temperatures to get some idea of the operating map for the reference design. None of them indicated any problem with regard to overtemperature of the cooling tubes or unusual coolant temperature rise or pressure drop behavior. Some of the values listed were used to check the computer representation of the nozzle used in system dynamic and control studies. Results of this work are presented in reference 4.

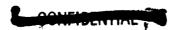
## NOZZLE TUBE STRESS ANALYSIS

Calculations were made to estimate the hoop stresses in the nozzle tubes for the 100 percent power case. Longitudinal stresses in the tubes were not calculated. The following assumptions were made for these calculations:

- (1) Nozzle tubes and backup shell are fabricated from Inconel X.
- (2) Chamber pressure is contained by the backup shell and not the tube bundle.
- (3) The axial position of the most critical stress condition coincides with that of the maximum tube temperature.
  - (4) The average circumferential tube temperature determines its expansion.
  - (5) The backup shell is at  $530^{\circ}$  R (294° K).
  - (6) Calculations assumed elastic behavior and no internal heat generation.

The maximum temperature of the tube wall occurs on the hot gas side of the tube (point A in fig. 107) and is shown in figure 111 to be approximately 3 inches (7.62 cm) upstream of the throat. Stresses present in the tube wall at this point are thermal, internal pressure, compressive, and bending. The superposition of each of these was used to determine the total stress in the tube wall at point A of the hottest axial region.

The main thermal stresses in the tube wall are caused by the temperature gradient which exists in the tube thickness between the coolant side and hot gas side. This results in compression at the hot side and tensions at the cold side of the following magnitude:





$$\sigma_{\theta B} = \frac{E\alpha(T_{GW} - T_{CW})}{2(1 - \gamma)}$$

A tensile hoop stress exists in the tube wall resulting from the pressure difference across the tube wall. The internal pressure of the coolant is higher than that of the hot gas in the nozzle. The magnitude of this hoop stress is

$$\sigma_{\Delta P} = \frac{(P_{CS} - P_{GS})r}{t}$$

The final two stresses considered, compressive and bending, are the result of the tangential load U shown in figure 107. This load results from the radial restraint of the cool backup shell on the tube bundle. Such a load causes stresses at point A which are opposite in direction to both the tube wall bending and pressure difference stresses. If only the stresses in the tubes normal to their axis are considered, it would appear that a rigid backup shell might reduce the net stress. Such a rigid shell, however, would also increase the restraint of the hot portions of the tube wall in the axial direction causing increased longitundinal compressive stresses and a tendency to buckle tube walls. The final compromise between these two tendencies must result from detailed stress and strain analyses of both plastic and creep behavior of the structure. For the present calculations, a reasonable degree of restraint was chosen based on an average hoop stress of 34 000 psi (2.34×10<sup>2</sup> N/cm<sup>2</sup>) in the backup shell wall. (A lower stress would represent higher values of U and decreased net stresses in the tube wall.) This assumed value for stress resulted from a qualitative consideration of stresses in the backup shell. Because a temperature gradient will exist across the backup-shell wall thickness, thermal stresses will exist that will cause little radial deformation. The rigidity of the backup shell depends on the stress available in the material to carry tangential loads after allowance has been made for the thermal stresses. Rough estimates of these thermal stresses indicated that, with the Inconel alloy at about room temperature, the assumed value for hoop stress is reasonable.

The diametral force per unit length U on the tubes was calculated from the difference in deformation between the individual tube and the portion of the backup shell associated with it. Increase of the tube diameter results from unrestrained growth due to pressure difference  $\delta_{\Delta P}$  and increase in temperature  $\delta_{\Delta T}$ . Expressions for these quantities are

$$\delta_{\Delta P} = \frac{2(P_{CS} - P_{GS})r^2}{Et}$$

## CONFIDENTIAL

$$\delta_{\Delta T} = 2r\alpha \Delta T$$

The increase in the length of the portion of the shell associated with one tube due to the hoop stress is

$$\delta_{\mathbf{S}} = \frac{2\mathbf{r}\sigma_{\mathbf{S}}}{\mathbf{E}}$$

The net deformation of the tubes caused by the force U is

$$\delta_{tot} = \delta_{\Delta P} + \delta_{\Delta T} - \delta_{S}$$

From the expression in reference 40 for deformation of a tube due to a concentrated diametral force acting along the entire length,

$$U = \frac{\delta_{\text{tot}} E t^3}{(1 - \nu^2) r^3 1.789}$$

In all calculations to determine U, material properties at the average circumferential tube temperature were used. The resulting tensile bending stress at point A from the same reference is

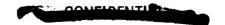
$$\sigma_{\rm B} = \frac{1.092~\rm Ur}{t^2}$$

The compressive membrane stress due to the force U is

$$\sigma_{\mathbf{U}} = \frac{\mathbf{U}}{2\mathbf{t}}$$

The compressive stress at the hot surface of the tube, point A, is equal to the sum of the bending and pressure stresses,  $\sigma_B + \sigma_{\Delta P}$ , subtracted from the sum of the membrane stress and thermal stress,  $\sigma_u + \sigma_{\theta B}$ .

Calculations were made for full-power operation with three different nozzle tube thicknesses: 0.010, 0.008, and 0.006 inch (0.254, 0.203, and 0.152 mm), and the results are given in table 20. Included in the table are the stresses in the tube wall with no restraint by the backup shell. It can be seen that the thermal stresses due to the temper-



ature gradient across the tube wall predominate. As wall thickness decreases, the temperature gradients decrease and the total stress picture improves. For 10 hours of operation at a maximum temperature of  $1700^{\circ}$  R ( $944^{\circ}$  K), all three thicknesses appear to be satisfactory for Inconel X if the backup-shell rigidity is taken into account. If there is no backup-shell rigidity, the 0.010-inch (0.254 mm) design may be somewhat marginal.

## HEAT TRANSFER AND STRESS IN FLANGE AND BACKUP SHELL

The tube assembly which forms the nozzle contour for the hot gases is a brazed assembly that in itself cannot withstand high pressure loads. A backup shell, therefore, is required from the gas inlet region extending past the throat. A flange for attachment of the nozzle to the reactor pressure vessel is incorporated into the backup shell (see fig. 109).

The static pressure of the hot gases exhausting through the nozzle at 100 percent power varies from 600 psia (414  $\rm N/cm^2$  abs) in the chamber to 1.2 psia (0.83  $\rm N/cm^2$  abs) at an area ratio of 40. The backup shell extends from the high-pressure region past the throat section terminating where the hot gas static pressure has been reduced to 33 psia (22.8  $\rm N/cm^2$  abs). Beyond this region, continuous support of the brazed tube assembly is not required.

The flange and backup shell structure must be designed so that internal heat generation due to gamma radiation does not result in either excessive metal temperatures or prohibitive thermal gradients. These requirements are particularly important in the flange region.

Although the flange and backup shell constitute an integral assembly, the heat-transfer analyses were conducted separately. The work on the flange was aimed at determining the extent to which complicated cooling passages have to be incorporated into the flange. It was also desirable to determine what coolant flow rates and pressure drops would be necessary to accomplish the required temperature control of the flange. It was assumed that the flange coolant would be bled from the plenum into which the nozzle tubes empty and bypass the heat-exchanger rejoining the main flow at the topping turbine.

The amount of material in the flange determines the cooling requirements. The flange width is determined by bolting and seal requirements and the flange depth by the pressure differential across the joint. Cooling is easiest to achieve on the inner and outer circumferential flange surfaces. From flange bolting and seal layouts, it appeared that a 2.0- to 2.5-inch (5.1 to 6.4 cm) flange width is required. A check was made of the thermal gradients and temperature levels in such a flange with liquid hydrogen cooling on only the inner and outer circumferential surfaces.



The results of this estimate were not encouraging, therefore, a flange design incorporating an additional circumferential cooling passage at the middle of the flange width was adopted. This configuration is shown in figure 110. The heat-transfer behavior of this configuration was explored by using the model shown in figure 114 and making the following simplifying assumptions:

- (1) The overall flange structural width is approximately 2.40 inches (6.10 cm). The flange was treated as a straight bar.
- (2) The temperature distribution in the outer side of the flange is symmetrical, and adequate hydrogen flow on the outer periphery will be maintained to remove that portion of the heat not transferred to the coolant in the slot.
- (3) The heat-transfer coefficient  $h_f$  on the inner periphery is 1025 Btu/(hr)(ft<sup>2</sup>)( $^{O}F$ ) (2.1×10<sup>7</sup> J/(hr)(m<sup>2</sup>)( $^{O}K$ )) estimated from known flow conditions and hydrogen properties at 170<sup>O</sup> R (94.4  $^{O}K$ ).
- (4) The internal heat-generation rate due to gamma heating at the inner flange surface  $Q_o$  is  $4.06\times10^6$  Btu/(ft<sup>3</sup>)(hr) (1.51×10<sup>11</sup> J/(m<sup>3</sup>)(hr)).
- (5) The flange material below the slot is ignored, and the calculations are done for a 1-inch-thick (2.54 cm) flange. Resulting cooling mass flow requirements are therefore per inch (centimeter) of flange thickness.

With these assumptions and the given model, one-dimensional heat-transfer calculations were made. The slot was treated as a uniform flow passage with heat transfer to the fluid from its two sides. Radial temperature distributions in the flange material, coolant pressure drop, and coolant temperature rise were calculated. It was assumed further that hydrogen enters the slot and flows  $360^{\circ}$  around the flange.

The expression for the total heat generated in the inner portion of the flange, obtained by integrating the local volumetric heating rates, is (see fig. 114)

$$q = \frac{Q_0 A}{\mu_e} \left[ 1 - \exp(-\mu_e L_2) \right]$$

Of this, some portion is transferred to the coolant on the inner flange surface through the assumed heat-transfer coefficient  $h_f$ . The remainder is transferred to the coolant flowing in the slot. The heat-transfer correlation of reference 41 was used to determine the heat-transfer coefficient at the cooling slot surface,  $h_2$ :

$$h_2 = 0.0208 \frac{K_{CF}}{d} \left( \frac{\rho_{CF} V_{Cd}}{\mu_{CF}} \right)^{0.8} \left( \frac{\mu_{CF} C_{p_{CF}}}{K_{CF}} \right)^{0.4} \left( 1 + 0.0147 \frac{\mu_{CW} \rho_{C}}{\mu_{C} \rho_{CW}} \right);$$

$$\left[ h_2 = 4.26 \times 10^2 \frac{K_{CF}}{d} \left( \frac{\rho_{CF} V_{Cd}}{\mu_{CF}} \right)^{0.8} \left( \frac{\mu_{CF} C_{p_{CF}}}{K_{CF}} \right)^{0.4} \left( 1 + 0.0147 \frac{\mu_{CW} \rho_{C}}{\mu_{C} \rho_{CW}} \right) \right]$$

The heat balance at each coolant interface for the right side of the flange results in two equations which can be solved simultaneously for the wall temperature at the slot  $^{T}w$ . 2:

$$\frac{Q_{o}}{\mu_{e}} + \frac{K}{L_{2}} T_{w, 2} - T_{w, f} \left(\frac{K}{L_{2}} + h_{f}\right) + \frac{Q_{o}}{L_{2} \mu_{e}^{2}} \exp(-\mu_{e} L_{2}) - 1 + h_{f} T_{C, f} = 0$$

$$\frac{Q_{o}}{\mu_{e}} \exp(-\mu_{e}L_{2}) + T_{w,2}\left(\frac{K}{L_{2}} + h_{2}\right) - T_{w,f}\frac{K}{L_{2}} + \frac{Q_{o}}{L_{2}\mu_{e}^{2}} \left[\exp(-\mu_{e}L_{2}) - 1\right] - h_{2}T_{C} = 0$$

Once  $T_{w,\,2}$  is established, the maximum temperature in the inner portion of the flange  $T_{2,\,max}$  can be evaluated from the expression

$$T_{2, \max} = -\frac{Q_{0} \exp(-\mu_{e} x)}{\mu_{e}^{2} K} + x \left\{ \frac{T_{w, 2} - T_{w, f}}{L_{2}} + \frac{Q_{0}}{L_{2} \mu_{e}^{2} K} \left[ \exp(-\mu_{e} L_{2}) - 1 \right] \right\} + T_{w, f} + \frac{Q_{0}}{\mu_{e}^{2} K}$$

at

$$x = -\frac{1}{\mu_{e}} \ln \left( -\left\{ \frac{T_{w, 2} - T_{w, f}}{L_{2}} + \frac{Q_{o}}{L_{2}\mu_{e}^{2}K} \left[ \exp(-\mu_{e}L_{2}) - 1 \right] \right\} \frac{\mu_{e}K}{Q_{o}} \right)$$

The assumption regarding the symmetrical temperature distribution simplifies the treatment of the outer portion of the flange. The amount of heat transferred through the outer side of the slot can be determined directly as



$$q = \frac{Q_0 A}{\mu_e} \left\{ exp \left[ -\mu_e (L_2 + a) \right] - exp \left[ -\mu_e \left( L_2 + a + \frac{L_1}{2} \right) \right] \right\}$$

The heat flux through this side wall is then

$$\frac{\mathbf{q}}{\mathbf{A}} = \mathbf{h}_1(\mathbf{T}_{\mathbf{w}, 1} - \mathbf{T}_{\mathbf{C}})$$

and the wall temperature  $T_{w, 1}$  at the left side of the slot is

$$T_{w, 1} = \frac{Q_{o}}{\mu_{e}h_{1}} \left\{ exp\left[-\mu_{e}(L_{2} + a)\right] - exp\left[\mu_{e}\left(L_{2} + a + \frac{L_{1}}{2}\right)\right] \right\} + T_{C}$$

In determining the value of  $T_{w,1}$ , the heat-transfer coefficient  $h_1$  is calculated by using the same correlation from reference 41 cited previously. The equation for the maximum temperature in the outer portion of the flange that occurs at the midpoint of that region is

$$T_{1, \max} = -\frac{Q_{o}}{K\mu_{e}} \exp \left[ -\mu_{e} \left( L_{2} + a + \frac{L_{1}}{2} \right) \right] \left[ \frac{1}{\mu_{e}} + \left( L_{2} + a + \frac{L_{1}}{2} \right) \right] + T_{w, 1} + \frac{Q_{o}}{K\mu_{e}} \left\{ \frac{\exp \left[ -\mu_{e} (L_{2} + a) \right]}{\mu_{e}} + (L_{2} + a) \exp \left[ -\mu_{e} \left( L_{2} + a + \frac{L_{1}}{2} \right) \right] \right\}$$

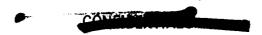
For each station N of the coolant circumferential flow, the coolant properties are determined from the enthalpy

$$i_{N+1} + \left[\frac{q}{A}(N-1)\right]_{Outer side} + \frac{q}{A}(N-1)\Big|_{Inner side}\right] \frac{A}{W}$$

The friction pressure drop  $\,\Delta P_{\mbox{\scriptsize f}}\,$  for each station is

$$\Delta P_{fN, N-1} = \frac{fL\rho_N v_N^2}{2gd}$$

The total friction pressure drop is



$$\Delta P_f = \sum_{N=1}^n \Delta P_{f, N}$$

The momentum pressure drop at each station is

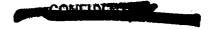
$$\Delta P_{m, N, N-1} = \frac{W}{A} (V_N - V_{N-1})$$

Total 
$$\Delta P_{m} = \sum_{N=1}^{n} \Delta P_{m, N}$$

Calculations of heat-transfer behavior were made for several versions of the interior slot configurations, and the results are given in table 22. The slot flow rate for all these calculations was 0.2 pound per second (90.8 g/sec), and the effects of slot width and slot location were investigated. At a flow rate of 21 pounds per second per square inch (180 g/(sec)(cm<sup>2</sup>)) for a 0.1-inch (2.54 mm) slot, the coolant pressure drop is 261 psi (180 N/cm<sup>2</sup>, case 1). Since the pressure drop available for flow bypassing the heat exchanger is approximately 35 psi (24.1 N/cm<sup>2</sup>), this is intolerable for such a flow scheme. The 0.2-inch (5.08 mm) slot (cases 2 to 4) with a flow rate of 1.0 pound per second per square inch (89.4 g/(sec)(cm<sup>2</sup>)) undergoes a much more reasonable pressure drop. The coolant temperature increase of  $250^{\circ}$  R ( $139^{\circ}$  K) for a flow of 0.2 pound per second (90.8 g/sec) appears to be satisfactory. The central location of the slot results in a maximum radial temperature difference of  $548^{\circ}$  R ( $305^{\circ}$  K).

Moving the slot closer to the region of high heat generation, cases 3 and 4, tends to reduce the maximum temperature difference in the right side of the flange. As this procedure continues, the maximum temperature difference shifts to the outer side of the flange, case 5. In general, the best slot location is that which results in equal gradients in both sides of the flange. For our flange width, heat-generation rate, and material, the slot located at approximately 0.85 inch (2.16 cm) from the inner edge results in equal temperature differences of  $390^{\circ}$  R ( $216^{\circ}$  K). This gradient results in a stress of approximately 58 000 psi ( $4\times10^{4}$  N/cm<sup>2</sup>). It would, therefore, appear that one interior cooling slot plus cooling on the inner and outer flange surfaces should be adequate at the maximum flange operating temperature of  $724^{\circ}$  R ( $402^{\circ}$  K).

Since there is a substantial circumferential gradient, it would appear desirable to establish at least two flow paths each covering  $180^{\circ}$  of the circumference. In that way, the temperature gradient would be spread over the entire diameter. With that arrangement, the slot widths could be reduced to 0.1 inch (2.54 mm) to maintain the flow at





1.0 pound per second per square inch (89.4  $g/(sec)(cm^2)$ ) so that the pressure drops would remain at the 40 psi (27.6  $N/cm^2$ ) level.

The cooling requirements for the bolts have not been investigated in this study. If good thermal contact with the flange can be established and maintained, the cooling provided for the flange may be sufficient. If not, a separate flow of hydrogen will have to be used for cooling the bolts.

The temperature distribution in the combined flange and backup shell was then investigated by using a steady-state multidimensional heat-transfer analysis. This analysis includes internal heat generation and heat transfer by radiation, conduction, and constant film and contact coefficients. A two-dimensional calculation of heat transfer in a longitudinal section of the backup shell assembly was made by using the model shown in figure 115. The resulting temperature distributions in a 0.5-inch (1.27 cm) backup shell are shown in figures 116 and 117.

The backup-shell temperature distributions were then used to calculate stresses in various regions of that component. The model and nomenclature for these calculations are shown in figure 118 and the following assumptions were made:

- (1) The exit end of the support shell is free. Integrated nozzle thrust forces to that point act on the end of the support shell.
  - (2) Coolant tubes offer no restraint to the nozzle pressure.
- (3) In the pressure shell portion of the backup shell, cross-sectional area was used to calculate an effective thickness. The actual moment of inertia of the shell cross section will be higher than that from the effective thickness.
  - (4) The pressure shell region experiences no temperature change.
- (5) The location of axial forces and reactions at the junction of the three shells result in a couple at that point.

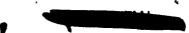
The stresses were calculated in three major steps:

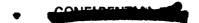
- (1) Stresses due to pressure loads only
- (2) Stresses due to both axial temperature gradients and pressure
- (3) Stresses due to radial temperature gradients

For calculations of the first two types, a computer program (ref. 42), was used to solve for stresses in thin shells with axial thermal gradients and axially symmetric loads. Since the program can only handle single continuous shells, the backup shell was broken into the three major components named flange, pressure, and support shells (see fig. 118).

Junction interactions among the three shells were determined from equilibrium and compatibility conditions after influence coefficients for unit junction loads were determined by using the same program. A final computer run was then made for each shell in which the junction interactions were inserted as boundary conditions.

The third type of stress calculation was a simplified form for thermal stress in a





thin cylinder with a temperature gradient through the wall. The total stress would result from the superposition of results of the second and third type of calculation.

One run was made for stresses due to pressure only, and the results are listed as case 1 of table 22. Stresses, displacements, forces, and moments are listed at specific locations. Two different runs were made for combined pressure and thermal stresses due to axial gradients to bracket the fixity situation at location FS1. Since the model describes this point as a fixed point, any flexibility of the flanged joint will reduce the calculated discontinuity stresses. Behavior similar to a difference in degree of fixity can be achieved by assuming different temperature levels for the zero thermal deformation condition. The first of two calculations (case 2, table 21) was made by assuming no thermal deformation at room temperature and represents a high degree of flange fixity. The second (case 3, table 21) was made by assuming no thermal deformation at a temperature of  $970^{\circ}$  R ( $539^{\circ}$  K), previously calculated at point FS1 and represents a lower degree of flange fixity. The actual stress and deformation condition for the flange shell region should fall somewhere between the results calculated for these two cases. The more accurate results for the pressure and support shells are those from case 2.

The thermal stresses due to radial temperature gradients in the shell thickness at various points are listed in table 23. These stresses must be added to the results of the most accurate axial and pressure stresses from cases 2 and/or 3 of table 22 for the total stress condition. It is obvious from the calculational results listed in tables 22 and 23 that extensive plastic flow would result from the thermal gradients existing in the backup shell structure investigated.

Certain modifications to the design appear desirable to reduce these gradients:

- (1) The stresses due to the radial gradient through the wall thickness can be lowered by reducing the thickness as much as the pressure loads will permit. Since the stresses due to pressure loads with the present 0.5-inch (1.27 cm) thickness are small away from the discontinuities, improvement in this area is easily achieved.
- (2) The temperature of the thick junction of the three members comprising the backup shell should be reduced by decreasing thickness and supplying some additional cooling in that area.
- (3) Since the pressure shell is exposed to coolant on both surfaces, it tends to run much colder than the other two components. It would, therefore, appear advantageous to insulate the outer surface of this portion so that it is cooled on one side only.
- (4) The rigidity of the flanged joint between the nozzle and the reactor pressure vessel and the relative expansion of the two components is extremely critical. A careful exploration of these factors will be required in the evaluation of a satisfactory design.

The deformations of the backup shell are important at the location of the flange and especially at the location of the inner seal. The seal configuration, shown in figure 109, is sensitive to axial (vertical) displacement. Although this displacement is low for the



pressure loads, it is intolerably large due to the temperature difference between the pressure shell region and the flange shell region. Here again, insulation on the outer surface of the pressure shell would improve performance. A somewhat different approach to the seal configuration may merit consideration. If the inner assembly seal were directly attached to the flange, the temperature differences between the two members would not affect the sealing function. An axially flexible sealing member such as a large bellows convolution could then be used to join the inner seal assembly and the pressure shell, as shown in the alternate backup shell design in figure 119.

## SUMMARY OF NOZZLE STUDY RESULTS

The limited investigation of the propulsion nozzle design and performance conducted in conjunction with the TWMR program indicates the following results:

- (1) The design of the cooling passages of a regeneratively cooled nozzle can be optimized for this application in terms of temperature increase of the coolant and its pressure drop.
- (2) Cooling-tube structural problems are the same as those for other nuclear rocket nozzles. Reasonable designs for tube thickness considering stresses in the radial plane can be achieved.
- (3) The backup shell flange requires cooling in its interior regions as well as on its outer and inner periphery in order to reduce thermal stresses.
- (4) The design of the backup shell is critical and complex because of its shape and the variety of temperatures to which it is exposed. Special cooling to areas other than the flange may have to be provided, and other techniques such as insulation may have to be incorporated in order to reduce temperature differences in the structure.

## SYMBOLS

- A area, ft<sup>2</sup>; m<sup>2</sup>
- a slot width, ft; m
- b cooling tube height, ft; m
- C\* characteristic velocity, ft/sec; m/sec
- C<sub>n</sub> specific heat at constant pressure, Btu/(lb)(OR); J/(kg)(OK)
- d hydraulic diameter, ft; m
- E modulus of elasticity, psi; N/cm<sup>2</sup>

```
friction factor
f
                    gravitational constant, ft/sec<sup>2</sup>; m/sec<sup>2</sup>
 g
                    flange inner surface heat-transfer coefficient, Btu/(ft<sup>2</sup>)(sec)(OR);
 hf
                      J/(m^2)(sec)(^{O}K)
                    flange slot (outer side) heat-transfer coefficient, Btu/(ft<sup>2</sup>)(sec)(OR);
h_1
                      J/(m^2)(sec)(^{O}K)
                    flange slot (inner side) heat-transfer coefficient, Btu/(ft<sup>2</sup>)(sec)(OR);
h_2
                      J/(m^2)(sec)(^{O}K)
                    enthalpy, Btu/lb; J/kg
i
                    thermal conductivity of flange material, Btu/(ft)(sec)(OR); J/(m)(sec)(OK)
K
                    station fluid flow length, ft; m
 L
                    distance from outer flange surface to slot surface, ft; m
 L_1
                    distance from inner flange surface to slot surface, ft; m
 L_2
\mathbf{N}
                    station number
                    number of stations
n
P
                    pressure
                   coolant pressure drop, \Delta P_f + \Delta P_m, psi; N/cm<sup>2</sup>
\Delta P_c
                    friction pressure drop, psi; N/cm<sup>2</sup>
\Delta P_f
                    momentum pressure drop, psi; N/cm<sup>2</sup>
\Delta P_{m}
                    internal heat-generation rate at inner flange surface, Btu/(ft<sup>3</sup>)(sec);
Q_{0}
                      J/(m^3)(sec)
                   total heat, Btu/sec; J/sec
q
                    radius, in.; cm
r
                   temperature, OR; OK
T
                   coolant temperature rise, OR; OK
\Delta T_c
T_{w, f}, T_{w, 1}, T_{w, 2}, T_{c, f}
                   temperatures at various locations in flange model (see fig. 114), {}^{O}R; {}^{O}K
                    coolant tube wall thickness, in.; cm
                   diametral load, lb/in. of axial length; kg/cm of axial length
U
                   velocity, ft/sec; m/sec
V
```

## CONFIDENTIAL -

- W mass flow, lb/sec; kg/sec 
  x radial distance from inner flange surface, ft; m  $\alpha$  thermal coefficient of linear expansion, in./(in.)( $^{O}$ R); cm/(cm)( $^{O}$ K)  $\delta_{\Delta P}$  diametral increase (pressure), in.; cm
- $\delta_{\mathbf{S}}$  diametral increase (hoop), in.; cm
- $\boldsymbol{\delta_{\Delta T}}$  diametral increase (temperatre), in.; cm
- $\delta_{\mathrm{tot}}$  total diametral increase, in.; cm
- $\mu$  absolute viscosity, lb/(ft)(sec); kg/(m)(sec)
- $\mu_{\rm e}$  energy absorption coefficient for gamma rays, ft<sup>-1</sup>; m<sup>-1</sup>
- ν Poisson's ratio
- $\rho$  density, lb/ft<sup>3</sup>; kg/m<sup>3</sup>
- $\sigma_{\rm R}$  bending stress, psi; N/cm<sup>2</sup>
- $\sigma_{\Lambda P}$  hoop stress, psi; N/cm<sup>2</sup>
- $\sigma_{\rm S}$  hoop stress backup shell, psi; N/cm<sup>2</sup>
- $\sigma_{
  m tot}$  sum of hoop, bending, membrane, and thermal stresses, psi; N/cm $^2$
- $\sigma_{\rm II}$  membrane stress, psi; N/cm<sup>2</sup>
- $\sigma_{ heta B}$  thermal stress, psi; N/cm<sup>2</sup>

## Subscripts:

- C coolant bulk
- CF coolant film
- ch chamber
- CS coolant bulk static
- CW coolant wall
- GS hot gas bulk static
- GW hot gas wall
- max maximum
- 1 outer portion of flange
- 2 inner portion of flange



## REFERENCES

- 1. Lietzke, A. F.: Feasibility Study of a Tungsten Water Moderated Nuclear Rocket.

  III. Fuel Elements. TM X-1422, estimated publication, approximately, Dec. 1967.
- 2. Heath, Colin A.: Pressure Measurements in Water-Moderator Crossover Region of Tungsten Water-Moderated Reactor. NASA TM X-1387, 1967.
- 3. Levin, S. A.; Hatch, D. C.; and von Halle, E.: The Separation of Tungsten-184. Rep. No. KOA-865, Oak Ridge Gaseous Diffusion Plant, 1961; also presented at Space Nuclear Conference, Gatlinburg, Tenn., May 3, 1961.
- 4. Marcy, R.; Cannon, W.; and Bulgier, L.: Engine System Analysis for TWMR Nuclear Rocket. Rep. No. R-6797 (NASA CR-72120), Rocketdyne Div., North American Aviation, Nov. 15, 1966.
- 5. Pierce, B. L.: A Multiple Channel Analysis Program (MCAP) for the Temperature Distribution in an Internally-Cooled Heat Generating Solid Cooled by a Compressible Gas. Rep. No. WANL-TME-944, Westinghouse Electric Corp., Mar. 19, 1962.
- 6. Miller, John V.; Davison, Harry W.; Mihaloew, James R.; Paulson, Water A.; and Ribble, Guy H., Jr.: Fluid Systems and Control. Nuclear Rocket Technology Conference. NASA SP-123, 1966, pp. 263-299.
- 7. Hogerton, J. F.; and Grass, R. C., eds.: Engineering. Vol. 2 of Reactor Handbook. USAEC, May 1955, p. 166.
- 8. O'Donnell, W. J.; and Langer, B. F.: Design of Perforated Plates. J. Eng. Industry, vol. 84, no. 3, Aug. 1962, pp. 307-320.
- 9. Linn, F. C.; and Culver, D. H., eds.: Heat Transfer Reactor Experiment No. 3. Rep. No. APEX-906, General Electric Co., 1962, p. 93.
- 10. Cox, T. H.; Gjertsen, R. K.; Guenther, E., Jr.; Kaufman, S.; Schumann, F. A.; and Trushin, J. K.: Fuel Assembly Design Study for the Tungsten Water-Moderated Reactor (TWMR). Rep. No. MND-3271 (NASA CR-72024), Martin Co., Aug. 31, 1966.
- 11. Aase, D. T.; Kempf, F. J.; O'Keefe, D. P.; Townsend, W. C.; and Trent, D. S.: Tungsten Water Moderated Reactor Fuel Support Design Analysis. Battelle-Northwest (NASA CR-72031), Aug. 1966.
- 12. Eckert, E. R. G.; and Drake, Robert M., Jr.: Heat and Mass Transfer. Second ed., McGraw-Hill Book Co., Inc., 1959, pp. 328-331.
- 13. McAdams, William H.: Heat Transmission. Third ed., McGraw-Hill Book Co., Inc., 1954, p. 297.



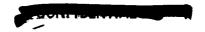
- 14. Einstein, Thomas H.: Analysis of Heat Transfer and Pressure Drop for a Gas Flowing Through a Set of Multiple Parallel Flat Plates at High Temperatures. NASA TN D-1165, 1961.
- 15. Miller, John V.; and Taylor, Maynard, F.: Improved Method of Predicting Surface Temperatures in Hydrogen-Cooled Nuclear Rocket Reactor at High Surface- to Bulk-Temperature Ratios. NASA TN D-2594, 1965.
- 16. Buskirk, D. L.: A Method of Statistical Analysis of the Effects of Manufacturing, Assembly, and Operating Deviations on Operating Temperature of the NRX-A Core. Rep. No. WANL-TME-539, Westinghouse Electric Corp., Aug. 1963.
- 17. Thomas, G. R.; and Nelson, P. A.: A Method of Statistical Analysis of the Effects of Manufacturing Tolerances and Other Deviations on Operating Temperatures of the Nerva B-4 Core. Rep. No. WANL-TNR-057, Westinghouse Electric Corp., Apr. 1962.
- 18. Hoel, Paul G.: Introduction to Mathematical Statistics. Third ed., John Wiley & Sons, Inc., 1962, p. 137.
- 19. Eanes, W. F.: Feasibility of a Chemical Poison Loop System. Task I. Analysis of Reference System. Rep. No. WCAP-2690 (NASA CR-54291), Westinghouse Electric Corp., Feb. 1965.
- 20. Eanes, W. F.: Feasibility of a Chemical Poison Loop System. Task II. Design of Laboratory Tests. Rep. No. WCAP (NASA CR-54420), Westinghouse Electric Corp., June 1965.
- 21. Engel, F. C.; and Bishop, A. A.: Feasibility of a Chemical Poison Loop System.

  Task 3a. Test and Analysis of a Manifold and Reentrant Tube Assembly. Rep. No.

  WCAP-2870 (NASA CR-54994), Westinghouse Electric Corp., July 1966.
- 22. Fultonberg, D. N.; and Taylor, G. R.: Feasibility of a Chemical Poison Loop System. Task 3b. Experimental Program to Investigate Stability, Compatibility and Corrosion of Poison Solutions and Structural Materials. Rep. No. WCAP-2867 (NASA CR-54995), Westinghouse Electric Corp., July 1966.
- 23. Eanes, W. F.; Fultonberg, D. N.; Rosal, E. R.; Fletcher, W. D.; and Loving, J. J.: Feasibility of a Chemical Poison Loop System. Rep. No. WCAP-2993 (NASA CR-72105), Westinghouse Electric Corp., Sept. 1966.
- 24. Griess, J. C.; Jenks, G. H.; Eissenberg, D. M.; and Bohlmann, E. G.: An Evaluation of the Chemical Problems Associated with the Aqueous Systems in the Tungsten Water Moderated Reactor. Rep. No. ORNL-TM-913 (NASA CR-54198), Oak Ridge National Lab., Aug. 1964.

- 25. Jenks, G. H.; Bohlmann, E. G.; and Griess, J. C.: An Evaluation of the Chemical Problems Associated with the Aqueous Systems in the Tungsten Water Moderated Reactor. Addenda 1 and 2. Rep. No. ORNL-TM-978 (NASA CR-54214), Oak Ridge National Lab., Mar. 1965.
- 26. Kaufman, Samuel J.: Feasibility Study of a Tungsten Water-Moderated Nuclear Rocket. I. Summary Report. NASA TM X-1420, 1967.
- 27. Cavicchi, Richard H.: Mapping a Tungsten-Reactor Rocket Engine as a Guide to Operation and Control. NASA TN D-3840, 1967.
- 28. Jenks, G. H.; Savage, H. C.; and Bohlmann, E. G.: NASA Tungsten Reactor Radiation Chemistry Studies. Rep. No. ORNL-TM-1630 (NASA CR-72070), Oak Ridge National Lab., Oct. 1966.
- 29. Davison, Harry W.; Heath, Colin A.; and Lowen, Walter: Control of a Nuclear Reactor with a Gaseous Control System. NASA TN D-4093, 1967.
- 30. Klann, Paul G.; Mayo, Wendell; Lantz, Edward; and Paulson, Walter A.: Feasibility Study of a Tungsten Water-Moderated Nuclear Rocket. IV. Neutronics.

  NASA TM X-1423, estimated publication, approximately Dec., 1967.
- 31. Fiero, Ivan B.; Miller, John V.; and Ribble, Guy H.: Analysis and Full-Scale Water Flow Testing of the Tungsten Water-Moderated Nuclear Reactor. NASA TM X-1369, 1967.
- 32. Busch, J. S.; Lynn, L. L.; and Bonilla, C. F.: The Calculation of Pressure Drop and Flow Distribution within a Reactor Vessel in a Pressurized Water Nuclear Reactor System. Rep. No. WAPD-217, Westinghouse Electric Corp., Aug. 1959.
- 33. Durant, William S.; Towell, Robert H.; and Mirshak, Samuel: Improvement of Heat Transfer to Water Flowing in an Annulus by Roughening the Heated Walls. Paper presented at the AIChE Nuclear Engineering Heat Transfer Symposium, Chicago, Dec. 2-5, 1962.
- 34. Siegel, Robert; and Savino, Joseph M.: An Analysis of the Transient Solidification of a Flowing Warm Liquid on a Convectively Cooled Wall. Proceedings of the Third International Heat Transfer Conference, Chicago, Aug. 7-12, 1966. AIChE-ASME, 1966, vol. 4, pp. 141-151.
- 35. Fultonberg, D. N.: Corrosion of Aluminum in Water. Rep. No. WCAP-7029 (NASA CR-72193), Westinghouse Electric Corp., 1967.
- 36. Puthoff, Richard L.: A Design Study of a Regeneratively Cooled Nozzle for a Tungsten Water Moderated Nuclear Rocket System. NASA TN D-3771, 1966.



- 37. Neumann, Harvey E.; and Bettinger, Paula J.: A Comparative Analysis of Convective Heat Transfer in a Nuclear Rocket Nozzle. TN D-1742, 1963.
- 38. Gordon, Sanford; Zeleznik, Frank J.; and Huff, Vearl N.: A General Method for Automatic Computation of Equilibrium Compositions and Theoretical Rocket Performance of Propellants. NASA TN D-132, 1959.
- 39. Back, L. H.; Massier, P. F.; and Gier, H. L.: Convective Heat Transfer in a Convergent-Divergent Nozzle. Tech. Rep. No. 32-415, Rev. 1 (NASA CR-57326), Jet Propulsion Lab., California Inst. Tech., Feb. 15, 1965.
- 40. Rohde, John E.; Duscha, Rudolph A.; and Derderian, George: Digital Codes for Design and Evaluation of Convectively Cooled Rocket Nozzle with Application to Nuclear-Type Rocket. NASA TN D-3798, 1967.
- 41. Hess, H. L.; and Kunz, H. R.: A Study of Forced Convection Heat Transfer to Supercritical Hydrogen. J. Heat Transfer, vol. 87, no. 1, Feb. 1965, pp. 41-48.
- 42. Sepetoski, W. K.; Pearson, C. E.; Dingwell, I. W.; and Adkins, A. W.: A Digital Computer Program for the General Axially Symmetric Thin-Shell Problem. J. Appl. Mech., vol. 29, no. 4, Dec. 1962, pp. 655-661.

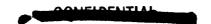


TABLE 1. - NUCLEAR AND PHYSICAL PROPERTIES OF MATERIALS

Materials	Dens	ity	Macro- scopic cross	i -	ermal expans emperature t indica	o ten	perature	The	ermal conduc ature ind		•	Young's r	modulus, E
	lb/in. <sup>3</sup>	g/cm <sup>3</sup>	section, $\Sigma_{a}$ , cm <sup>-1</sup>	°R	in./in./ <sup>0</sup> R	°K	cm/cm/ <sup>0</sup> K	°R	Btu (hr)(ft <sup>2</sup> )(OR)	°к	J (hr)(m <sup>2</sup> )( <sup>0</sup> R)	psi	N/cm <sup>2</sup>
Aluminum 6061 and 6067	0.098	2.72	0. 026	760	13. 3	422	23. 9	760	111	422	6.91×10 <sup>5</sup>	9. 0×10 <sup>6</sup>	6.21×10 <sup>6</sup>
Inconel X-750	. 298	8. 25	. 359	860	7.2	478	13.0	860	10.4	478	6.48×10 <sup>4</sup>	30. 0	20.7
Ti-6Al-4V	. 160	4.43	. 309	860	5.0	478	9.0	860	5, 1	478	3. 18	14. 0	9.65
Zircaloy-2	. 237	6.56	. 009	860	4.6	478	8, 28	860	7.2	478	4.48	11.5	7.94
304 Stainless steel	. 286	7.92	. 308	860	7.5	478	13.5	860	9.7	478	6.04	30.0	20.7

TABLE 2. - EQUIPMENT LIST

[Data recording system has flat response,  $\pm 3$  dB, over frequency range 5 cps to 2 kcps (5 Hz to 2 kHz).]

Description	Amplitude range	Frequency range (±3 dB)
Isoply power supplies	12 to 15 V(dc)	(a)
Preston Model 8300 am- plifiers	±10 V; ±100 mA (peak)	dc to 10 kcps
Honeywell M3300 galva- nometers	±3 in. (±7.62 cm)	dc to 2 kcps
Endevco Model 2226 accel- erometers	±1000 g's (peak)	10 cps to 5 kcps
Budd strain gages, Type C6-121	±3000 μin./in. (μm/m) (max)	dc to 10 kcps (min)
Honeywell Model 1612 oscillograph	(a)	(a)
Endevco charge amplifiers,	±100 mA (peak)	2 cps to 20 kcps
Model 2711A	_	(2 Hz to 20 kHz)
MB vibration exciter	28 000 lb (1.245×10 <sup>5</sup> N)	5 cps to 2 kcps
Model C210	maximum force	(5 Hz to 2 kHz)

a<sub>Not</sub> applicable.



# TABLE 3. - SUPPORT TUBE RESPONSE IN ABSENCE

## OF PRESSURE TUBES

+		Mation, in (cm)	in)	
33	32 (81.3)	53 (135)	30 (76.2)	30 (76.2)
stre	Bending stress, psi $(\mathrm{N/cm}^2)$	1/cm <sup>2</sup> )	Accel-	Deflection,
			eration,	in. (mm)
		-	В	
8 2(	00 (126)	2110 (14.6)	9.75	2500 (17.2) 18 200 (126) 2110 (14.6) 9.75 0.0596 (1.51)

## OF SUPPORT TUBE

TABLE 4. - PRESSURE TUBE RESPONSE IN ABSENCE

	40 (102)			225 (1. 55)		340 (2.34)
Station, <sup>a</sup> in. (cm)	15 (38.1) 13.5 (34.3) 26.5 (67.3)	Bending stress, psi $(N/cm^2)$	acket	1095 (7.56) 515 (3.55) 1115 (7.70) 225 (1.55)	cket	900 (6.21) 1620 (11.2) 340 (2.34)
Station, <sup>a</sup>	13. 5 (34. 3)	ending stress	No water in jacket	515 (3.55)	Water in jacket	900 (6.21)
	15 (38.1)	<b>д</b>		1095 (7.56)		1530 (10.6)
Fre-	quency,			154		42

<sup>a</sup>See fig. 27.

# TABLE 5. - SUPPORT TUBE AND PRESSURE TUBE BENDING STRESSES

[First mode resonance.]

Fre-	ž				Bending stress, psi (N/cm <sup>2</sup> )	s, psi (N/cm	1,2)			
quency	springs			Support tube				Pressu	Pressure tube	
					Station, a	Station, <sup>a</sup> in. (cm)				
		16. 5 (41. 9)	27. 25 (69. 3)	32. 0 (81. 3)	38. 0 (96. 5)	53. 0 (135)	1. 5 (3. 81)	13. 5 (34. 3)	53. 0 (135) 1. 5 (3.81) 13. 5 (34. 3) 26. 5 (67. 4) 40. 0 (102)	40. 0 (102)
					Water in jacket					
39	0	2990 (2060)	23 300 (16 100)	28 400 (19 600)	2990 (2060) 23 300 (16 100) 28 400 (19 600) 28 900 (19 900)	æ	1995 (1375)	<u></u> ê	<u>(</u>	æ
39	-	2650 (1827)	2650 (1827) 7 530 (5 190)	8 500 (5 860)	8 500 (5 860) 8 500 (5 860) 910 (627)	910 (627)	1940 (1338)	<u> </u>	2210 (1520)	<b>a</b>
39	7	4325 (2980)		7 000 (4 830)	7 050 (4 860) 7 000 (4 830) 6 875 (4 740) 600 (414)	600 (414)	· @	890 (614)	2220 (1530)	39
37	က	5270 (3635)		7 460 (5 140)	7 460 (5 140) 6 650 (4 590) 650 (448) 2190 (1510)	650 (448)	2190 (1510)	940 (648)	2240 (1540)	630 (434)
					No water in jacket	*				
41	0	2870 (1980)	22 300 (15 400)	26 400 (18 200)	2870 (1980) 22 300 (15 400) 26 400 (18 200) 27 700 (19 100)	(a)	1220 (841)	æ	1025 (106)	(Q)
53	-	2870 (1980)	5 910 (4 070)	6 130 (4 220)	2870 (1980) 5 910 (4 070) 6 130 (4 220) 8 760 (6 040)	585 (403)	1330 (916)	. <u>(</u> 2	1525 (1050)	<u> </u>
53	67	4350 (3000)		6 000 (4 140)	5 370 (3 700) 6 000 (4 140) 8 920 (6 150) 780 (538)	780 (538)	(2)	615 (424)	1940 (1340) 170 (117)	170 (117)
75	8	4810 (3320)		5 750 (3 960)	5 200 (3 580) 5 750 (3 960) 7 070 (4 870) 370 (255) 1460 (1008) 473 (326) 1755 (1210) 270 (186)	370 (255)	1460 (1008)	473 (326)	1755 (1210)	270 (186)
									,	()

 $^{\rm a}{\rm See}$  figs. 26 and 27 for station locations.  $^{\rm b}{\rm Strain}$  gage inoperative.

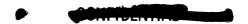


TABLE 6. - HEAT TRANSFER AND FLOW CONDITIONS FOR CONCENTRIC

## CYLINDER REFERENCE DESIGN

Conditions	U.S. Customary units	SI units
Inlet coolant gas temperature (all assemblies), OR; OK	322	179
Outlet coolant gas temperature (all assemblies), OR; K	4460	2475
Maximum power fuel assembly:		
Fuel assembly heat-generation rate, Btu/sec; J/sec	15 190	1.6×10 <sup>7</sup>
Coolant gas flow rate, lb/sec; kg/sec	0.9566	0.434
Inlet gas pressure, psia; N/cm <sup>2</sup> abs	712	491
Gas pressure drop, psi; N/cm <sup>2</sup>	124	85. 5
Assembly outlet average dynamic head, psi; $\mathrm{N/cm}^2$	12.75	8.80
Assembly outlet average Mach number	0.184	
Heat loss to pressure tube, Btu/sec; J/sec	26.64	$2.815 \times 10^4$
Highest support tube temperature in region of fuel stages, OR; OK	3984	2210
Highest support tube temperature, OR; OK	4500	2500
Highest fuel surface temperature, OR; OK	4894	2720
Highest inlet Reynolds number	136 000	
Lowest outlet Reynolds number	13 000	
Dimensions of all fuel assemblies (hot):		
Number of stages in each fuel assembly	26	
Number of fuel cylinders in each stage	10	
Stage length, in.; cm	1. 500	3.81
Inner radius of pressure tube, in.; cm	1.190	3.02
Radial width of insulation annulus, in.; cm	0.120	3.05
Unfueled support tube thickness, in.; mm	0.015	0.381
Thickness of each fuel cylinder, in.; mm	0.021	0.534
Outer radius of unfueled center tube, in.; mm	0. 197	5.0
Radial width of innermost flow annulus, in.; mm	0.041	1.04
Radial width of second to ninth flow annuli, in.; mm	0.063	1.60
Radial width of tenth flow annulus, in.; mm	0.057	1.45
Radial width of eleventh flow annulus, in.; mm	0.046	1.17
Total flow area in eleven annuli, in. <sup>2</sup> ; cm <sup>2</sup>	2. 549	16.43
Total wetted surface area in each stage, in. 2; cm <sup>2</sup>	129.772	836
Total fuel surface area in each stage, in. <sup>2</sup> ; cm <sup>2</sup>	117.972	760

TABLE 7. - EFFECT OF ZONING

Assumed conditions and results	Unzoned	Zoned
Peak-to-average power	1.320	1.460
Stage where peak power occurs	13	9
Highest fuel surface temperature, OR; OK	5051; 2810	4894; 2720
Inlet pressure, psia; N/cm <sup>2</sup> abs	717; 495	717; 495
Pressure drop, psi; N/cm <sup>2</sup>	112; 77.2	124; 85.5
Highest outlet dynamic head, psi; N/cm <sup>2</sup>	13.00; 8.96	13.25; 9.13



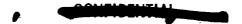


## TABLE 8. - FUEL SURFACE TEMPERATURE FACTOR

## UNCERTAINTIES AND CONFIDENCE LEVELS

Identi-	Contributing factor	Estimated uncertainty	Assigned con-
fying	•	value	fidence level;
number,			number of stan-
n			dard deviations
1	Fuel assembly power	4 Percent	2
2	Heat-transfer coefficient	15 Percent	
3	Temperature sensing	100 <sup>o</sup> R (55. 5 <sup>o</sup> K)	
4	Power adjustment	at outlet 50 <sup>°</sup> R (27.8 <sup>°</sup> K) at outlet	
5	Flow passage width	0.002 in. (0.0508 mm)	
6	Stage power	3 Percent	
7	Orifice mismatch	5 Percent	3
8	Upper plenum pressure	3 Percent	2
9	Cylinder power	3 Percent	2
10	Fuel loading	3 Percent	2

TABLE 9. - RANGE OF VARIABLES STUDIED FOR CONTROL SYSTEM
WATER CHEMISTRY EXPERIMENTS

Variable		Type of e	xperiment
	Flask	Autoclave	Loop
Materials	347 st	ainless stee	316 stainless steel; el; Zircaloy-2; aloy-niobium
Pretest <sup>a</sup> solution pH	1 to 7	3.4 to 5.9	3
Material surface temperature, <sup>O</sup> R; <sup>O</sup> K	675; 375	710; 394 760; 422 810; 450 860; 478	830 (461)
Heat flux, Btu/(hr)(ft $^2$ ); J/(hr)(m $^2$ )	0	0	75 000; 8.52×10 <sup>8</sup>
Solution velocity, ft/sec; m/sec	0	0	5 to 30 (1.52 to 9.15)
Cadmium concentration, (mg Cd)/cm <sup>3</sup>	4 160	4.5	4
Test duration, hr	100	100 500	$93\frac{1}{2}$
System pressure, psia; N/cm <sup>2</sup> abs	15; 10.3	600; 414	600; 414

 $<sup>^{\</sup>mathbf{a}}$ During the course of the experiments, no attempt was made to maintain the solution pH at its initial value.

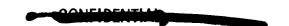


TABLE 10. - TYPICAL METHODS OF REACTOR

CONTROL WITH PUSH-PULL CONTROL RODS

Case	Number of axial fuel zones	Control rod programming
1	1	Single bank motion; all rods withdrawn together
2	2	Single bank motion; all rods withdrawn together
3	1	Two-bank motion; outer bank out, inner bank partly in- serted at beginning of life

TABLE 11. - SHIFT IN POWER WITH DRUM ROTATION

Cell location	Relative	e power		age shift m -
	Drums in	Drums out	In to out	Out to in
Center Peripheral	1. 56 <b>7</b> . 520	1.346 .751	-14.1 44.5	16.4 -30.8

TABLE 12. - AVERAGE HEATING
RATES IN WATER SYSTEM

Material	Source	Average heat-
		ing rate, W/cm <sup>3</sup>
Water	Gamma	77.8
	Neutron	100.0
Aluminum	Gamma	159.8
	Beta	3.2





TABLE 13. - SOURCES OF HEAT PERTINENT TO

## WATER FLOW SYSTEM

Location	Sources of heat	Heati	Heating value
		Btu/sec	J/sec
Aluminum Pressure tube (121) Flow divider (121) Total	Gamma plus beta Gamma plus beta	2 034 2 400 4 434	2. 148×10 <sup>6</sup> 2. 534×10 <sup>6</sup> 4. 682×10 <sup>6</sup>
Water Outside flow divider	Gamma Neutron	8 916 16 830	9.414×10 <sup>6</sup> 1.777×10 <sup>7</sup>
Inside flow divider	Gamma Neutron	3 407	$3.597\times10^{6}$ $6.791\times10^{6}$
Total inside Total		9 839	$\frac{1.039\times10^{7}}{3.7573\times10^{7}}$
Side reflector Beryllium Water Total	Gamma Gamma plus neutron	5 713 850 6 563	$6.022\times10^{6} \\ 8.97\times10^{5} \\ 6.930\times10^{6}$
Miscellaneous Top reflector Heat exchanger Hot fuel assembly Total	Gamma Gamma plus neutron Conduction plus radiation	492 623 3 220 4 335	$ 5.19 \times 10^{5} 6.58 \times 10^{5} 3.400 \times 10^{6} 4.577 \times 10^{6} $
Total heat sources		50 917	5. 376×10 <sup>7</sup>

## TABLE 14. - RADIAL DISTRIBUTION OF

HEAT TRANSFERRED TO AND

## GENERATED IN WATER

	Value	relative	to core	average	1.35	1.33	1.29	1.19	1.06	. 89	.75	1.00
	Value	relative	to center	cell	1.00	66 .	. 95	. 88	. 78	99.	. 56	0.74
	Heat load per cell	1/800	7 ac/		$5.090 \times 10^{5}$	5.019	4.841	4.481	3.976	3,358	2.839	356.37 3.7628×10 <sup>5</sup>
	Heat los	Btn /eoc	nae/mid		482.1	475.3	458.5	424.4	376.6	318.0	268.9	356.37
	Number	of cells			1	9	12	18	24	30	30	a <sub>121</sub>
,	Ring				1 (center)	7	အ	4	2	9	7	Average

<sup>a</sup>Total



## TABLE 15. - TYPICAL COMPARISON OF PREDICTED

## AND MEASURED PRESSURE LOSSES FOR

## TWMR WATER FLOW TEST

## (a) Orifice pressure losses

Transmitter	Ring	Pressu	ıre loss, psi (	N/cm <sup>2</sup> )
		Predicted <sup>a</sup>	Correctedb	Measured
25	1	0.80 (0.55)	0.80 (0.55)	0.65 (0.45)
26	2			1.03 (.71)
27	2			37 ( 26)
28	2			24 ( 17)
29	3			. 41 (. 28)
30	3			07 ( 05)
31	3	*	*	. 39 (. 27)
32	4	5.91 (4.07)	4. 90 (3. 38)	3. 24 (2. 23)
33	4	5.91 (4.07)	4. 90 (3. 38)	2.27 (1.57)
34	4	5.91 (4.07)	4. 90 (3. 38)	2.29 (1.58)
35	5	7. 12 (4. 91)	6.31 (4.35)	2, 48 (1, 71)
36	5	}		3.29 (2.27)
37	5			4.61 (3.18)
38	5			3. 25 (2. 24)
39	5			3. 05 (2. 10)
40	5	•	₩	2.60 (1.79)
41	6	10.96 (7.56)	7. 88 (5. 43)	9. 03 (6. 23)
42	6		1 1	6.63 (4.57)
43	6			8.06 (5.56)
44	6		•	6.86 (4.73)
45	7	23. 85 (16. 44)	14. 12 (9.74)	11. 31 (7. 80)
46	7			14. 41 (9. 94)
47	7			8.69 (5.99)
48	7		<b>Y</b>	14. 48 (9. 98)

<sup>&</sup>lt;sup>a</sup>Based on ideal orifice dimensions.

 $<sup>^{\</sup>mbox{\scriptsize b}}\mbox{Corrected}$  for leakage based on nominal orifice dimension.

TABLE 15. - Continued. TYPICAL COMPARISON OF PREDICTED AND MEASURED PRESSURE LOSSES FOR TWMR WATE: FLOW TEST

(b) Inlet plenu n losses

Transmitter	From inlet	Pressure loss,	psi $(N/cm^2)$
	to ring	Predicted	Measured
49	6 to 7	c4.75 (3.28)	7. 84 (5. 41)
20	5 to 6	8. 73 (6. 02)	6.67 (4.60)
51	5 to 6	9.78 (6.74)	7.91 (5.45)
52	6 to 7	<sup>c</sup> 4, 75 (3, 28)	7.26 (5.01)
53	3 to 4	8. 82 (6. 08)	6.71 (4.63)
54	3 to 4	8, 82 (6, 08)	6.83 (4.71)
22	3 to 4	8 82 (6.08)	6. 96 (4. 80)
26		88 (6.	96 (4.
22	1 to 2	69	90
58	4 to 5	8.73 (6.02)	6.92 (6.34)
59	2 to 3	9.88 (6.81)	6.99 (4.82)
09	1 to 2	8.69 (5.99)	7.06 (4.87)
61	3 to 4	8. 82 (6. 08)	6.96 (4.80)
62	6 to 7	9. 16 (6. 32)	7.38 (5.09)
63	3 to 4	8.82 (6.08)	6.98 (4.81)
64	3 to 4	8, 82 (6, 08)	7.11 (4.90)
65	5 to 6	8. 43 (5. 81)	6.99 (4.82)
99	6 to 7	<sup>c</sup> 4.75 (3.28)	7.77 (5.36)
6			

<sup>a</sup>Predicted lower value due to missing element in

# TABLE 15. - Concluded. TYPICAL COMPARISON OF PREDICTED AND MEASURED PRESSURE LOSSES

## (c) Miscellaneous losses

FOR TWMR WATER FLOW TEST

Transmitter	Location	Pressure loss, psi (N/cm <sup>2</sup> )	psi $(N/cm^2)$
		Predicted	Measured
67	Upper reflector	9, 42 (6, 50)	7. 60 (5. 24)
89		11.86 (8.18)	8.91 (6.14)
69		14.34 (9.89)	7.79 (5.37)
70	-	12.53 (8.64)	9.07 (6.25)
7.1	Support plate	16.85 (11.62)	16, 49 (11, 37)
72	,	16. 58 (11. 43)	15, 18 (10, 47)
73		13.65 (9.41)	16. 75 (11. 55)
74	-	14.93 (10.29)	15. 27 (10. 53)
75	From inlet to	36, 54 (25, 19)	32, 64 (22, 51)
	heat exchanger		
76	Across heat	30. 56 (21.07)	32.05 (22.10)
	exchanger		
77	Inlet nozzle	2.41 (1.66)	2.35 (1.62)
78	Outlet nozzle	5.27 (3.63)	3.92 (2.70)
Ö	تارىس تارىس	15.9 (10.48)	15 1 (10 41)
<b>6</b>	TION TRUE	_	
08 —	Total reactor	(27.76) (27.73)	03.0 (41.33)
81	Total system	a <sub>84.2</sub> (58.06)	80.0 (55.16)

<sup>d</sup>The predicted values for overall pressure losses appear to be 5 to 10 percent conservative based on the measured values.



TABLE 16. - CHARACTERISTICS<sup>a</sup> OF REFERENCE-DESIGN CRYOGENIC HYDROGEN-WATER HEAT EXCHANGER

Characteristic	U.S. customary units	SI units
Water flow rate, lb/sec; kg/sec	1040	472
Cryogenic hydrogen flow rate, lb/sec; kg/sec	92.7	42.1
Number of tubes	720	
Inside diameter of tubes, in.; mm	0. 305	7.75
Outside diameter of tubes, in.; mm	0.375	9. 53
Spacing of tubes, centerline to center-	0. 475	12.1
line, in.; mm		
Inlet water temperature, OR; OK	699	388
Outlet water temperature, OR; OK	654	363
Inlet hydrogen temperature, OR; OK	170	94. 5
Outlet hydrogen temperature, OR; OK	302	168
Minimum water side tube temperature,  OR: OK	55 <b>7</b>	310
Heat-transfer rate, Btu/sec; J/sec	5.09×10 <sup>4</sup>	5.37×10 <sup>7</sup>
Margin from freezing, R <sup>o</sup> ; K <sup>o</sup>	65	36
Length of heat-transfer region, in.; cm	33	83.8

<sup>&</sup>lt;sup>a</sup>At full power conditions.



TABLE 17. - POSSIBLE VARIATION IN HEAT-EXCHANGER PARAMETERS DURING STARTUP

Case							Va	riabl	es								Results	s of icing a	alysis		
		Γrar ime				Hyd	lroge eratu			te	Wa:		e		Icing begins	Icing ends	Total icing	Maximum U/U <sub>crit</sub>	Maximum U/U <sub>crit</sub>	Maxi stea	
	w	х	Y	z					Tir	ne					at time, sec	at time, sec	time, sec	occurs at time,	0.10	state thick	
						0		z	(	)	:	x		Z	•			sec		in,	mm
						H	eat-	excha	nger i	inlet	temp	eratu	re								
				i	o <sub>R</sub>	° <b>K</b>	OR	oĸ	OR	o <sub>K</sub>	o <sub>R</sub>	o <sub>K</sub>	o <sub>R</sub>	°K							
1	10	15	0	30	50	27.8	180	100	680	378	650	361	700	388	5. 0	20. 5	a <sub>15.5</sub>	15	1. 193	0.013	0. 330
2	5	15		30	1					1					5. 0	19.5	14.5		1.141	. 007	. 170
3	15	15		30											5.0	22.0	17.0		1.282	. 022	. 559
4	0	15		30			ŀ								6.5	18, 5	12.0	*	1. 107	. 005	. 127
5	20	30		60											10.0	41.0	29.0	29	1. 193	. 013	. 330
6	40	60	🕴	120											19.5	82.5	63.0	59. 5	1. 194	. 013	. 330
7	5	15	10	30											2.5	22.5	20.0	10.0	1.924	. 039	. 991
8	5	15	20												2.5	26.0	23.5	10.5	1.959	. 040	1, 02
9	0	15	10								1	1			2.5	22.0	19.5	10.0	1.862	. 037	. 940
10	10	15	0	7							660	367			5. 5	19. 5	14.0	12.5	1.133	<.001	. 025
11	20	30	0	60											10. 5	38. 5	28.0	25.0	1.133	<. 001	. 025
12	40	60	0	120											21.0	78.0	57.0	49.5	1. 133	<. 001	. 025
13	5	15	10	30							<b>Y</b>	1			2.5	22.0	19.5	10.0	1.868	. 037	. 940
14	10	15	0	30							670	372			6.0	18.0	12.0	10.5	1.091	<. 001	. 025
15	20	30		60											11.5	36.0	24.5	21.0	1.091	<.001	. 025
16	40	60		120	*	*									23.0	72.0	49.0	42.0	1.091	<. 001	. 025
17	10	15		30	80	44. 5					650	361			6.5	19.0	12.5	15.0	1.134	. 007	. 178
18	20	30		60	80	44. 5					650	361			13.0	38.5	25. 5	30.0	1.134	. 007	. 178
19	40	60		120	80	44. 5			1	🕴	700	361			25.5	77.5	52.0	60,0	1. 134	. 007	. 178
20	10	15	1	30	50	27.8	.   1	₹	700	388	700	388	1	7			0	10.0	. 970		

<sup>&</sup>lt;sup>a</sup>See figs. 94 to 96.

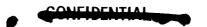




TABLE 18. - MODERATOR SYSTEM WATER CHEMISTRY

EXPERIMENTS RANGE OF VARIABLES STUDIED

Variable	Туре	of experiment
	Autoclave	Loop
Material	6061-T6 alı	ıminum
Pretest material treatment		autoclave and ''Alumilite Hard-
Pretest <sup>a</sup> solution pH Material surface temperature, <sup>o</sup> R; <sup>o</sup> K	5 660; 367	5 760; <b>422</b>
Heat flux, Btu/(hr)(ft <sup>2</sup> ); J/(hr)(m <sup>2</sup> )	760; 422 0	48 500; 5. 51×10 <sup>8</sup> 360 000; 4. 09×10 <sup>9</sup>
Water velocity, ft/sec; m/sec	0	2; 0.61
Test duration, hr	1400	15; 4.57 10 351

<sup>&</sup>lt;sup>a</sup>The solution pH was not adjusted during the course of the experiments.



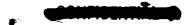


## TABLE 19. - NOZZLE DESIGN CASES

(a) U.S. Customary Units

Case	Main flow,	Nozzle cl		No	ozzle coo	lant tubes		Coolant	Coolant	l .	rate,	Maxi-	Wall
	percent	Collan	1011	Inlet con	ndition	Exit con	dition	pressure drop,	temper- ature	16/	sec -	mum wall	temper-
		Temper- ature, <sup>O</sup> R	Pres- sure, psi	Temper- ature, <sup>O</sup> R	Pres- sure, psi	Temper- ature, OR	Pres- sure, psi	ΔP <sub>c</sub> ,	rise, <sup>ΔT</sup> c,  R <sup>O</sup>	Cool- ant	Hot gas	temper- ature, OR	drop, R <sup>0</sup>
8B	100	4500	600	51.0	1203	170.2	1070.7	132.3	119.2	92.7	90.3	1865	665
11				1	1203	186.2	1069.9	133. 1	136.2			1865	665
13	1				1203	171.8	1071.7	131.3	120.8			1650	500
19	7	<b>Y</b>	1	<b>, ,</b>	1500	179.0	1390	110	128.0	🕴	₹	1830	700
101	60	4460	360	46.0	678.8	171.9	591.8	87.01	125.9	55.6	54.2	1692	500
200	60	3460	312	44.2	627.5	125. 09	571.5	55, 95	80.89	55.6	54.2	1330	378
201	60	3460	312	44.2	627.5	148.0	586.6	40.9	103.8	43.2	54.1	1360	385
202	60	3460	312	44.2	480	121.9	399.4	80.6	77.7	55.6	54.2	1313	399
302	37	4460	219.4	44.8	454.6	186.7	400. 59	54.0	141.89	33. 9	33	1540	330
500		3460	196.5	42.1	340.6	131.3	294.9	45.68	89.2	1	1	1200	300
501		3460	196.5	42.1	454.6	135.3	422.4	32.2	93.2			1194	293
502	٧	3460	196.5	42.1	400.0	133.3	362.9	37.1	91.2	<b>*</b>	¥	1186	323
600	21	2460	94.46	42.5	189	89.2	175. 1	14.6	46.6	19.47	18.88	790	165
700	21	3460	112.9	42.9	226	146.0	199.5	26.5	103.1	19.47	18. 88	1080	210

Case	Main	Nozzle ci		No	ozzle coo	olant tubes		Coolant	Coolant	į.	rate,	Maxi-	Wall
	flow,	condit	ion T	Inlet co	ndition	Exit cor	dition	pressure drop,	temper- ature	kg/	sec	mum wall	temper-
	percent	Temper- ature, <sup>O</sup> K	Pres- sure, N/cm <sup>2</sup>	Temper- ature, <sup>O</sup> K	Pres- sure, N/cm <sup>2</sup>	Temper- ature, <sup>O</sup> K	Pres- sure, N/cm <sup>2</sup>	ΔP <sub>c</sub> , N/cm <sup>2</sup>	rise, <sup>ΔT</sup> <sub>c</sub> ,  K <sup>o</sup>	Cool- ant	Hot gas	temper- ature, OK	ature drop, <sup>O</sup> K
8B	100	2500	414	28.4	830	94.6	739	91.3	66.3	42.1	41.0	1037	370
11	1				830	103.5	737	91.8	75.7	1	1	1037	370
13					830	95.4	740	90.5	67.1			917	278
19	1	1	🔻	₹	1032	99.5	958	75.8	71.1	¥	\ \	1018	389
101	60	2480	248	25.6	468	95. 5	408	60	70.0	25.2	24.6	940	278
200	60	1920	215	24.6	433	69.6	394	38.6	44. 9	25.2	1	740	210
201	60	1920	215	24.6	433	82.2	404	28.2	57.6	19.6		755	214
202	60	1920	215	24.6	331	67.7	275	55. 5	43.2	25.2	Ť	730	222
302	37	2480	151	24.9	314	103.8	276	37.2	78.8	15.4	15	856	183
500	1 .	1920	135	23.4	235	67.6	204	31.5	49.6	1	ı	666	167
501		1920	135	23.4	314	75.2	292	22.2	51.9			664	163
5 <b>02</b>	Ŧ	1920	135	23.4	276	74.1	250	25.6	50.6		*	659	179
600	21	1370	65. 1	23.6	130	49.6	121	10.1	25. 9	8.85	8. 57	439	91.6
700	21	1920	77.8	23.8	156	81.1	138	18.3	57.3	8. 85	8, 57	600	117

TABLE 20. - STRESSES AT OUTER FIBER OF TUBE WALL

(a) U.S. Customary Units

Type of stress	Wal	l thickness, i	in.
	0. 010	0.008	0.006
		Stress, psi	
Bending, $\sigma_{\mathbf{B}}$	18.3 ×10 <sup>3</sup>	14. 10 ×10 <sup>3</sup>	10. 52×10 <sup>3</sup>
Thermal, $\sigma_{\theta B}$	92. 2	79.5	66.5
Hoop, $\sigma_{\Delta P}$	3.63	4.53	6.03
Membrane, σ <sub>U</sub>	1.40	1.08	. 48
Total, otot	72	62	57
Total with no restraint from	89	75	60
backup shell, $\sigma_B = \sigma_U = 0$			

Type of stress	Wall	thickness, n	nm
	0.254	0.2032	0.1524
	St	ress, N/cm <sup>2</sup>	
Bending, σ <sub>B</sub>	12.6 ×10 <sup>3</sup>	9.72 ×10 <sup>3</sup>	7.25×10 <sup>3</sup>
Thermal, $\sigma_{\theta \mathbf{B}}$	63.5	54.8	45.8
Hoop, σ <sub>ΔP</sub>	2.50	3, 12	4.15
Membrane, σ <sub>U</sub>	. 965	.745	. 33
Total, otot	49.6	42.7	39. 3
Total with no restraint from	61.4	51.7	41.4
backup shell, $\sigma_{B} = \sigma_{U} = 0$			



## TABLE 21. - SUMMARY OF FLANGE DESIGN CASES

(a) U.S. Customary Units

Case	Slot width,	Slot lo- cation,	Weight flow per unit	Coolant   Coolant   Maximum temperature   pressure   temper-   difference, R <sup>O</sup>				temper-	
:	in.	in.	area, lb/(sec)(in. <sup>2</sup> )	drop, ΔP <sub>c</sub> , psi	ature rise, $\Delta T_{c}$ , $R^{O}$	Inner side	Outer side	Circum- ferential	ature of flange, <sup>O</sup> R
1	0. 10	1. 15	2	261	250	556	233	118.8	865.1
2	. 20	1.15	1	44	250	547.6	217	116.8	873
3		1.05		39	245	481	269	115.9	798
4		. 95		39	238	417	328.7	115, 1	724.5
5	<b>*</b>	.75	<b>*</b>	42	227.8	302	476	114	589

Case	Slot width,	Slot lo- cation,	Weight flow per unit	Coolant pressure	Coolant temper-	Maximum temperatur difference, K <sup>O</sup>		-	temper-	
	mm	cm	area, g/(sec)(cm <sup>2</sup> )	drop, ΔP <sub>c</sub> , N/cm <sup>2</sup>	ature rise, $\Delta T_{c}$ ,	Inner side	Outer side	Circum- ferential	ature of flange, <sup>O</sup> K	
					K <sup>o</sup>					
1	2.54	2. 92	179	180	139	308	129	66	481	
2	5.08	2.92	89	30.4	139	304	120	64.8	485	
3		2.66		26.9	136	267	149	64.4	443	
4		2.42		26.9	132	232	182	64.0	402	
5	Y	1.90	Y	29.0	126	168	264	63.4	327	



## TABLE 22. - BACKUP SHELL STRESS AND DEFORMATION (SEE FIG. 118)

(a) U.S. Customary Units

Case	Case Temper- ature, OR		Axial stress, psi		Hoop stress, psi		Moment, inlb/in.		Force, lb/in.			Displacement, in.	
		CIOII	Inner	Outer	Inner	Outer	Axial	Ноор	Vertical	Horizontal	Ноор	Vertical	Horizontal
1		FS1	58 900	-28 500	17 100	-8 300	1 822	528	7 594	1 543	2 202	0	0
		FS2	74 800	-43 900	29 100	-4 080	2 473	692	6 160	-4 897	6 262	. 0032	. 0061
1		SS1	-16 100	23 600	3 750	15 100	-6 870	-1 962	5 001	-4 031	13 600	. 0032	. 0061
		SS2	-1 190	-1 190	11 100	10 600	0	1	-200	0	1 629	0028	. 0037
	!	PS1	0	0	-27 600	-27 600	0	0	0	0	-9 643	.0011	0196
		PS2	-41 500	41 500	-3 550	20 700	-847	-248	0	1 051	3 003	. 0032	. 0061
2	530	FS1	171 300	-141 000	-46 600	-137 100	6 506	1 887	7 594	5 292	-45 920	0	0
		FS2	4 610	22 600	41 200	48 500	-376	-152	6 160	2 917	22 440	. 0405	. 0850
		SS1	-35 700	42 400	-115 600	-93 500	-13 500	-3 828	5 001	1 661	-150 500	. 0405	. 0850
		SS2	-1 194	-1 194	11 200	10 600	0	1	200	0	1 633	0100	0151
		PS1	0	0	-27 500	-27 500	0	0	0	0	9 629	. 0405	0196
		PS2	-227 800	227 800	52 700	185 600	-4 650	-1 357	0	4 836	41 700	. 0406	. 0850
3	970	FS1	-740	31 100	-320	8 920	-664	- 192	-7594	-221	2 150	0	0
		FS2	-44 400	-68 200	44 900	78 600	-2 350	-702	6 160	-999	30 900	. 0007	. 02 52
		SS1	-34 100	40 900	-101 500	-80 100	-13 000	-3 690	5 001	974	-130 800	. 0007	. 02 52
		SS2	-1 190	-1 190	11 200	10 600	0	1	200	0	1 633	1556	0471
		PS1	0	0	-27 700	-27 700	0	0	0	0	-9 681	0008	0197
		PS2	-97 800	97 800	6 740	63 800	-1 996	-583	0	2 075	12 300	. 0007	. 02 52

Case	Temper- ature, <sup>O</sup> K	Loca- tion	Axial stress, N/cm <sup>2</sup>		Hoop stress, N/cm <sup>2</sup>		Moment, (cm)(N)/cm		Force, N/cm			Displacement, mm	
			Inner	Outer	Inner	Outer	Axial	Ноор	Vertical	Horizontal	Ноор	Vertical	Horizontal
1		FS1	40 600	-19 600	11 800	-5 720	8 100	2 345	13 300	2 700	3 850	0	0
		FS2	51 500	-30 200	20 000	-2 810	11 000	3 080	10 800	-8 560	10 850	. 0813	. 155
		SS1	-11 100	16 300	2 580	10 400	-30 600	-8 730	8 750	-7 050	23 800	. 0813	. 155
		SS2	-820	-820	7 6 5 0	7 300	0	4	-350	0	2 850	0711	. 094
		PS1	0	0	-19 000	-19 000	0	0	0	0	-16 880	. 028	498
		PS2	-28 600	28 600	-2 440	14 280	-3 770	-1 100	0	1 840	5 2 5 0	. 0813	. 155
2	294	FS1	118 000	-97 300	-32 100	-94 500	28 900	8 390	13 300	9 260	-80 500	0	0
		FS2	3 180	15 600	28 400	33 400	-1 670	-676	10 800	5 100	39 300	1.03	2.16
		SS1	-24 600	29 200	-79 600	-64 500	-60 000	-17 000	8 750	2 910	-264 000	1.03	2.16
		SS2	-824	-824	7 720	7 310	0	4	350	0	2 860	254	384
		PS1	0	0	-19 000	-19 000	0	0	0	0	16 850	1.03	498
		PS2	-157 000	157 000	36 400	128 000	-20 600	-6 030	0	8 4 5 0	73 000	1.03	2.16
3	539	FS1	-510	21 400	-220	6 150	-2 950	-854	13 300	-387	3 760	0	0
		FS2	-30 600	-47 000	31 000	54 200	-10 450	-3 120	10 800	-1 750	54 100	.0178	. 64
		SS1	-23 500	28 200	-70 000	-55 200	-57 800	-16 400	8 750	1 705	-228 700	.0178	. 64
		SS2	-820	-820	7 720	7 310	0	4	350	0	2 860	-3.95	-1.20
		PS1	0	0	-19 100	-19 100	0	0	0	0	-16 920	0203	5
		PS2	-67 400	67 400	4 6 5 0	44 000	-8 870	-2 590	0	3 630	21 550	.0178	. 64



TABLE 23. - THERMAL STRESSES FOR GRADIENT

## ACROSS WALL

Type of	Location											
stress	FS1	FS2	SS1									
	Stress, psi (N/cm²)											
Inner axial	135 700 (93 400)	102 000 (70 400)	328 000 (226 000)									
Outer axial	-68 600 (-47 300)	-46 200 (-31 200)	-78 700 (-54 200)									
Inner hoop	135 700 (93 400)	102 000 (70 400)	328 000 (226 000)									
Outer hoop	-68 600 (-47 300)	-46 200 (-31 200)	-78 700 (-54 200)									

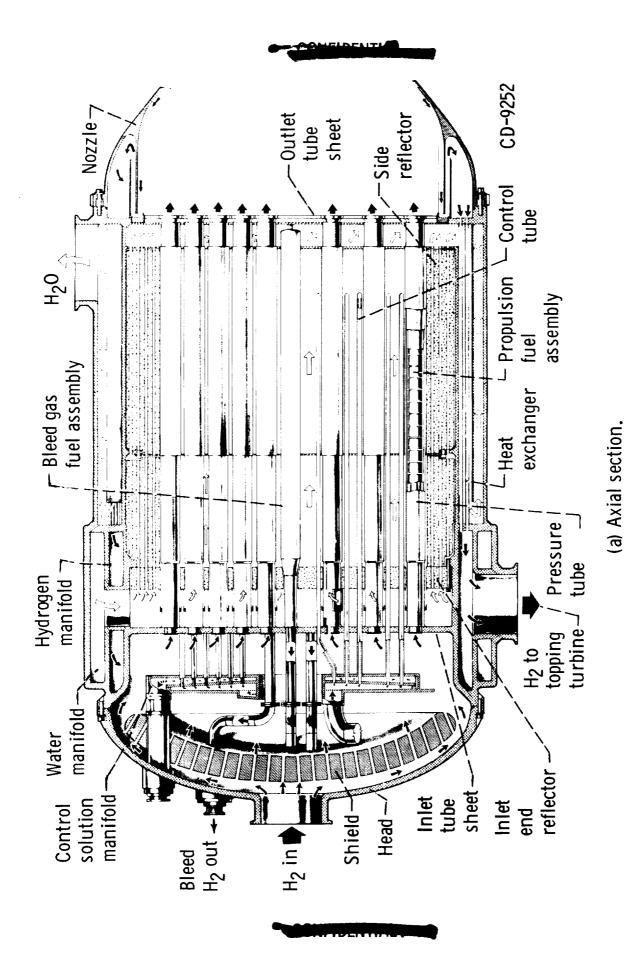
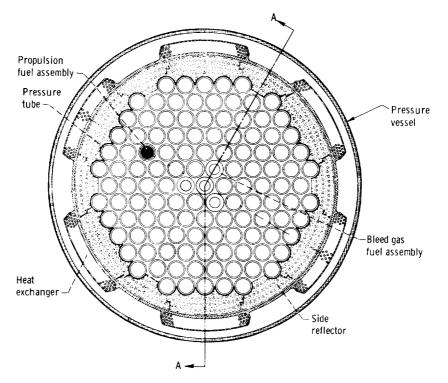


Figure 1. - Reactor assembly.

## - CONFIDENTIAL



(b) Cross section.

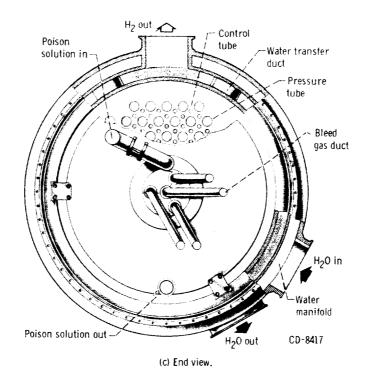


Figure 1. - Concluded.



16, 17

11

Section through core

12 <sup>j</sup> 13

15

16, 17

18

21

22

20

Section through

fuel assemblies

31

29

-23

CD-9242

33

## Nomenclature

- 1. Fuel assembly spacing
- 2. Center fuel assembly
- Ring 2 of fuel assemblies (arranged in hexagonal rings numbered consecutively from ring 1 located at reactor center)
- 4. Ring 3 of fuel assemblies
- 5. Side reflector
- 6. Reactor pressure-vessel head
- 7. Inlet hydrogen plenum
- 8. Reactor pressure vessel
- 9. Heat-exchanger tubes
- 10. Heat-exchanger, water side
- 11. Internal primary shield
- 12. Inlet tube sheet
- 13. Inlet water plenum
- 14. Inlet end reflector
- 15. Flow divider tube
- 16. Flow divider passage (description of passage only)
- 17. Pressure tube cooling water (description of water in passage)
- 18. Core water region
- 19. Orifice hole
- 20. Outlet water baffle
- 21. Outlet water plenum
- 22. Outlet tube sheet
- 23. Outlet tube sheet insulation
- 24. Nozzle chamber wall
- 25. Inlet reflector insert
- Inlet fuel stage 1 (numbered consecutively from 1 for first fuel stage at inlet end)
- 27. Pressure tube
- 28. Outlet fuel stage
- 29. Control tube
- 30. Inlet water pipe
- 31. Water manifold
- 32. Outlet water pipe
- 33. Nozzle chamber

Figure 2. - Reactor component nomenclature.

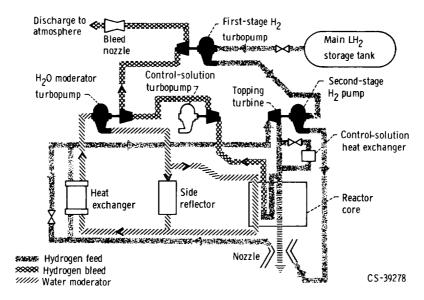
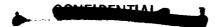


Figure 3. - Schematic drawing of hydrogen and water flow systems.





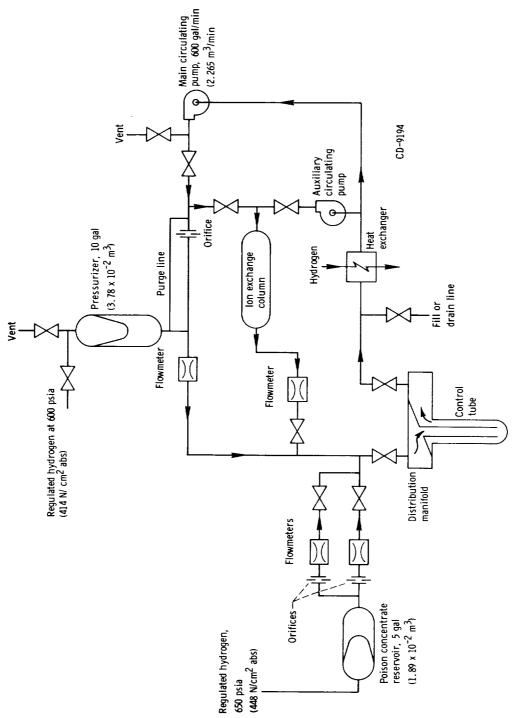
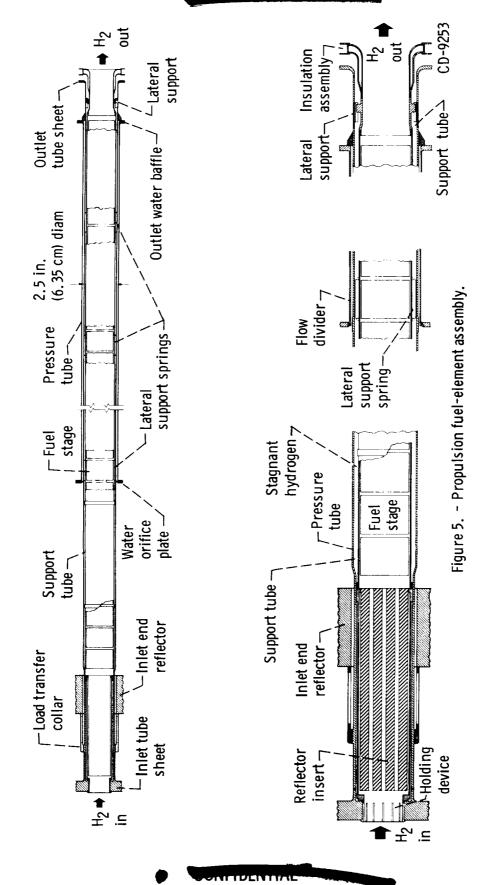
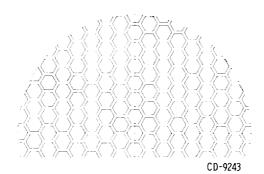
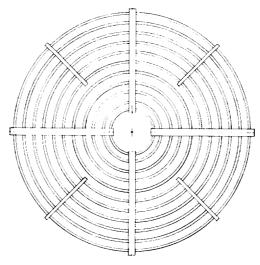


Figure 4. - Control system flow diagram.

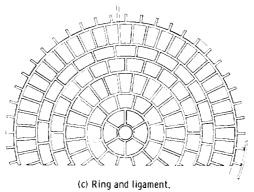




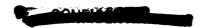
(a) Honeycomb.



(b) Concentric cylinder.



to, iting and tigament.



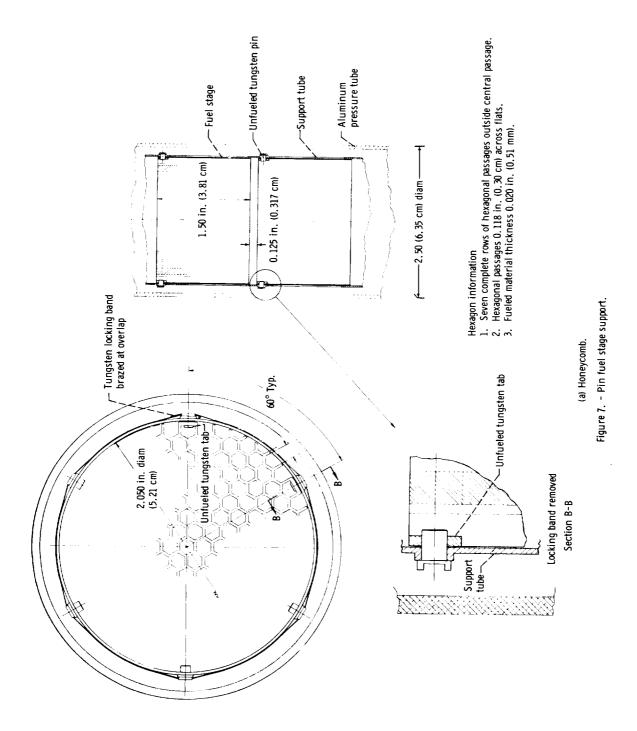


Figure 7. - Concluded.



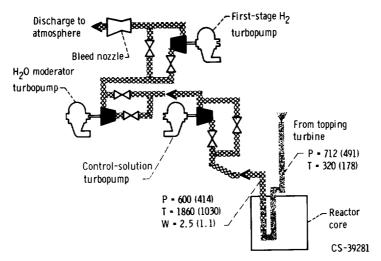


Figure 10. – Hydrogen bleed system schematic diagram. Pressure, P, psia (N/cm $^2$  abs); temperature, T,  $^\circ$ R ( $^\circ$ K); flow rate, W, Ib/sec (kg/sec).

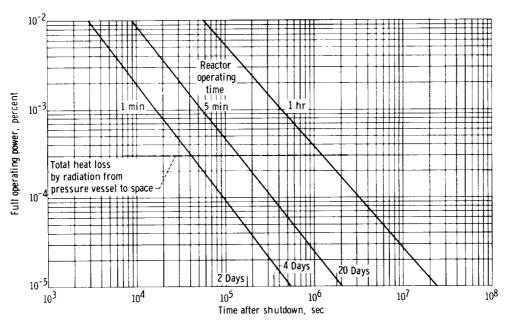


Figure 11. - Total fission product power as function of time after shutdown. Vessel temperature,  $660^{\circ}$  R ( $367^{\circ}$  K); vessel emissivity, 0. 90.



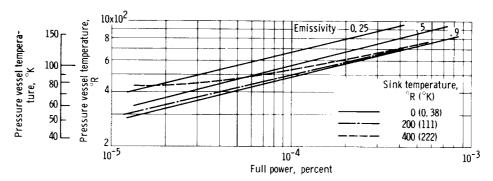


Figure 12. - Steady-state thermal radiation to space from reactor pressure vessel at various temperatures.

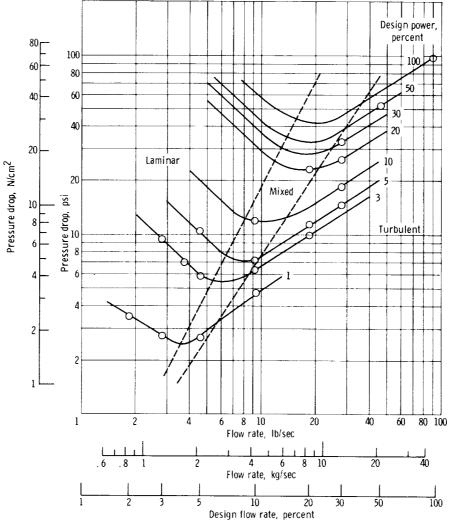


Figure 13. - Reactor core pressure drop. Inlet temperature, 322° R (179° K).





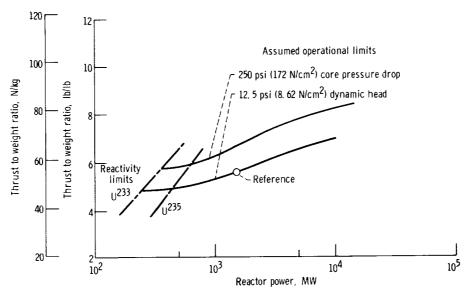
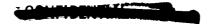
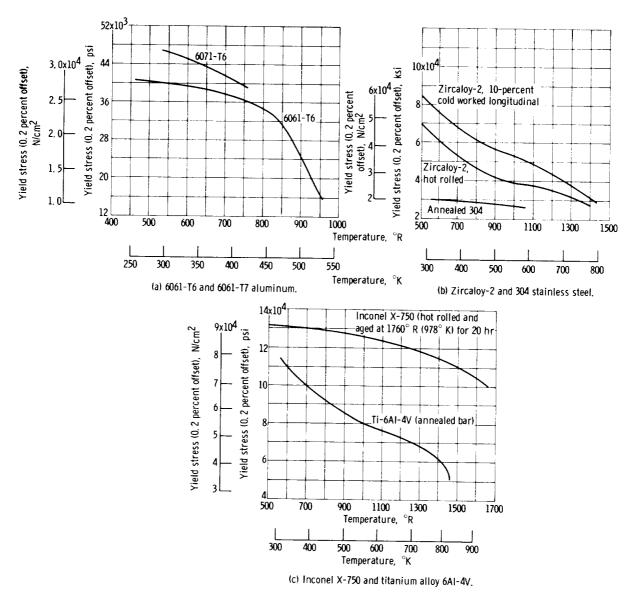


Figure 14. - Effect of power level and operational limits on thrust-weight ratios.

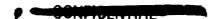






CONTRA

Figure 15. - Effect of temperature on yield stress.



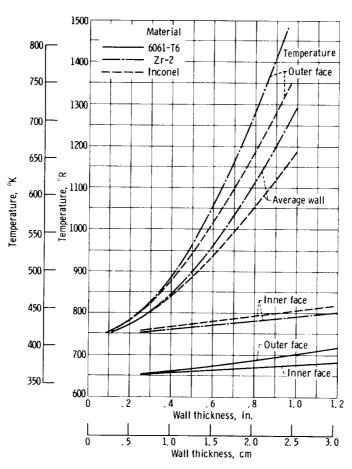
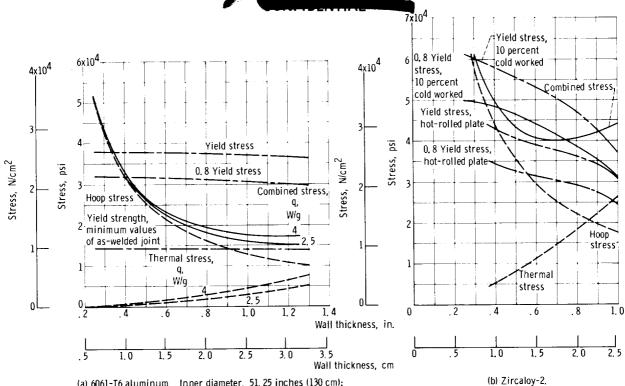


Figure 16. - Wall temperatures of pressure vessels of various materials and thicknesses. Internal heat generation rate, 2. 65 watts per gram; inner face in contact with coolant.



(a) 6061-T6 aluminum. Inner diameter, 51, 25 inches (130 cm); pressure load, 505 psi (348 N/cm²); internal heat generation rate, 2, 65 and 4, 00 watts per gram.

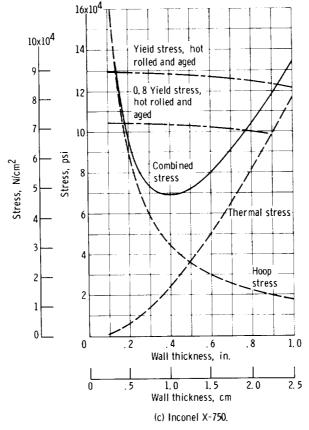


Figure 17. - Stresses of inner face of pressure vessel.

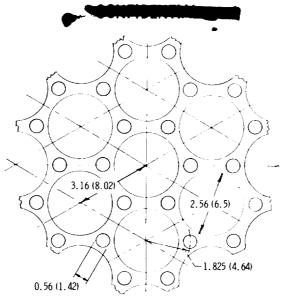


Figure 18. – Hole configuration in beryllium inlet end reflector. (All dimensions are in inches (cm).)

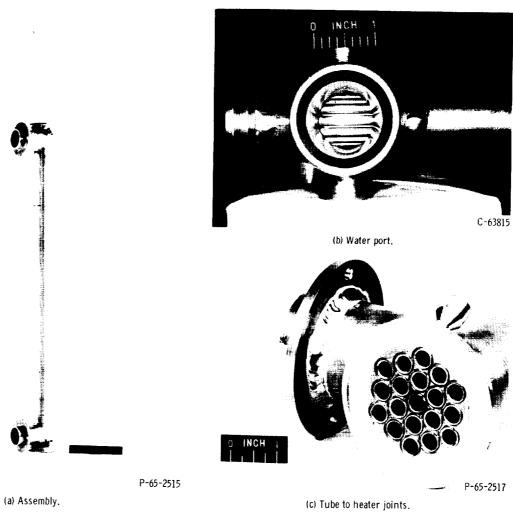


Figure 19. - Test heat exchanger.

147

## CONFIDENTIAL

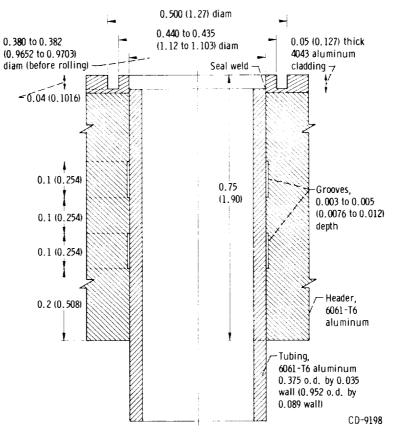


Figure 20. - Rolled tube and header configuration (before welding). (All dimensions are in inches (cm).)

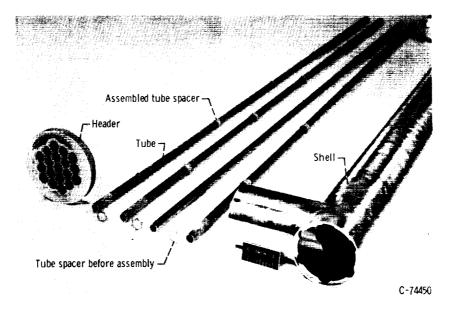


Figure 21. - Test heat exchanger components.

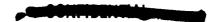




Figure 22. - Test heat exchanger tubes and tube spacers.

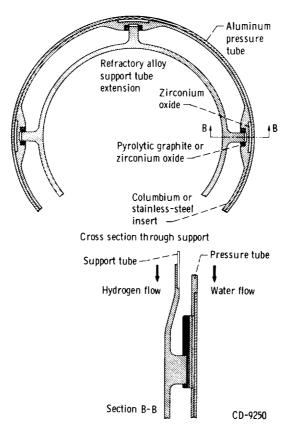
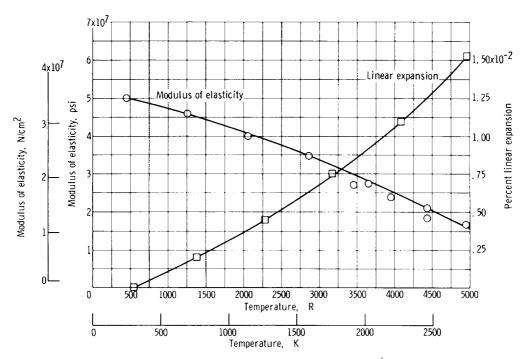
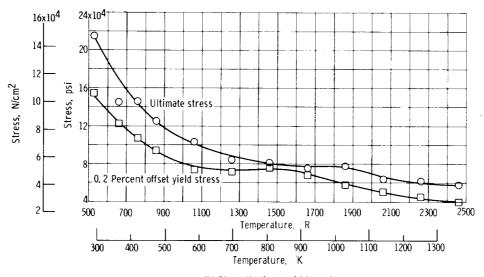


Figure 23. - Reference design hot end fuel assembly support.



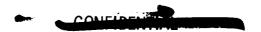
(a) Expansion and modulus of elasticity. Percent linear expansion =  $\{(Length \ at \ temperature) - [Length \ at 536° R (298° K)]/Length \ at 536° R (298° K) \} x 100.$ 

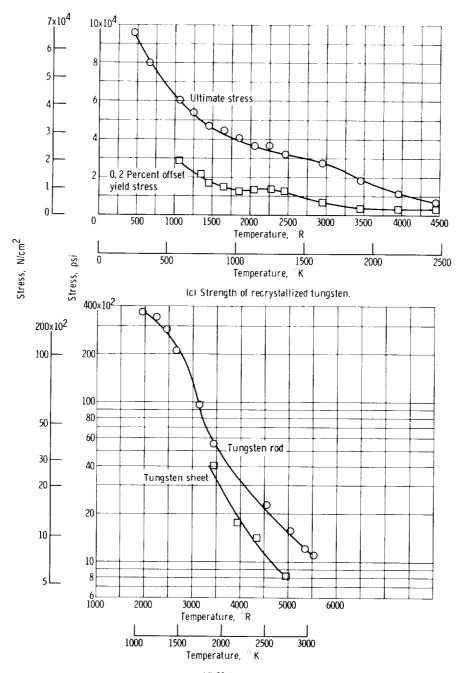


(b) Strength of wrought tungsten.

Figure 24. - Effect of temperature on properties of tungsten.







(d) 20-Hour stress to rupture.

Figure 24. - Concluded.



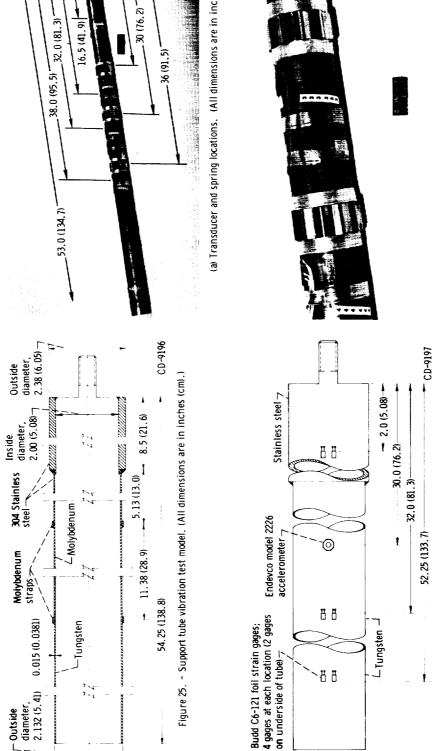


Figure 26. - Transducer locations on partly instrumented support tube model. (All dimensions are in inches  $\{cm\}$ .)

C-65-3407

(b) Closeup of springs and strain gage installation.

Figure 27. - Support tube model.



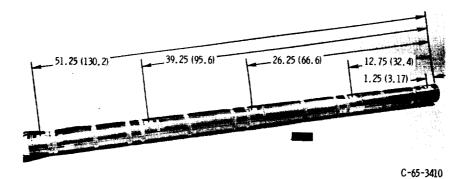


Figure 28. - Pressure tube strain gage locations. (All dimensions are in inches (cm).)

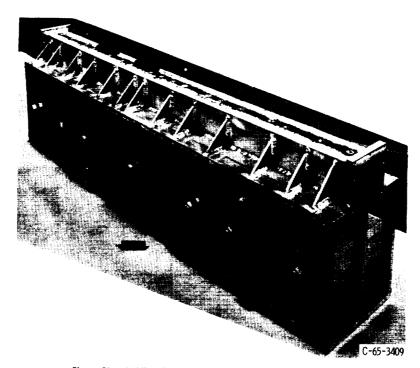
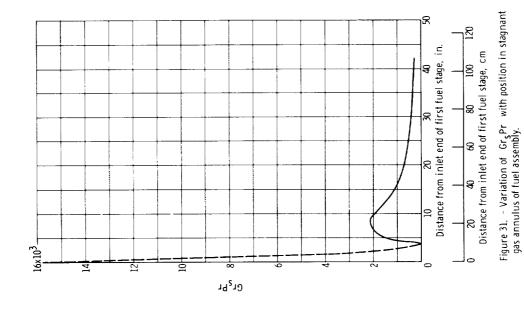
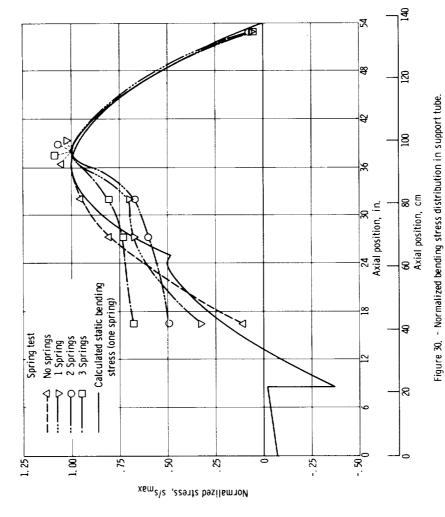


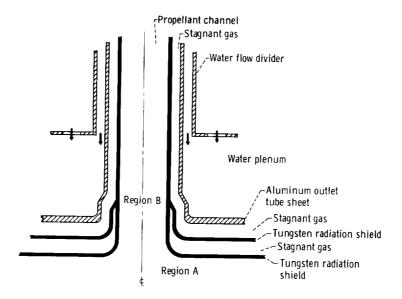
Figure 29. - Holding fixture for vibration tests on fuel assemblies.





CONFIDENTIAL





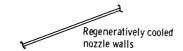


Figure 32. - Schematic diagram of outlet tube sheet region of core.

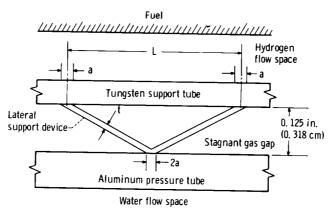
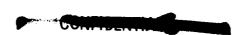


Figure 33. - Schematic representation of generalized V-type lateral support device used in heat-transfer analyses, where  $a = \left[t\sqrt{(L/2)^2 + (0.125)^2}\right]/0.125$  inches  $\left(a = \left[t\sqrt{(L/2)^2 + (0.318)^2}\right]/0.318$  cm), t is thickness of lateral support spacer, and t is characteristic length of spacer.





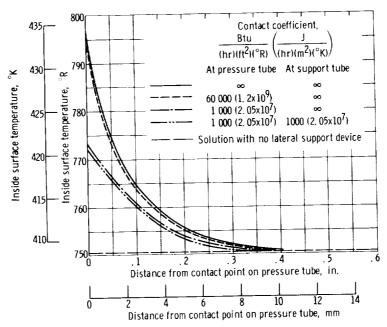


Figure 34. - Effect of contact resistance on aluminum pressure tube temperature. Thickness, 0.007 inch (0.178 mm); characteristic length, 0.600 inch (1.52 mm).

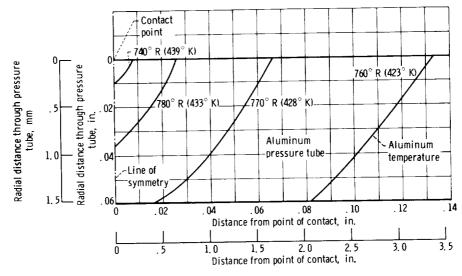
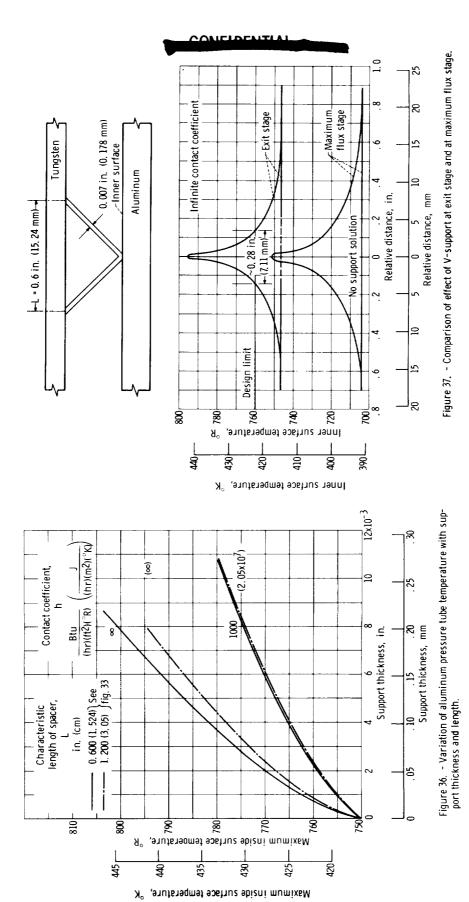


Figure 35. – Typical variation of pressure tube temperature in vicinity of support contact. Infinite contact coefficients, 0.007 inch by 0.600 inch (0.178 mm by 1.524 cm) spacer.





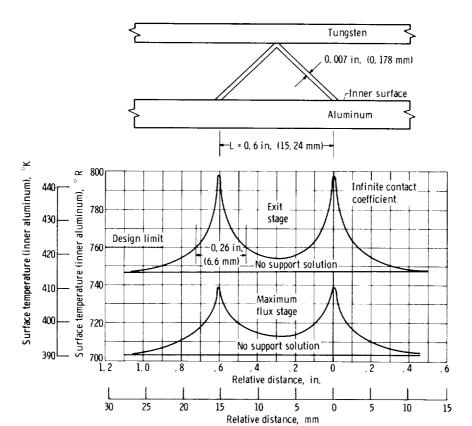
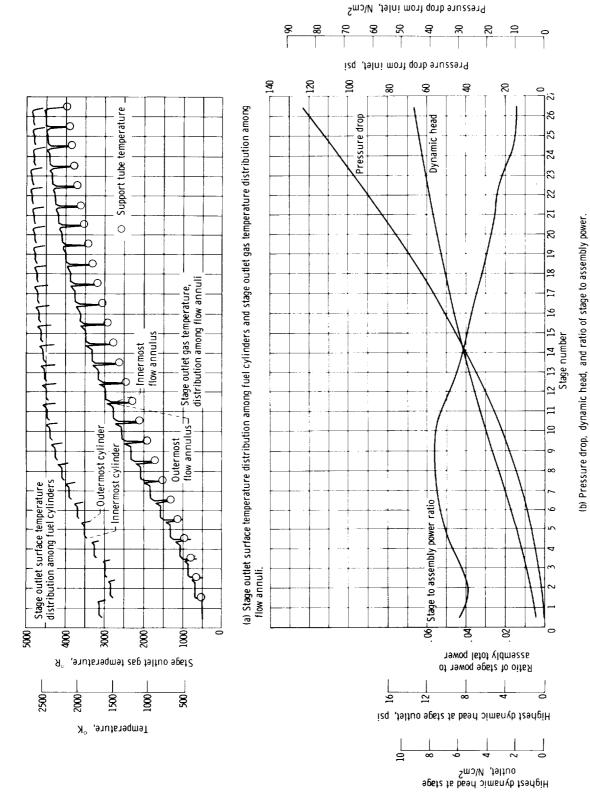


Figure 38. - Effect of inverted V-support on aluminum pressure tube temperature.

PONTEULITIME





SONFTDEN FIAS

Figure 39, - Heat transfer and flow calculation results for concentric-cylinder fuel-element assembly. Assembly power, 15 190 Btu per second (1, 6x10<sup>7</sup> J/sec); assembly inlet gas temperature, 322° R (179° K); assembly outlet gas temperature, 4460° R (2480° K); number of fueled cylinders, 10.

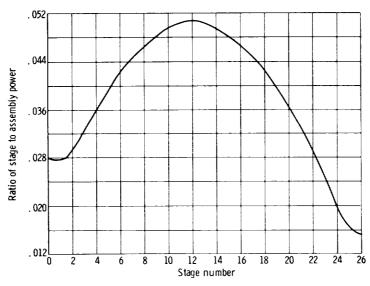


Figure 40. - Unzoned core axial power distribution.



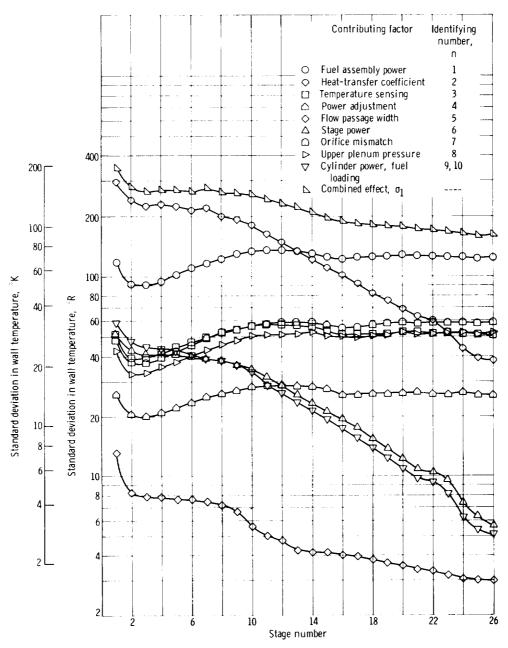
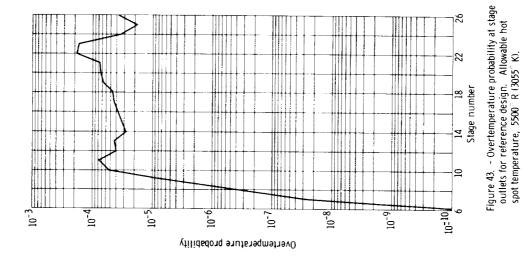
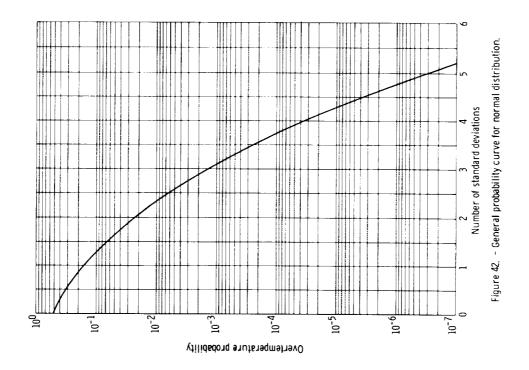
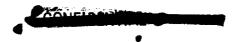


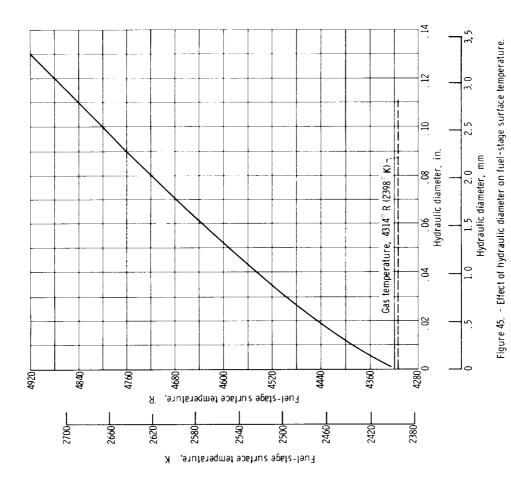
Figure 41. – Stage to stage variation of 1 standard deviation in various uncertainties (see table VIII).



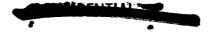








10-5
Overtemperature probability at stage outlets for 29 stages. Allowable hot spot temperatures, 5500° R (3055° K).





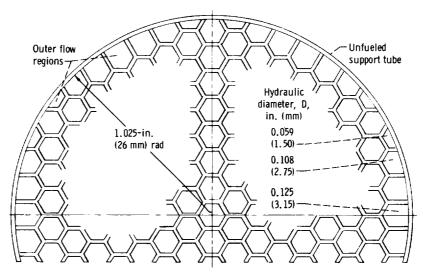
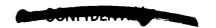


Figure 46. - Honeycomb fuel stage. View in direction of flow. Nominal hydraulic diameter, 0.119 inch (3.02 mm).



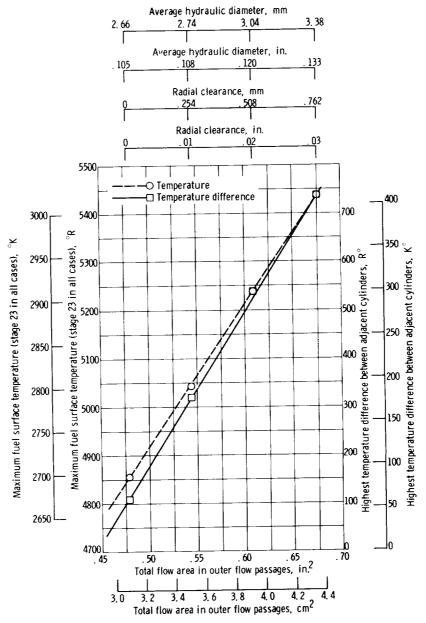
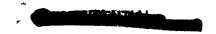
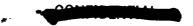


Figure 47. - Effect of total area in outer flow passages of honeycomb stage on maximum surface temperatures and temperature differences. Cylinders used to simulate honeycomb.





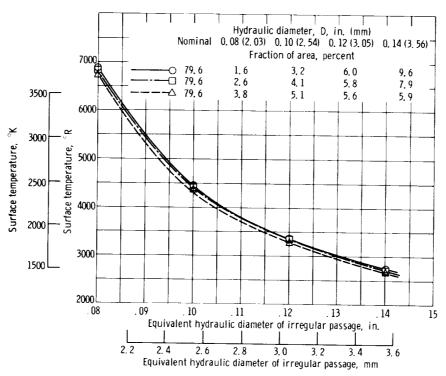


Figure 48. - Effect of irregular flow passages in honeycomb on surface temperature. Ratio of heat transfer surface to total surface in irregular passages, 0, 75; nominal passage equivalent hydraulic diameter, 0, 119 inch (3, 02 mm).

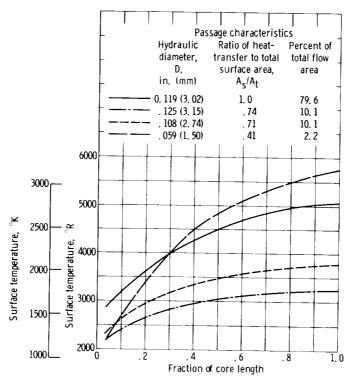


Figure 49. - Surface temperatures of honeycomb fuelelement assembly with irregular passages.

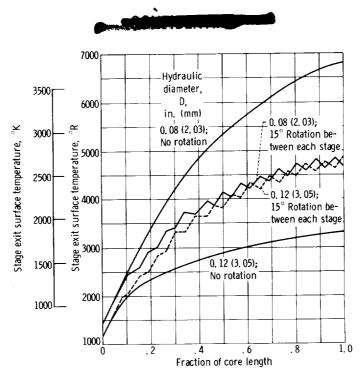


Figure 50. - Effect of rotation of honeycomb stages on temperature differences between irregular passages. Ratio of heat-transfer to total surface area, 0.75. Complete mixing between stages is assumed.

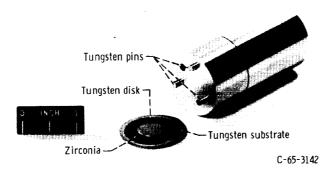


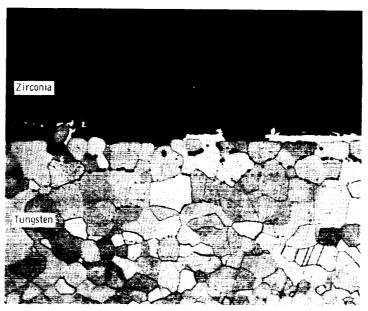
Figure 51. - Tungsten and zirconia compatability test specimens.



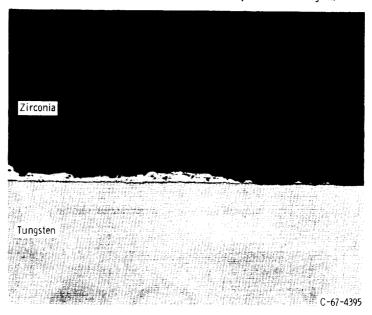
Figure 52. – Zirconia surface before and after compatability test with tungsten.





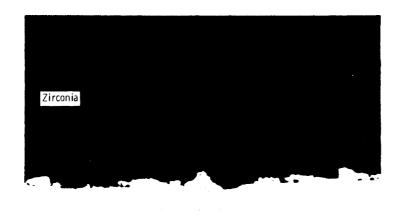


(a) After 2 hours at 3860° R (2145° K). Etchant, Murakami's reagent.



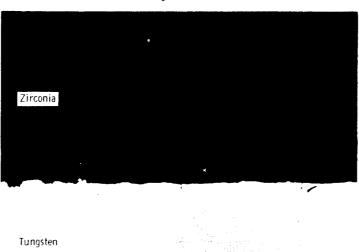
(b) Prior to test.

Figure 53. - Zirconia-coated tungsten test specimen. X100.



Tungsten

(a) Roughened surface.



C-67-4394

(b) Smooth surface,

Figure 54. – Zirconia-coated tungsten test specimen after 2 hours at 3860° R (2145° K). X100.





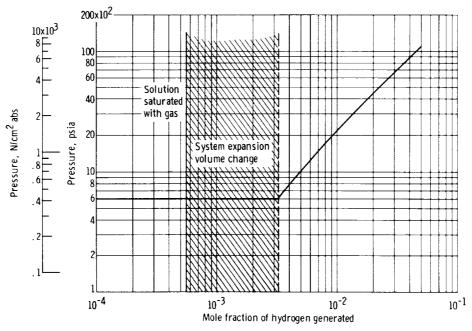


Figure 55. - Calculated control system internal pressure for variations in hydrogen generation,  $% \left( 1\right) =\left( 1\right) \left( 1\right)$ 

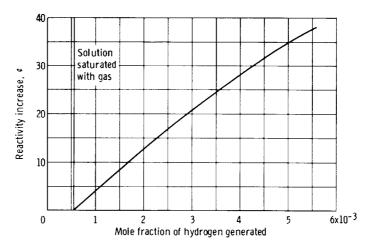


Figure 56. - Reactivity change due to hydrogen gas formation in control system. 1 Cent = 0.0070 percent reactivity.

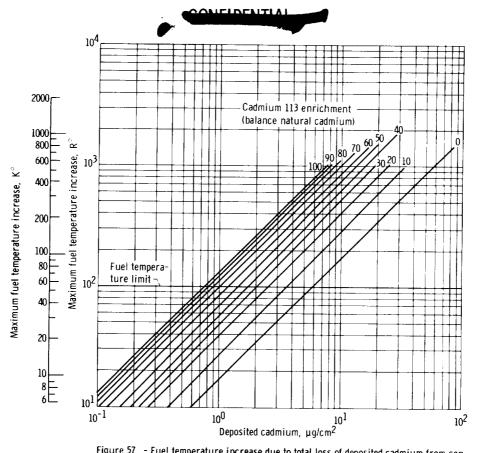


Figure 57. - Fuel temperature increase due to total loss of deposited cadmium from control tubes.

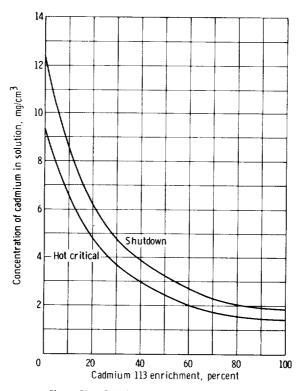
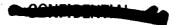


Figure 58. - Cadmium concentration requirements for control of reference design.





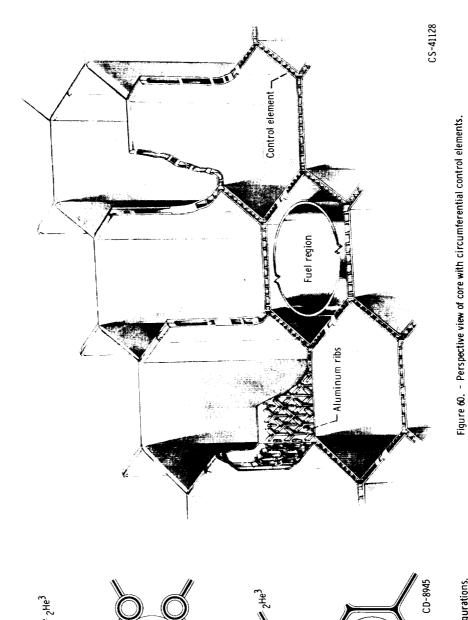
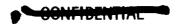


Figure 59. - Gaseous control element configurations.

(b) Circumferential type.



regions (a) Interstitial type.

Control element

Fuel region

Distribution system—

Fuel region



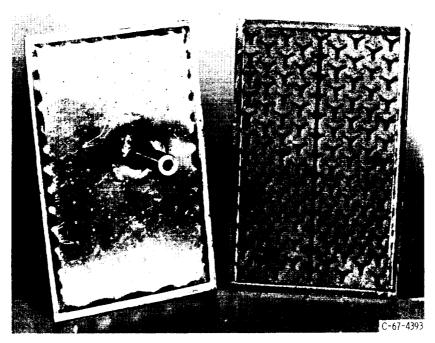


Figure 61. - Specimen of circumferential type control element manufactured by chemical etching. (Photograph courtesy of E. B. Welding Service, Clevite Corp., Aerospace Division.)

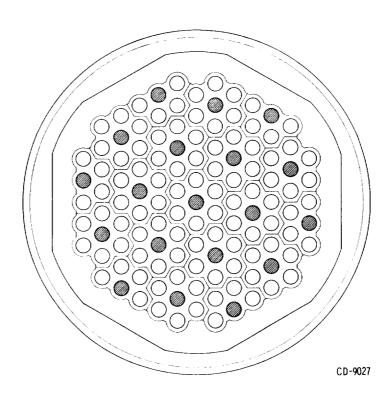
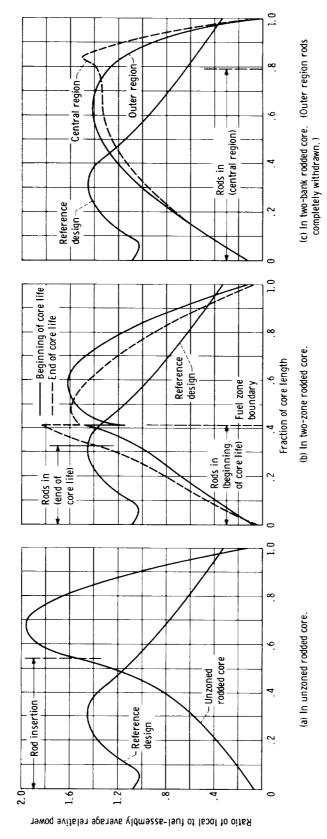


Figure 62. - Core layout with 19 control rods.



CONCIDENTIA

Figure 63. - Axial power distribution.



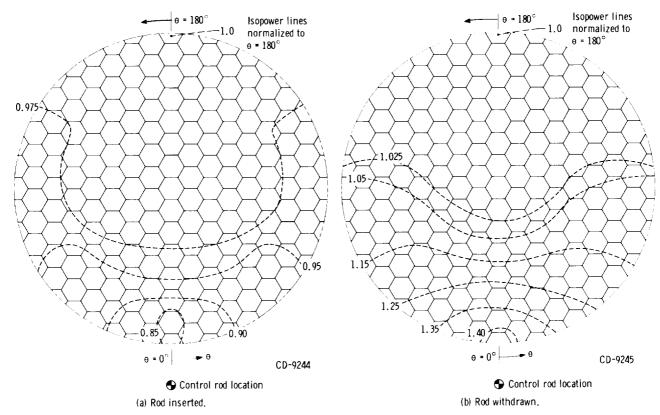


Figure 64. - TWMR rodded reactor relative power across fuel element.

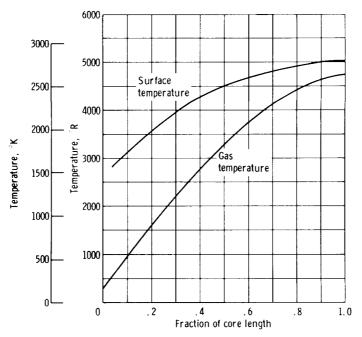


Figure 65. - Thermal performance of reference design reactor with liquid poison control. Length of core (heat-transfer surface), 39 inches (99 cm).



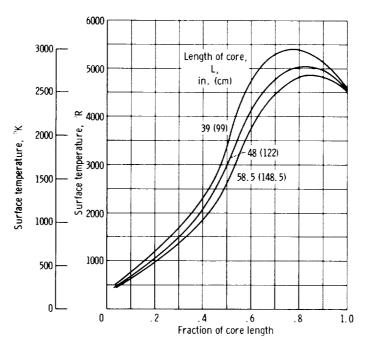


Figure 66. - Effect of length on fuel-element surface temperature of unzoned rodded reactor. Uniform circumferential power distribution in fuel assembly. Exit gas temperature, 4460° R (2475° K).

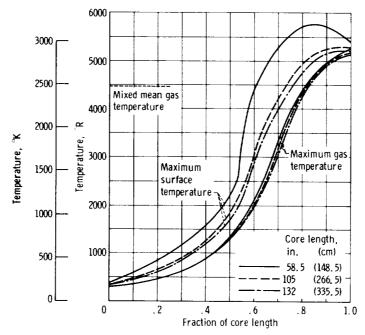


Figure 67. - Thermal performance of unzoned rodded reactor with circumferential power distortion (for passage adjacent to control rod).



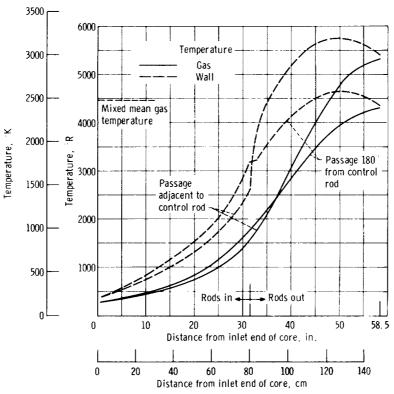
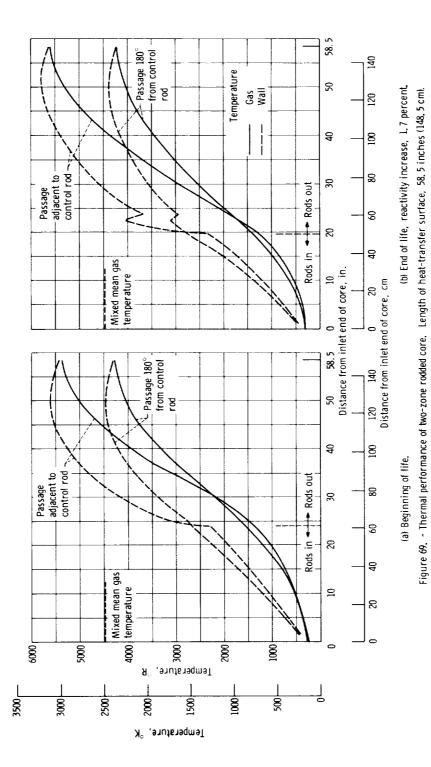
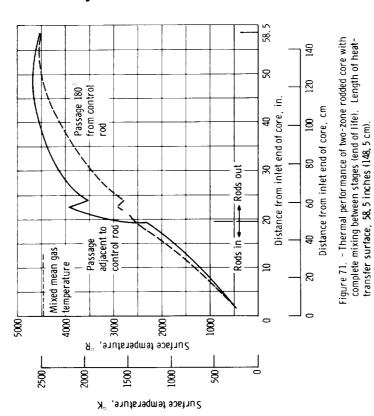
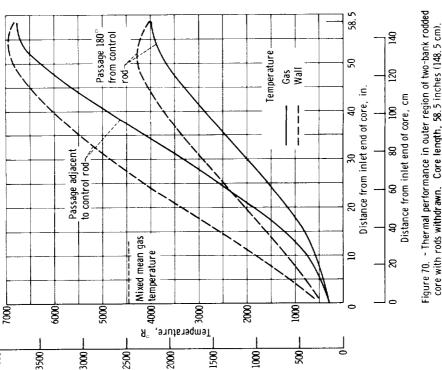


Figure 68. - Thermal performance of unzoned rodded reactor (beginning of life). Core length, 58.5 inches (148.5 cm).







Temperature, "K

4000

Figure 70. - Thermal performance in outer region of two-bank rodded core with rods withdrawn. Core length, 58.5 inches (148.5 cm).

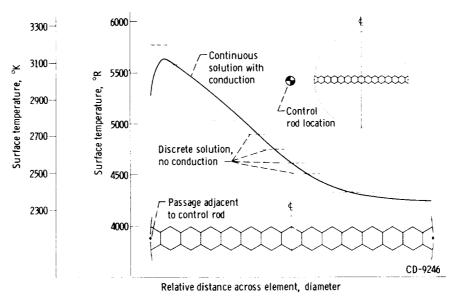


Figure 72. - Effect of interpassage conduction on two fuel zone rodded core (end of life) surface temperature.

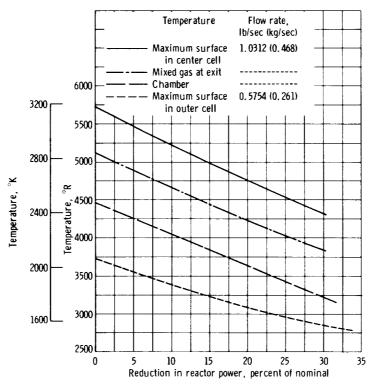


Figure 73. - Reduction in power required to compensate for drum rotation in combination drum and rod control core. Drums in: initial flow distribution based on drums-out condition.





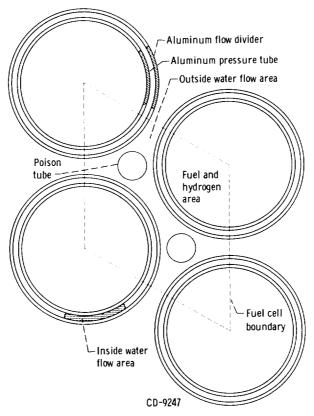


Figure 74. - Typical reference-design fuel cell.

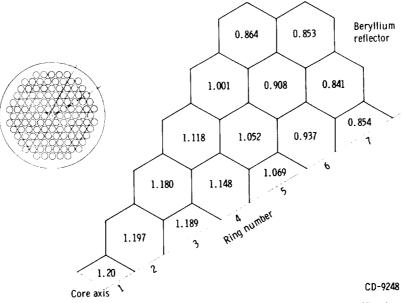


Figure 75. - Relative cell fission power distribution (local to average) for one-twelfth of symmetrical core. (See fig. 2 for designation of ring numbers.)

## CONFIDENTIAL

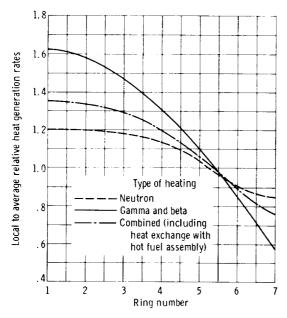


Figure 76. - Radial distribution of volumetric heating rates in water. (See fig. 2 for explanation of ring numbers.)

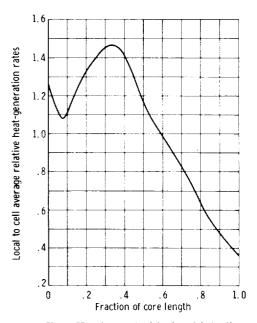


Figure 77. - Assumed axial volumetric heating rate distribution.

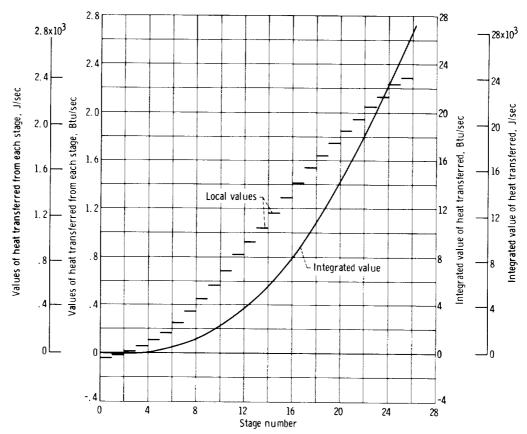
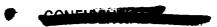


Figure 78. - Axial variation of heat transferred to water from hot fuel assembly.





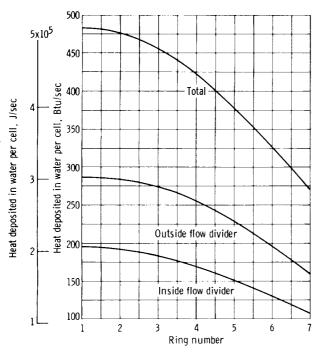


Figure 79. - Radial distribution of heat transferred to and generated in water. (See fig. 2 for explanation of ring numbers.)

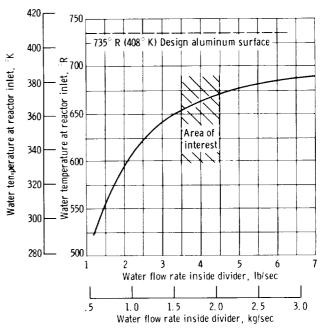


Figure 80. - Water inlet temperature required to cool pressure tube of center fuel assembly at various flow rates.

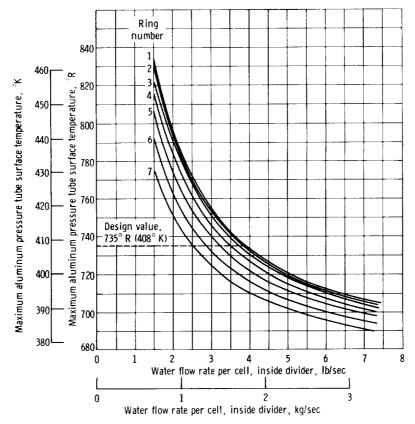


Figure 81. - Effect of flow rate on maximum aluminum pressure tube temperature. Water temperature at reactor inlet,  $660^\circ$  R ( $367^\circ$  K).





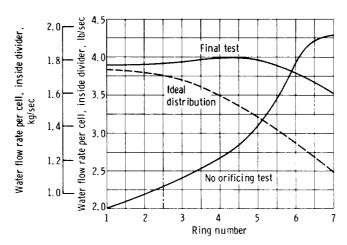


Figure 82. - Water flow distribution test results.

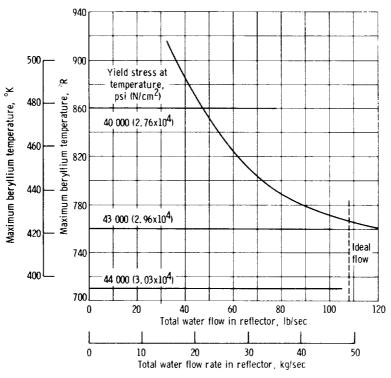
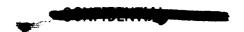


Figure 83. - Effect of water flow rate in reflector on maximum beryllium temperature. Water temperature at reactor inlet  $660^\circ$  R,  $(367^\circ$  K).



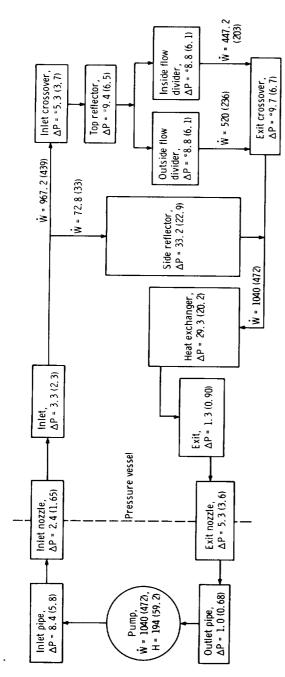


Figure 84. - Predicted pressure drops and prescribed flow distribution in test facility. Pump head, H, ft (m); flow rate, W, 1b/sec (kg/sec); pressure loss, ΔP, psi (N/cm²). (Starred values are for center fuel assembly.)

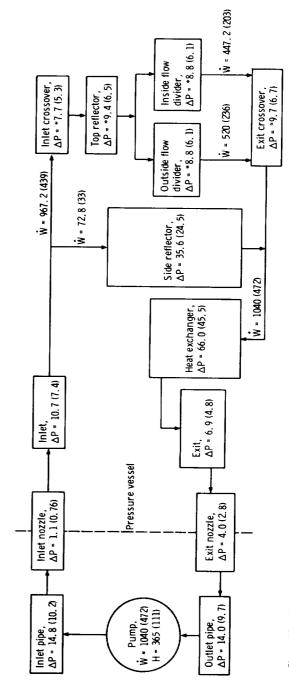
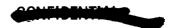


Figure 85. - Predicted pressure drops and prescribed flow distribution for reference design. Pump head, H, fl of water (m of water); flow rate, Ψ, lb/sec (kg/sec); pressure loss, ΔP, psi (N/cm²). (Starred values are for center fuel assembly.)



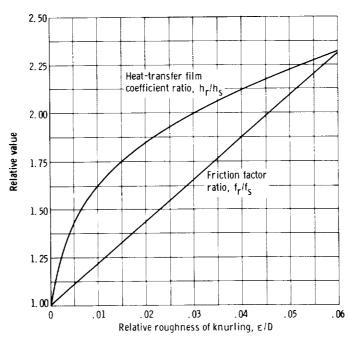


Figure 86. - Effect of knurling on heat transfer and fluid flow in an annular passage (see ref. 34). Only heat-transfer surface knurled.

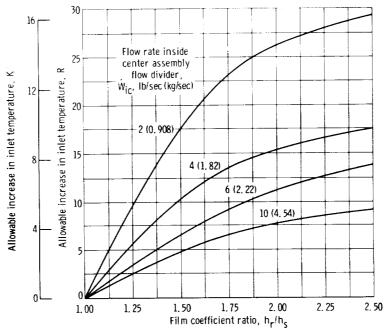
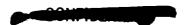


Figure 87. - Effect of film coefficient on allowable water inlet temperature.



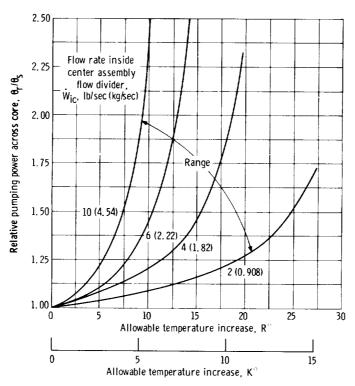


Figure 88. - Effect of knurling on pumping power at constant flow.

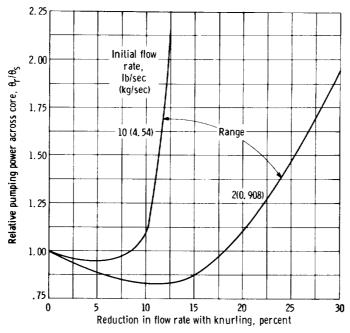
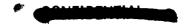
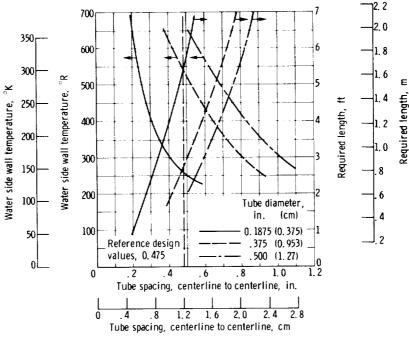


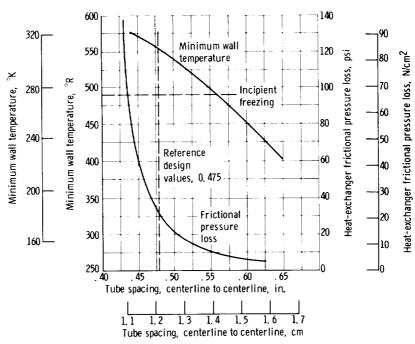
Figure 89. - Effect of knurling on pumping power at constant inlet temperature.







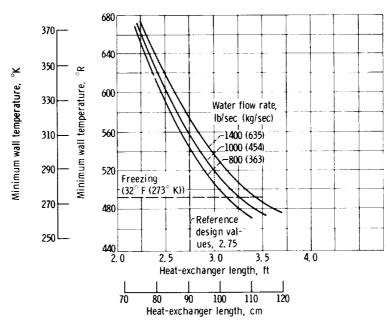
(a) Tube diameter and spacing. (See table 16 for referencedesign conditions for heat-transfer rate, fluid flow rates, and inlet fluid temperatures.)



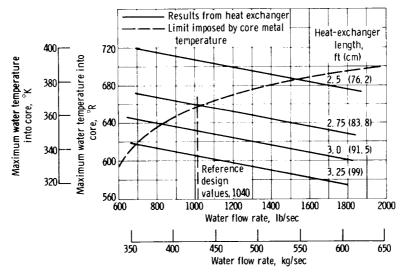
(b) Tube spacing. Tube diameter, 0. 375 inch (0. 953 cm). (See table 16 for reference-design conditions for heat-transfer rate, fluid flow rates, and inlet fluid temperatures.)

Figure 90. - Effects of geometry and flow parameters on heatexchanger performance.



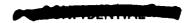


(c) Length. (See table 16 for reference-design conditions for heat-transfer rate, hydrogen flow rate and inlet temperature, and tube diameter and spacing.)



(d) Heat-exchanger length on required water flow rate. (See table 16 for reference-design conditions for heat-transfer rate, hydrogen flow rate and inlet temperature, and tube size and tube spacing.)

Figure 90. - Concluded.





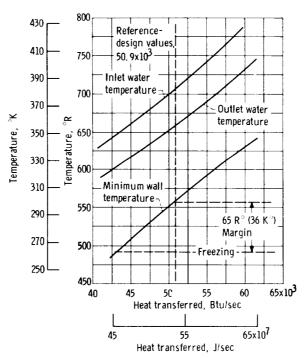
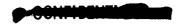


Figure 91. - Effect of heat-transfer rate on heat-exchanger performance. (See table 16 for reference-design conditions for fluid flow rates, inlet hydrogen temperature, and tube size and spacing.)



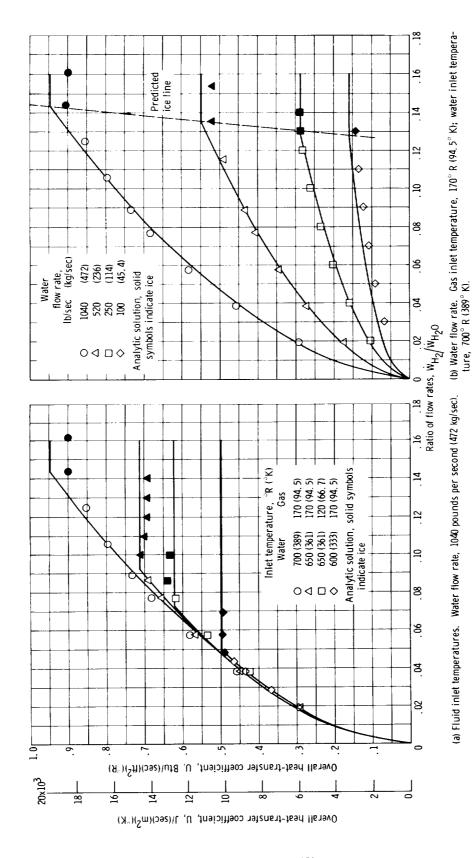
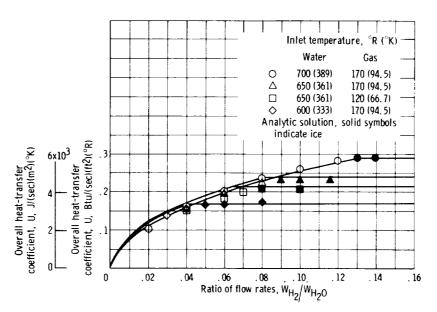


Figure 92. - Effects of temperature and flow rate on performance of reference-design heat exchanger.





(c) Fluid inlet temperatures. Reduced water flow rate of 250 pounds per second (114 kg/sec).

Figure 92. - Concluded.

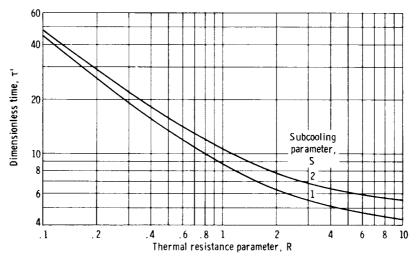
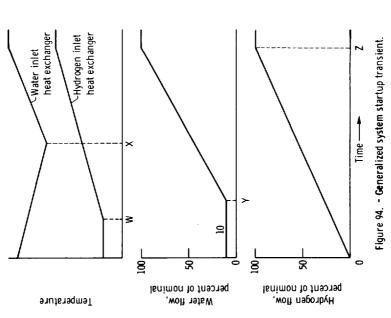
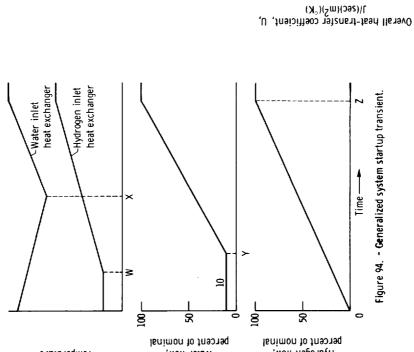
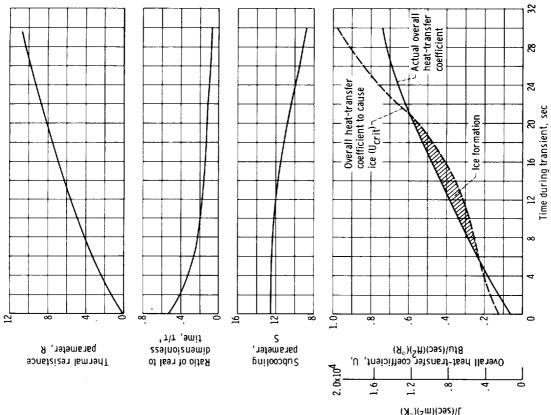


Figure 93. – Time to reach 98 percent of steady-state ice thickness during transient (ref. 32).

Figure 95. - Variation in ice formation parameters during typical startup (case 1, table 17).









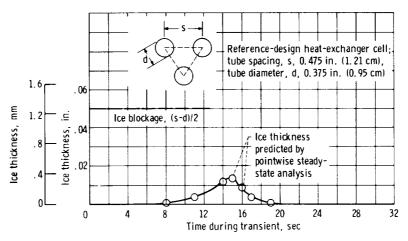


Figure 96. - Variation of ice thickness on heat-exchanger tubes during typical startup (case 1, table 17).

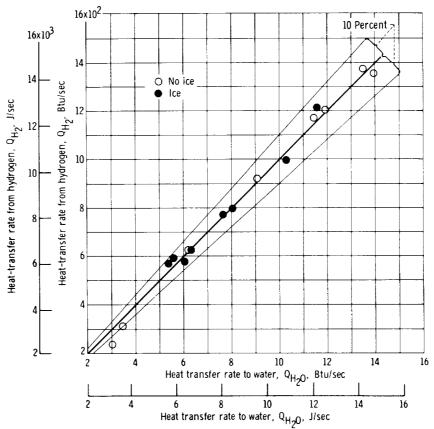


Figure 97. - Heat balance for heat-exchanger tests. Normal hydrogen gas; para-hydrogen liquid.



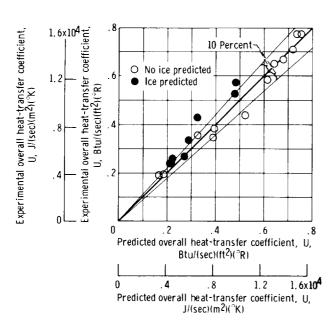


Figure 98. - Comparison of experimental and predicted overall heat-transfer coefficients for heat-exchanger tests.

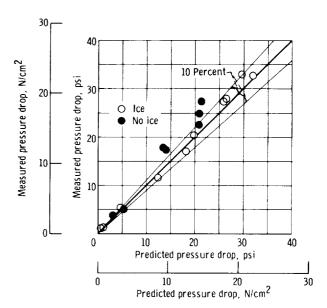


Figure 99. - Comparison of measured and predicted hydrogen pressure drop for heat-exchanger tests.

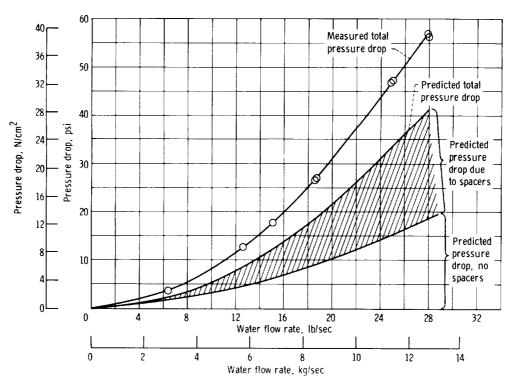


Figure 100. – Predicted and measured isothermal water pressure drops in test heat exchanger. Isothermal test water temperature,  $534^{\circ}$  R (297 K).



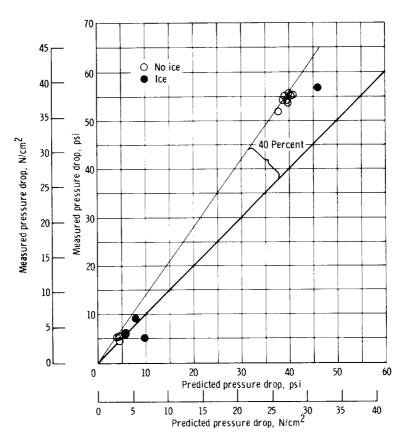
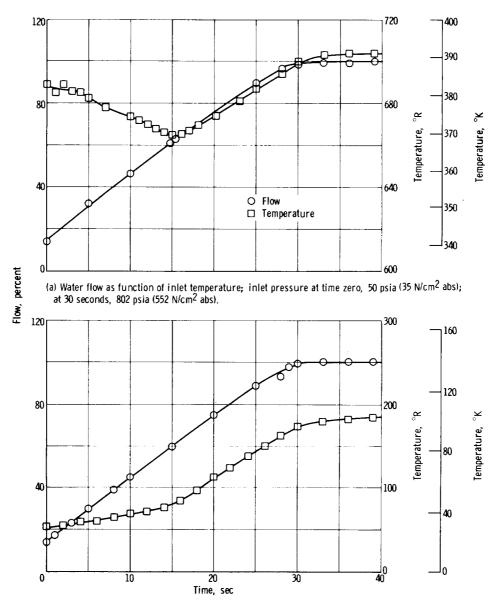


Figure 101. - Comparison of measured and predicted water pressure drops for heat-exchanger tests.



(b) Hydrogen flow as function of inlet temperature; inlet pressure at time zero,  $87 \text{ psia } (59.9 \text{ N/cm}^2 \text{ abs})$ ; at 30 seconds,  $733 \text{ psia } (504 \text{ N/cm}^2 \text{ abs})$ .

Figure 102. - Measured fluid flow rates and inlet temperature during transient heat-exchanger test.

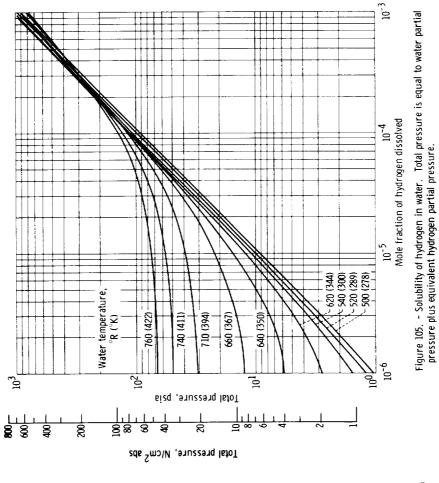


Figure 103. - Overall heat-transfer coefficient during transient heat-exchanger tests (see fig. 101 for fluid flow rates, temperatures, and pressures).

Percent of total ramp time

8

**E** 

Ramp time,

0

**D** 

Overall heat-transfer coefficient, U, Btu/(sec)(ft $^2$ )(°R)

Overall heat-transfer coefficient,  $U_{\rm r} / (sec) (m^2)(^2K)$ 

Overall heat-transfer coefficient at τ = ∞ --

28 8 32

0 4 0-

囡

8 0 0 þ Percent of total ramp time 0 Transient Steady state 0 🏻 20 Overall heat-transfer coefficient, U, Btu/(sec)(ft<sup>2</sup>)(<sup>2</sup>R) 1.6x1n<sup>4</sup>

 $\chi(sec)(m^2)/\chi$ Overall heat-transfer coefficient, U,

Figure 104. - Overall heat-transfer coefficient during transient heat-exchanger tests with reduced water inlet temperatures. Ramp time, 30 seconds: inlet water temperatures 40 R $^\circ$  (22, 2 K $^\circ$ ) below those in figure 103.

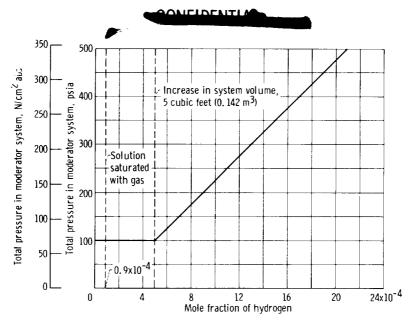


Figure 106. - Internal pressure in moderator system with hydrogen generation. Water temperature,  $660^{\circ}$  R (367 K).

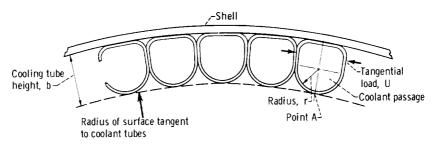


Figure 107. - Cross section of formed tube configuration for nozzle cooling.

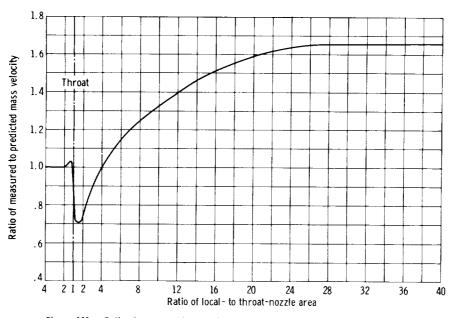


Figure 108. - Ratio of measured to one-dimensional predicted mass velocity in bell-shaped exit cone.



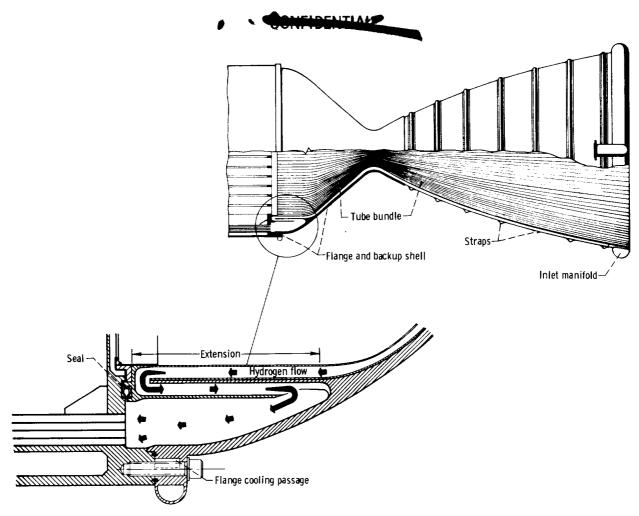


Figure 109. - Reference - design thrust nozzle.

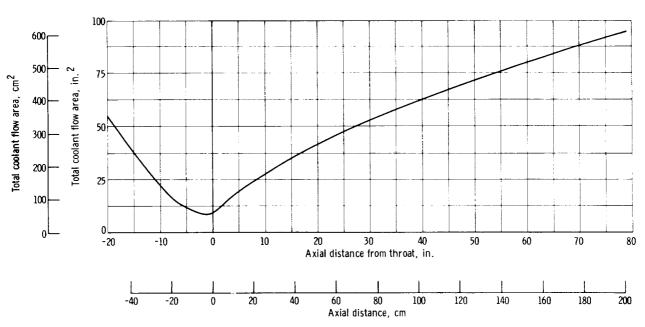
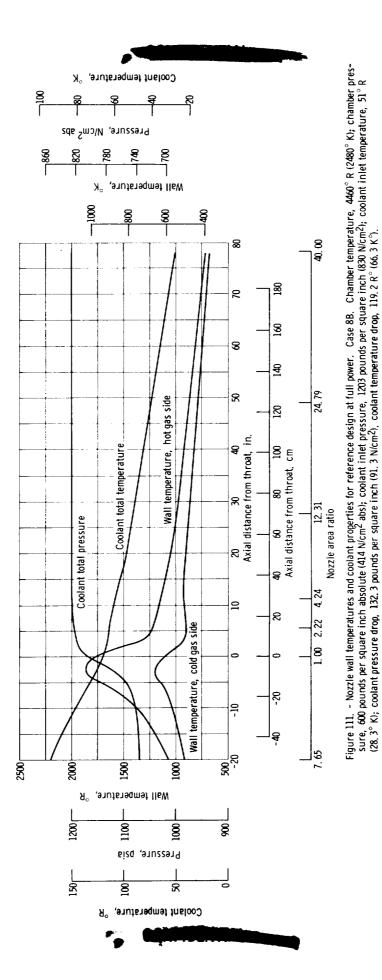
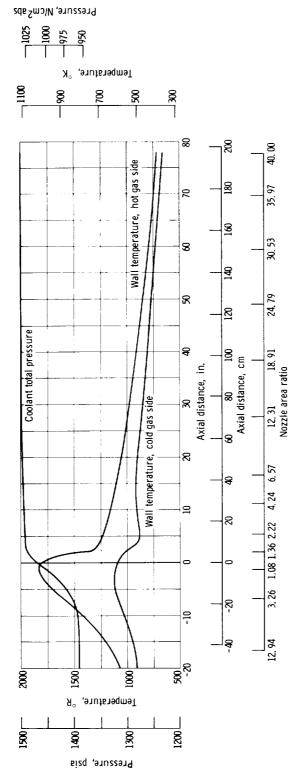


Figure 110. - Variation of flow area in nozzle cooling passages for case 88. Direction of hot gas flow is from left to right.

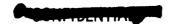


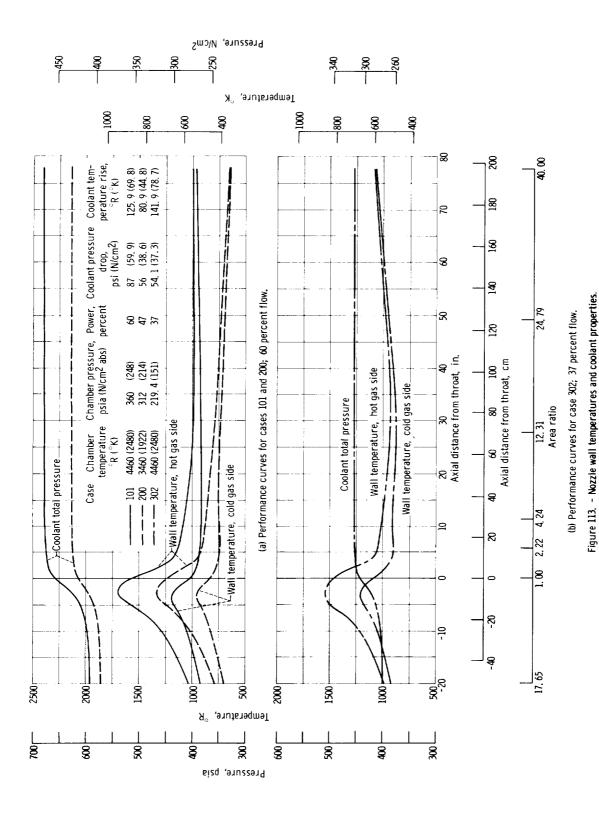
## P GONFIDENTIAL



---

Figure 112. - Nozzle wall temperatures and coolant properties for increased coolant inlet pressure and full power. Case 19. Chamber temperature, 4460° R (2480° K); chamber pressure, 600 pounds per square inch absolute (414 N/cm² abs); coolant inlet temperature, 51° R (28.3° K); coolant inlet pressure, 1500 pounds per square inch absolute (1033 N/cm² abs); coolant pressure drop, 110 pounds per square inch absolute (75.8 N/cm² abs); coolant temperature drop, 128 R° (71.2 K°).





O COMPANY OF THE PARK OF THE P

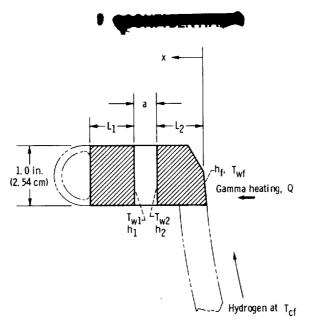


Figure 114. - Nozzle flange heat-transfer model. Slot width, a; outer and inner side flange slot heat-transfer coefficients,  $\mathbf{h}_1$  and  $\mathbf{h}_2$ , respectively; flange inner surface heat-transfer coefficient,  $\mathbf{h}_f$ ; distance from outer and inner flange surface to slot surface,  $\mathbf{L}_1$  and  $\mathbf{L}_2$ , respectively; outer and inner wall temperatures of flange slot,  $\mathbf{T}_{\mathbf{W}1}$  and  $\mathbf{T}_{\mathbf{W}2}$ , respectively; inner flange surface temperature  $\mathbf{T}_{\mathbf{W}f}$ ; radial distance from inner flange surface,  $\mathbf{x}_i$ ; temperature of hydrogen coolant on inner flange,  $\mathbf{T}_{\mathbf{C}f}$ .

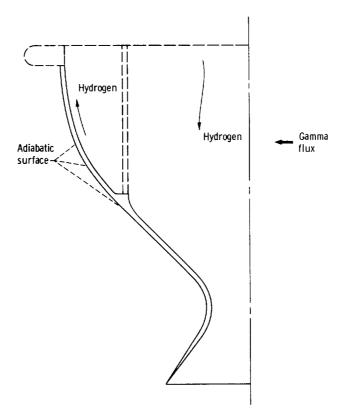


Figure 115. - Backup shell heat-transfer model.



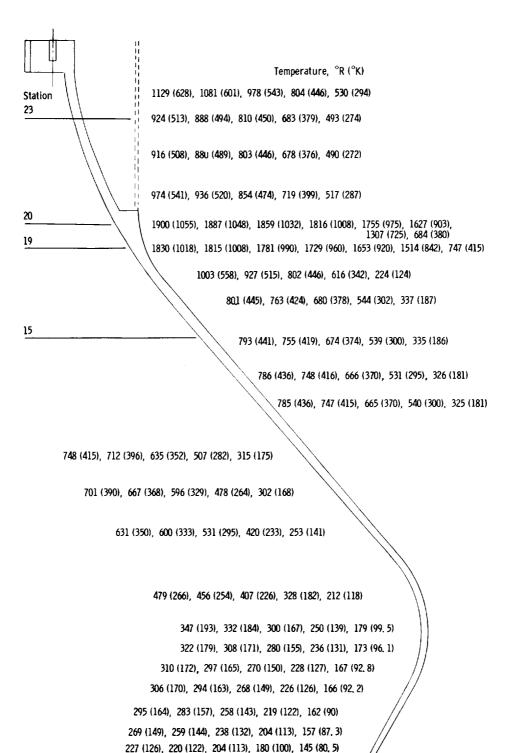


Figure 116. - Nozzle backup shell temperature distributions. Values shown are for temperatures at equidistant points across wall thickness.

196 (109), 191 (106), 180 (100), 162 (90), 137 (76)





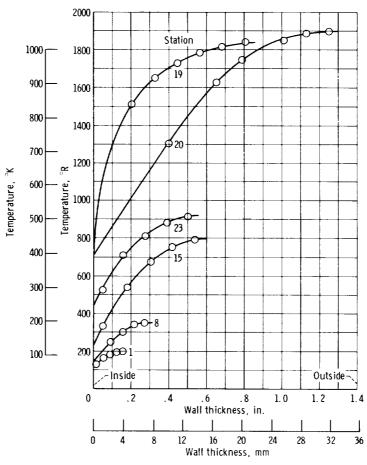


Figure 117. - Temperature profile in wall of nozzle backup shell (see fig. 115 for station locations).

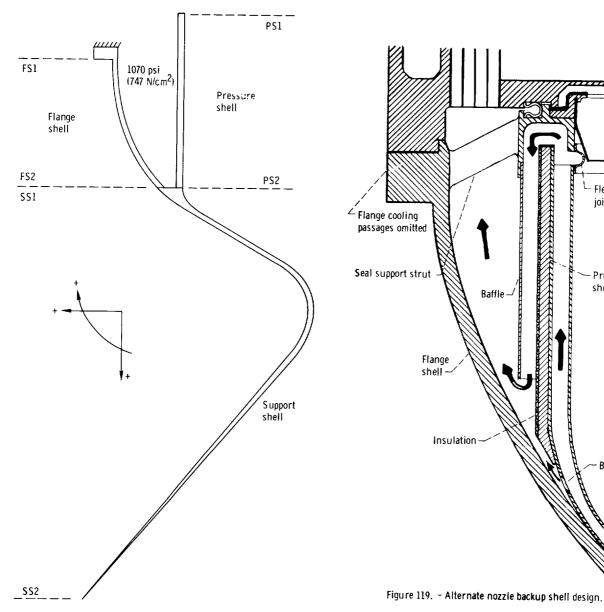


Figure 118. - Model of nozzle backup-shell stress. Chamber  $\mu$  essure, 600 pounds per square inch (414 N/cm²). (See table 22 for ca. es run.)

Flexible

Pressure shell

Bleed holes

joint



CONFIDENTIAL